Development Of A Novel Metal-Binding Lipid As A New Building Block For Artificial Cells

Gabriela Sachet Fernández

Department of Chemistry

Imperial College London

Thesis submitted for a degree of Doctor of Philosophy

May 2024

Originality and Copyright declaration

I, Gabriela Sachet Fernández declare that all the material presented in this thesis is my own work except where referenced.

The copyright of this thesis rests with the author. Unless otherwise indicated, its contents are licensed under a Creative Commons Attribution-Non Commercial 4.0 International Licence (CC BY-NC).

Under this licence, you may copy and redistribute the material in any medium or format. You may also create and distribute modified versions of the work. This is on the condition that: you credit the author and do not use it, or any derivative works, for a commercial purpose. When reusing or sharing this work, ensure you make the licence terms clear to others by naming the licence and linking to the licence text. Where a work has been adapted, you should indicate that the work has been changed and describe those changes.

Please seek permission from the copyright holder for uses of this work that are not included in this licence or permitted under UK Copyright Law.

Acknowledgments

I am highly grateful to my main supervisor, Rudiger Woscholski, for his unwavering support and guidance throughout my three years as a PhD student in his research group. His dedication and availability have been instrumental in my academic journey. I would like to extend my gratitude to Oscar Ces for his continuous support and encouragement throughout the thesis process. I consider myself incredibly fortunate to have had supervisors who not only excel in their academic positions but also demonstrate exceptional humanity skills and inspiration for students like me.

Additionally, I would like to share a special appreciation to James Hindley for his invaluable training during challenging times, particularly amidst the COVID-19 pandemic, and for his consistent project oversight and advice. My gratitude also extends to Kevin, whose mentorship and practical insights greatly enriched my learning experience. I am equally indebted to Nacho for his unfailing availability to address my queries and for generously sharing his experience. Our scholar relationship has developed into a long-life friendship, alongside Juan and Giulia, with whom I've shared countless laughter-filled lunch breaks, enriching this journey with unforgettable memories in London. I am also thankful for the valuable support by my close friends Anna and Lis, who have understood the process I have been through and that we have pushed each other in the best way possible.

Lastly, I wish to express my deepest appreciation to my family and friends for their unwavering emotional support. To my parents, sister, and brother, and to my husband Felix, who has been a constant source of encouragement through the ups and downs of this journey.

Abstract

Bottom-up synthetic biology aims at building structures and functions of living cells from non-living building blocks by leveraging tools from biology, chemistry, and materials science. The field has progressed from recreating simple biological functions to integrating complex systems that combine both biological and synthetic functions. For this reason, there is a pressing need to develop new tools to functionalise artificial cells to achieve higher levels of complexity. One approach to functionalise artificial cells is through their membranes, particularly through the incorporation of functional phospholipids in the membrane. Thus, there is a need to synthesise artificial lipids with functional headgroups to enable their incorporation into the membrane of vesicles.

In this research, a phosphatidyl-histidinol lipid carrying an imidazole moiety was synthesised as a tool for reversibly binding his-tagged compounds to the membrane of vesicles and facilitating vesicle-vesicle interactions.
The lipid was synthesised by enzyme-assisted synthesis using phospholipase D, wherein the headgroup of a phospholipid was transphosphatidylated with L-histidinol. We validated the lipid-binding functionality with metal ions, both in a coated system and in a vesicular system. For proof of concept, his-mEGFP was utilized. Additionally, the lipid exhibited catalytic properties attributed to its imidazole moiety, with a metal dependency as well as a lipid presentation dependency. Unexpectedly, the incorporation of PtdHisOH into a vesicular system promoted membrane asymmetry with the synthetic lipid being predominantly located in the outer leaflet of the bilayer. Finally, we demonstrated lipid-lipid interactions mediated by zinc ions, resulting in hemi-fusion of vesicles lipid membrane mixing.

The PtdHisOH lipid offers a new tool for facilitating vesicle aggregation and promoting cell-cell interaction, thereby enabling the formation of tissue-like structures. Its potential applications extend to biomedical fields, including targeted nanodelivery, leveraging the lipid's metal selectivity. Moreover, the lipid holds promise in the development of micromachines, facilitating in situ specific reactions.

Publications

The work presented in this thesis will be partially published. The manuscript is under correction.

Authors: *Sachet-Fernandez, G., Hindley, J. W., Ces, O., Woscholski, R.*

Proposed title: *Novel imidazole headgroup phospholipid shows a symmetric distribution in bilayer and zinc dependent esterase activity in vesicles.*

Abbreviations

a.u.	Arbitrary unit
BNPP	Bis(4-nitrophenyl) phosphate
BSA	Bovine serum albumin
Ca^{2+}	Calcium ion
Co^{2+}	Cobalt (II) ion
Cu^{2+}	Copper (II) ion
DLS	Dynamic light scattering
DOPA	1,2-dioleoyl-sn-glycero-3-phosphate (sodium salt)
DOPC	1,2-dioleoyl-sn-glycero-3-phosphocholine
DOPE	1,2-dioleoyl-sn-glycero-3-phosphoethanolamine
E. coli	*Escherichia coli*
FDA	Fluorescein Diacetate
Fe^{2+}	Iron (II) ion
GUV	Giant unilamellar vesicle
HEPES	4-(2-hydroxyethyl)-1-piperazineethanesulfonic acid
LUV	Large unilamellar vesicle
mEGFP	Monomeric enhanced green fluorescent protein
NBD	Nitrobenzoxadiazole
PDE	Phosphodieterase activity
PLD	Phospholipase D
pNPP	p-Nitrophenyl Phosphate
PtdHisOH	Phosphatidyl histidinol
Rhd B	Rhodamine B
TLC	Thin Layer Chromatography
Zn^{2+}	Zinc (II) ion

Table of contents

Originality and Copyright declaration 2

Acknowledgments 3

Abstract 4

Publications 5

Abbreviations 6

1. Chapter 1: Introduction 12

1.1. Chapter outline 12

1.2. Synthetic biology 12

1.2.1. Top-down vs bottom-up approach 13

1.3. Biological and artificial membranes 16

1.3.1. Biological membrane structure 16

1.3.2. Types of lipids 18

1.3.3. Lipid functions 19

1.3.4. Membrane asymmetry 20

1.3.5. Membrane phases and curvatures 20

1.4. Model membranes: vesicular systems 23

1.4.1. Artificial cells chassis 24

1.4.2. Membrane functionalisation 25

1.4.3. Membrane fusion 26

1.5. Lipid synthesis 27

1.5.1. Organic and biochemical synthesis 27

1.5.2. Phospholipase enzymes 28

1.5.3. Phospholipase D and transphosphatidylation 29

1.6. Imidazole catalysis 31

1.7. Aim & objectives 32

2. Chapter 2: General Materials and methods 34
2.1. PtdHisOH lipid synthesis 34
2.1.1. Lipids 34
2.1.2. Lipid coating 35
2.1.3. Synthesis in the coating system 35
2.1.4. Detection of the product 36
2.1.5. Scaling-up the reaction 37
2.2. Chemical characterisation of the synthesized lipids 38
2.2.1. TLC analysis & stains 38
2.2.2. Mini column chromatography 39
2.2.3. Mass spectrometry 40
2.3. Catalysis 40
2.3.1. BNPP assay 40
2.3.2. pNPP assay 41
2.3.3. FDA 42
2.4. Vesicles and micelles 43
2.4.1. Lipid films 43
2.4.2. Preparation of LUVs by extrusion (large unilamellar vesicles) 43
2.4.3. Preparation of GUVs by emulsion phase transfer 43
2.4.4. Preparation of detergent mixed micelles 45
2.5. Particle sizer 45
2.6. Fluorescence wide-field microscopy and confocal microscopy 45
2.7. His-mEGFP 46
2.7.1. Protein expression and purification 46
2.7.2. SDS-page protein gel 50
2.7.3. Quantification 52

2.8. Flow cytometry for fusion assays 52
2.9. Software for figures 52
3. Chapter 3: PtdHisOH synthesis & chemical characterization 53
3.1. Optimisation of the transphosphatidylation reaction in the coated system 54
3.1.1. Introduction of the coated system 54
3.1.2. Optimal reaction time 54
3.1.3. Reducing unspecific interactions of PLD enzyme 55
3.1.4. Optimal substrate concentration: L-histidinol gradient (Km/Vmax) 56
3.1.5. Optimal PLD units for the reaction 58
3.1.6. Temperature 59
3.2. Optimisation of the reaction is the 2-phase system 60
3.2.1. Optimal reaction time 60
3.2.2. Optimal substrate concentration 62
3.2.3. PLD units 62
3.2.4. Temperature 63
3.2.5. Evaporation of chloroform/leaking chloroform 65
3.3. Scaled-up reaction in a glass vial 66
3.4. Yields 68
3.5. Chemical characterisation on TLC 68
3.6. Purification and chemical characterisation through mass spectrometry 72
3.7. Conclusions 73
4. Chapter 4: Characterization of PtdHisOH metal-binding properties 75
4.1. Lipid functionality – metal binding assay development 75
4.1.1. Zincon: a chelating chromophore 76
4.1.2. Quenching of calcein 81
4.2. Functionality through protein binding in the coating 86

4.2.1. His-mEGFP - PtdHisOH binding through Cu^{2+} 87
4.2.2. Testing other metals 89
4.3. Conclusions & future work 91
5. Chapter 5: Catalytic properties of PtdHisOH 92
5.1. Catalytic abilities: esterase, phosphodiesterase, phosphatase activity 93
5.1.1. Phosphodiaestarase activity 93
5.1.2. Phosphatase activity 99
5.1.3. Esterase activity 101
5.2. Esterase activity 103
5.2.1. Lipid presentation 103
5.2.2. Variation of PtdHisOH amounts 105
5.2.3. Effect of Zn^{2+} on PtdHisOH LUVs 107
5.2.4. Zn^{2+} dependency of the esterase activity 109
5.3. Conclusions & future work 112
6. Chapter 6: Application of PtdHisOH to the Artificial Cell technology 114
6.1. Incorporation of the PtdHisOH lipid into the membrane of artificial cells 114
6.1.1. Characterisation and stability of LUVs with PtdHisOH 114
6.1.2. Lipid distribution in PtdHisOH LUVs 116
6.2. Applying the lipid-metal affinity to attract vesicles together 118
6.2.1. Size distribution of PtdHisOH LUVs in the presence of metal ions 119
6.2.2. Investigating the increase in size of LUVs 121
6.3. Making GUVs with PtdHisOH 127
6.4. Lipid-protein interaction in GUVs 128
6.4.1. Lipid-protein binding in PtdHisOH GUVs 128
6.5. Lipid-lipid interaction in GUVs 133
6.6. Catalysis – Fura-2AM 135

6.7. Conclusions & future work 140

7. Conclusions & future work 141

7.1. Summary of findings 141

7.2. Future work 142

7.2.1. Sythesis of functional phospholipids 142

8. Appendix 145

9. References 148

1. Chapter 1: Introduction

1.1. Chapter outline

The aim of this research project is to develop new tools to broaden the applications of artificial cell by enhancing their functionalisation. By synthesizing novel phospholipids to be incorporated into the artificial cell membrane, new functions can be achieved, such as reversible protein binding and cell-cell interaction.

This introduction provides context and background information for this research but does not intend to be an extensive review of the discussed topics. The first part of the introduction will give a brief overview of synthetic biology and the two main approaches that are being used, the bottom-up and the top down approach [1]. Secondly, biological and artificial membrane properties will be introduced, with a focus on their compositions, their importance and roles played within the cell. Thirdly, model membranes will be discussed, and more particularly liposomes which are used as the chassis for building artificial cells. Artificial phospholipid generation will then be introduced, and more particularly enzyme assisted synthesis. A brief overview of catalysis in biological systems will follow. The aims and objectives of the project are presented at the end of the introduction chapter.

1.2. Synthetic biology

Modern synthetic biology emerged in the early 21st century as a multidisciplinary field that combined insights from biology, engineering, and computer science. It marked a departure from traditional biological research by seeking to actively engineer and manipulate biological systems to achieve specific goals [2]. This shift in perspective led to the development of new methodologies and approaches that allowed researchers to redesign living organisms at the genetic level.

Early developments in synthetic biology focused on creating modular genetic components and standardizing biological parts [3]. These efforts aimed to simplify the process of genetic engineering by providing researchers with standardized building blocks that could be easily combined and repurposed for various applications. Advances in DNA sequencing technologies during this period also played a crucial role, enabling

scientists to rapidly decipher the genetic code of organisms and manipulate DNA with unprecedented precision.

The applications of synthetic biology are diverse and far-reaching. In medicine, it holds the promise of personalized therapies and treatments tailored to individual genetic profiles [4]. In agriculture, synthetic biology can lead to the development of crops that are more resilient to environmental stressors and produce higher yields, addressing food security challenges. Furthermore, synthetic biology has implications for energy production, with the potential to create biofuels and renewable energy sources that are more efficient and sustainable [5].
Looking to the future, synthetic biology is poised to play an even greater role in addressing global challenges and driving innovation. Emerging technologies, such as CRISPR-Cas (Clustered Regularly Interspaced Short Palindromic Repeats) gene editing, offer new avenues for manipulating biological systems with unprecedented precision and efficiency [6]. These advancements hold the potential to unlock novel solutions to pressing issues such as disease, environmental degradation, and resource scarcity [7].

Overall, synthetic biology represents a paradigm shift in our approach to understanding and harnessing the power of living organisms. By integrating principles from diverse disciplines and leveraging cutting-edge technologies, synthetic biology opens new possibilities for solving some of the most pressing challenges facing humanity as those described above. Two main approaches exist for synthetic biology: the top-down approach, which has been the more extensively studied one, and the bottom-up approach, which represents a newer frontier within the field (Figure 1.1) [1].

1.2.1. Top-down vs bottom-up approach

The top-down approach is the modification of existing biological systems (cells, microorganisms, organisms), to achieve desired functionalities. The first genetic modification of *Escherichia coli* (*E. coli*) in 1973, which involved the incorporation of an antibiotic resistance gene, stands as a starting point achievement in the field of genetic engineering [8]. Since then, the discipline has undergone remarkable evolution. Today,

the manipulation of DNA extends across various microorganisms, including bacteria and yeast, as well as mammalian cells and plants. Genetic material can be added (knock-in), removed (knocked-out) or replaced, facilitating a broad spectrum of applications [9]. Common applications of the top-down approach include metabolic engineering, where existing microorganisms are engineered to produce valuable chemicals, fuel or pharmaceuticals [10, 11]. It is used in agriculture for enhancing crop traits, such as disease resistance or increased yield, in existing plant varieties. Additionally, it has been applied to environmental remediation, including the cleanup of polluted soils, and has participated in making significant contributions to medicine, improving diagnostic methods and treatment approaches.

One of the limitations of the top-down approach remains in the reliance on the cellular resources and machinery of the host organism. The addition of non-natural genes can create a resource competition and burden in the host, which can lead to reduced growth rates, cellular stress, or even cell death [12-14].

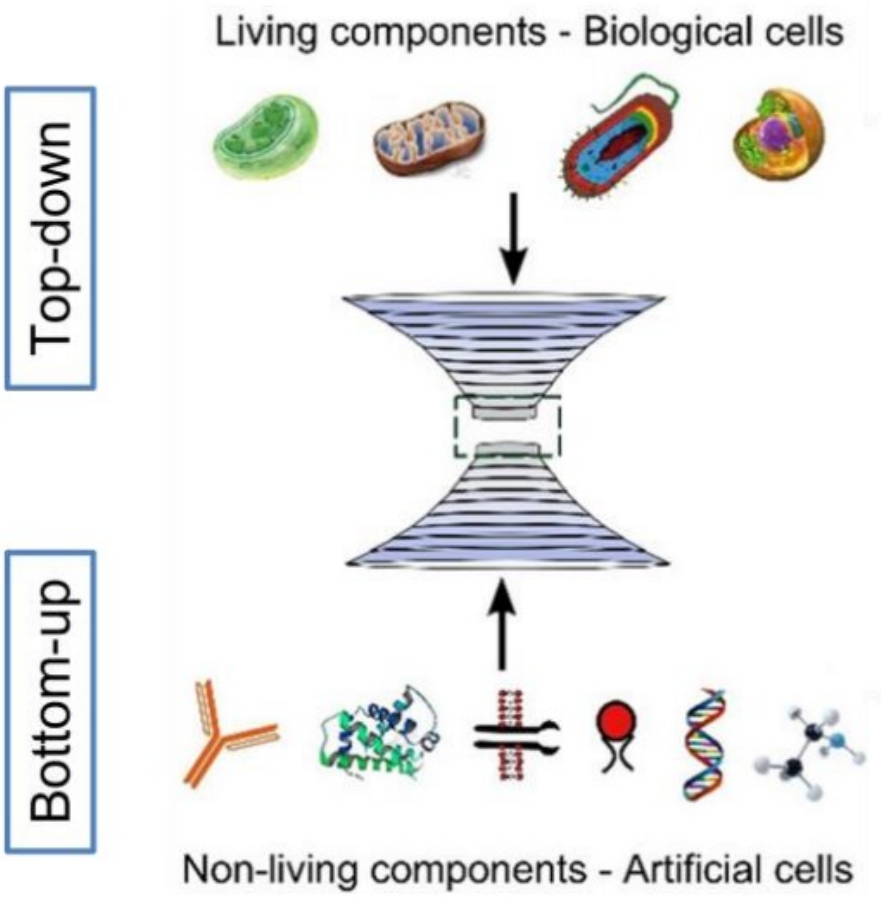


Figure 1.1 – Synthetic biology: the top-down versus bottom-up approach. The top-down approach consists in genetically engineering living systems, while the bottom-up approach is the assembling of non-living building blocks to create artificial cells. Source: [1].

The bottom-up approach aims to reconstruct biological systems from scratch, using basic cellular components such as phospholipids, DNA, RNA and proteins. These building blocks are assembled to create functional systems with tailored complexity and functionality [15]. With this approach, cellular behaviours such as movement, metabolism, division, sensing and response can be achieved. In the field of synthetic biology, these systems have been referred to as synthetic cells, minimal cells or artificial cells [16].

Artificial cells offer some advantages compared to engineered organisms, as they are not living systems. This implies that they are not subject to burden and competition for resources with natural functions. ACs also offer great flexibility in the design, as non-natural building blocks such as polymers or nanoparticles can be incorporated into the system, creating new functions without putting at risk the cell viability. Finally, the

simplicity of these systems makes them highly programmable, controllable, and predictable.

ACs are used for research purposes to better understand the origin of life from non-living building blocks to a truly functional and autonomous system [17]. They are also used for fundamental research, where protocells (simplified versions of living cells) are employed to better understand biological processes by adding one parameter at a time [18]. Finally, artificial cells have the potential to be employed as micromachines for applications in drug delivery, tissue engineering or environment remediation [1].

Some limitations of ACs are that they lack the complexity to achieve more complex functions such as infinite replication, or self-repair [19, 20]. Research on ACs has been focusing on developing its functionalisation, to widen the possibilities of applications and the complexity of tasks performed by the cell.

1.3. Biological and artificial membranes

Cells of all biological systems are compartmentalised by a membrane separating the inside of the cell from its environment. The role of this semi-permeable membrane is to protect the inner components, control the material exchange in and out of the cell, sense extra-cellular signals, and allow movement [21, 22].

1.3.1. Biological membrane structure

Biological membranes are made of a phospholipid bilayer composed of different types of phospholipids, which differ in their headgroups, tail lengths, and unsaturation [23, 24]. Additionally, sterols and non-phospholipids (sphingosine lipids and triglycerides) are also membrane components. The last component found in lipid bilayers are proteins, categorised as integral, peripheral, and anchoring proteins [25, 26]. Integral proteins are embedded within the lipid bilayer and facilitate material exchange between the cell and its environment. They possess both hydrophilic regions, exposed to the aqueous environment, and lipophilic regions within the membrane. Peripheral proteins are located on the membrane's surface through electrostatic interactions, or loosely bound to integral proteins. Anchoring proteins utilise a combination of lipid-protein interaction or protein-protein interaction to tether themselves to the lipid bilayer.

Biological membrane models have evolved over time, with the fluid mosaic model, developed by Singer and Nicolson in 1972, being the most widely accepted [27]. In this model, the membrane is composed of a fluid lipid bilayer in which proteins are embedded or located on the surface (Figure 1.2). The lipid bilayer is composed of a double layer of phospholipids, where hydrophobic tails are directed inwards, away from the aqueous environment, and hydrophilic heads face outwards, in contact with the aqueous milieu [28, 29]. This structure creates a two-dimensional fluid where lipids and other molecules can move laterally within the membrane. In an update from Nicolson (2013) on the original fluid mosaic model, lipid rafts were introduced. Lipid rafts consist of microdomains enriched in lipids such as cholesterol, glycolipids, and sphingolipids and can form occasionally in the membrane [30, 31]. These microdomains confer rigidity to the membrane through a more ordered less fluid environment, serving as a platform for various cellular processes such as cell signalling, membrane dynamics and cell-cell communication. Some biological membranes have shown membrane asymmetry, with a differential distribution of lipids within the inner and outer leaflets [32, 33]. In eukaryotic cells, phosphatidylcholine and sphingomyelin are often more abundant in the outer leaflet, while phosphatidylethanolamine, phosphatidylserine and phosphatidylinositol are predominantly found in the inner leaflet. The asymmetries are essential for maintaining membrane structure and functions [34].

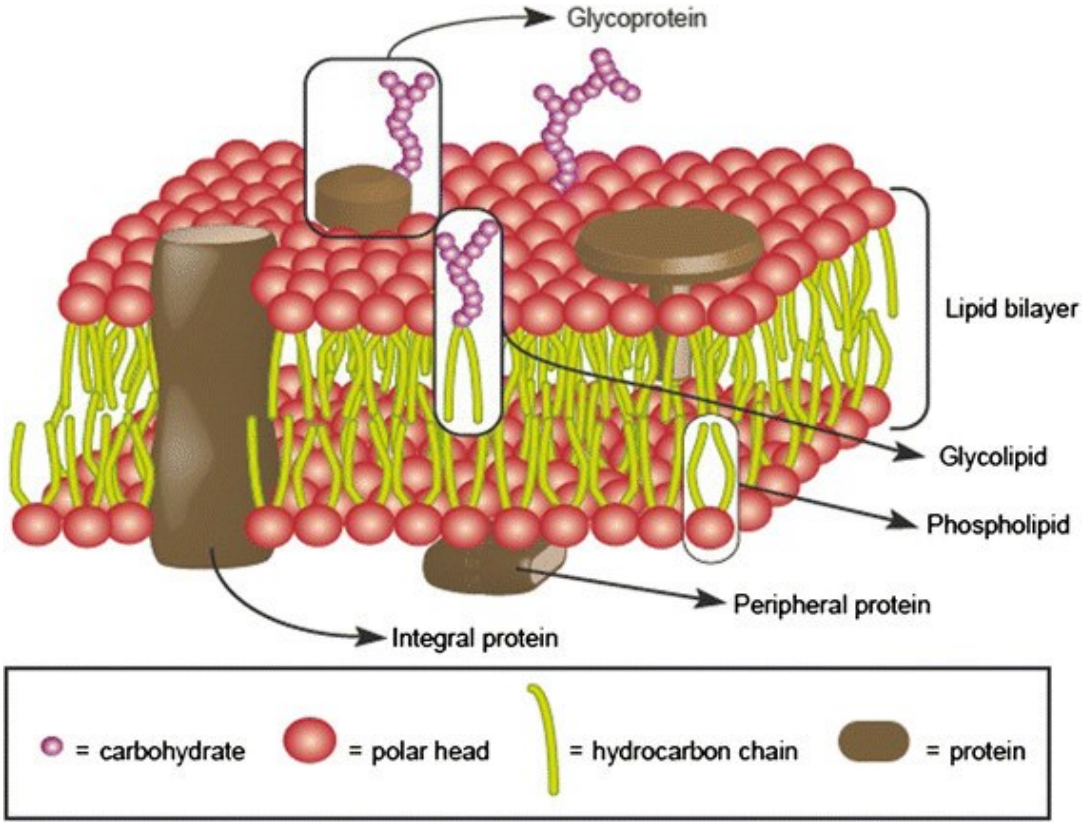


Figure 1.2 – The fluid mosaic model proposed by Singer and Nicolson. Biological membranes are composed of fluid lipid bilayers embedding proteins. These dynamic structures resemble a mosaic pattern. Source: [26]

1.3.2. Types of lipids

Phospholipids are the main components of biological membranes, that self-assemble into lipid layers (mono or bilayers) due to their amphiphilic characteristics. They are composed of a polar head group and a hydrophobic tail composed of one or two fatty acid chains. There is a large variety of headgroups found in biological membranes such as choline, ethanolamine, serine and inositol [35, 36]. The headgroups are linked to the fatty acid chains through a covalent bond between the phosphate group and the backbone of the headgroup (glycerol or sphingosine). Fatty acid chains also offer a large variety, depending on the length and the levels of unsaturation, with the most common ones in nature containing 16 to 22 carbon atoms and 0 to 6 unsaturated bonds (Figure 1.3) [37]. Cholesterol is a sterol with a bulky structure, that plays a fundamental role in the membrane fluidity and stability of mammalian cells [38]. Glycolipids contain a carbohydrate group attached to the hydrophilic head group and play a role in cell-cell

recognition and signalling. The most common ones are glycosphingolipids which are predominantly located in the outer membrane [39].

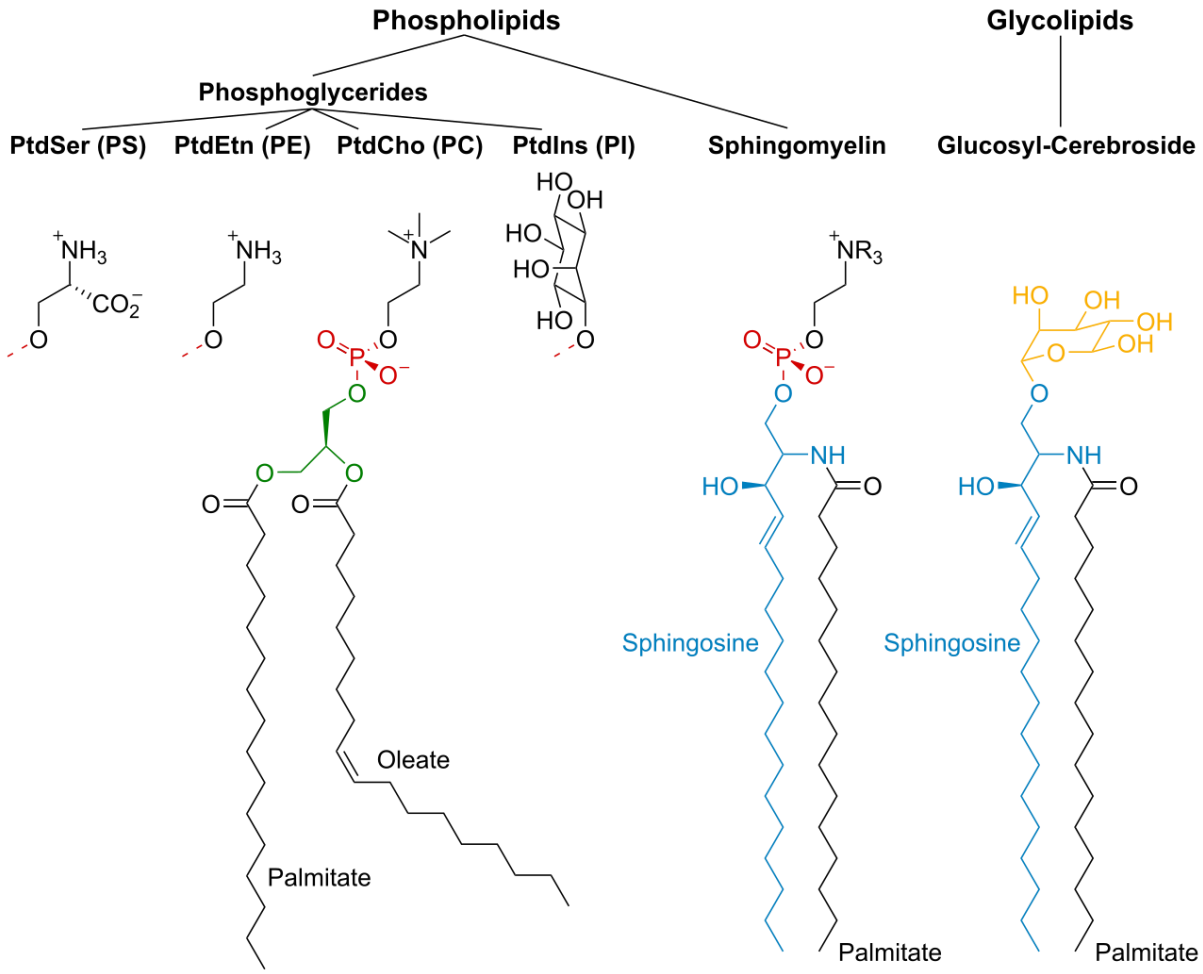


Figure 1.3 – Common lipids found in biological membranes. Hydrophilic heads are connected to hydrophobic tails through a phosphodiester bond between the phosphate group and the glycerol backbone. Source: Wikimedia Commons.

1.3.3. Lipid functions

Beyond their role of being a physical barrier, the lipids composing the biological membrane dictate the membrane fluidity and flexibility, ensuring a constant adaptation of the cell to the environmental stress, as well as adaptation to the different cellular processes. Lipids are also highly involved in the selective permeability of the membrane as they control the passage of ions, small molecules and proteins in both directions (endocytosis and exocytosis) [40]. Cell signalling is also dependent on lipids, as they act

as signalling platforms and can regulate the activity and localisation of signalling proteins. Finally, lipids (glycolipids) act as recognition sites and promote cell-cell interactions.

1.3.4. Membrane asymmetry

Biological membranes often show an asymmetrical distribution of the lipids across layers. While almost all types of lipids can be found in both leaflets, the specific amounts present in each layer can vary. One notable example is phosphatidylserine (PS) which is predominantly located on the inner leaflet, ensuring essential membrane functions. When the cell enters an apoptotic cycle, PS is translocated to the outer membrane, serving as a signal for macrophages [32, 33]. Another example is glycolipids such as glycosphingolipids that need to be primarily located in the outer leaflet, as they serve for cell-cell recognition and adhesion.

Asymmetry can also be temporary, as biological membranes are fluid and dynamic. They give lipids the freedom to move across one layer, but also to pass from one layer to the other, through membrane proteins: flippases move phospholipids from the outer layer to the inner layer, whereas floppases move phospholipids from the inside to the outside. Sramblases can move phospholipids in either direction. This is achieved by using the energy released from the hydrolysis of ATP (Adenosine triphosphate) to ADP (Adenosine diphosphate).

1.3.5. Membrane phases and curvatures

As stated earlier, there is a wide variety of biological membranes, especially due to the phospholipids that compose them, as well as the amount and distribution. In aqueous solution, lipids can be found in a variety of phases, depending on the morphology of the lipid, referred to as lipid polymorphisms. These phases are dependent on the chemical structure of the lipid, hydration levels of the membrane, ionic strength, pH, temperature, and pressure, with the objective of minimizing the hydrophobic repulsions of the lipid chains with the aqueous environment.

1.3.5.1. Lipid phases and membrane curvature

Lipid geometry can be classified into three types, depending on the packing parameter *P* [41, 42] (equation 1.1). This will determine the shape adopted by a lipid when incorporated into a mono or bilayer.

$$\boldsymbol{P = \frac{V}{a_0 \times l_c}}$$

Equation 1.1 – The packing parameter P is defined by this equation. V is the volume of the hydrophobic chain, lc is its length, and a0 is the area occupied by the headgroup.

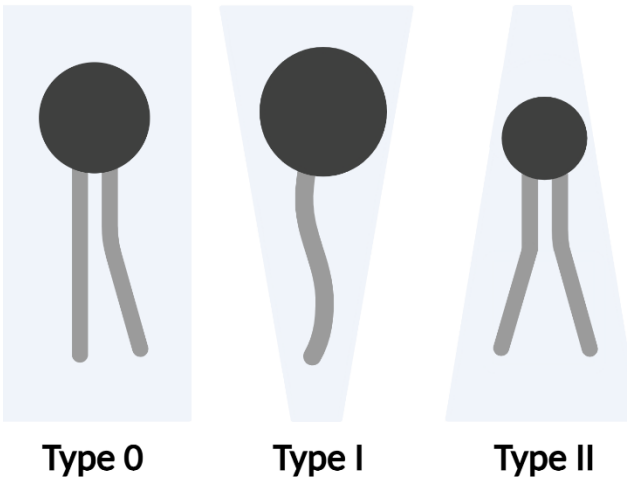


Figure 1.4 – Phospholipid polymorphism: the three main types of lipids based on the packing parameter P. Type 0 lipids have a cylindrical shape, type I lipids have and inverted conical shape, and type II lipids have a conical shape.

(i) Type 0 lipids have a cylindrical geometry in nature, with headgroup and chain groups of the same size. The packing number for this type of lipids is close to 1, and these lipids will tend to form planar lipid bilayers with no curvature or with a small bend. One examples of type 0 lipids is DOPC (phosphatidylcholine) [43].

(ii) Type I lipids have an inverted conical shape with their headgroups being larger than the chain groups. For these lipids, the packing parameter is superior to 1, forming micellar structures and or hexagonal (H_I) phases. Lysophopholipids are an example of type I lipids [44].

(iii) Type II lipids are conical, meaning that the headgroup is smaller than the hydrophobic tails. The packing parameter for this type of lipids lower than 1/3.

Some examples of type II lipids are DOPE (phosphatidylethanolamine), DOPS (phosphatidylserine) and DOPG, which tend to form inverted hexagonal (H_{II}) phases [45] (Figure 1.5).

The type of lipids will therefore impact the formation of the membrane, as well as the curvature. The lipids will also define the state of the lipid bilayer, in terms of mobility and organisation. Two distinct states are described: the gel phase (or solid phase), and the fluid phase (or liquid phase) [46]. The gel phase corresponds to a state where lipids are tightly packed with limited mobility, forming ordered structures with increased rigidity and decreased flexibility. This state is favoured at low temperatures. The fluid phase allows lipids to move laterally within the lipid bilayer, making the membrane more dynamic, flexible and adaptable. This phase is favoured at higher temperatures. The transition between the fluid phase and the gel phase is dictated by the lipid composition of the membrane, and more specifically by their transition temperature (Tm) [47]. Tm varies depending on the length and unsaturation of the lipids' hydrophobic chain [48]. Unsaturations in the chain lower the Tm, while a longer chain increases the Tm due to the Van der Waals interactions between chains.

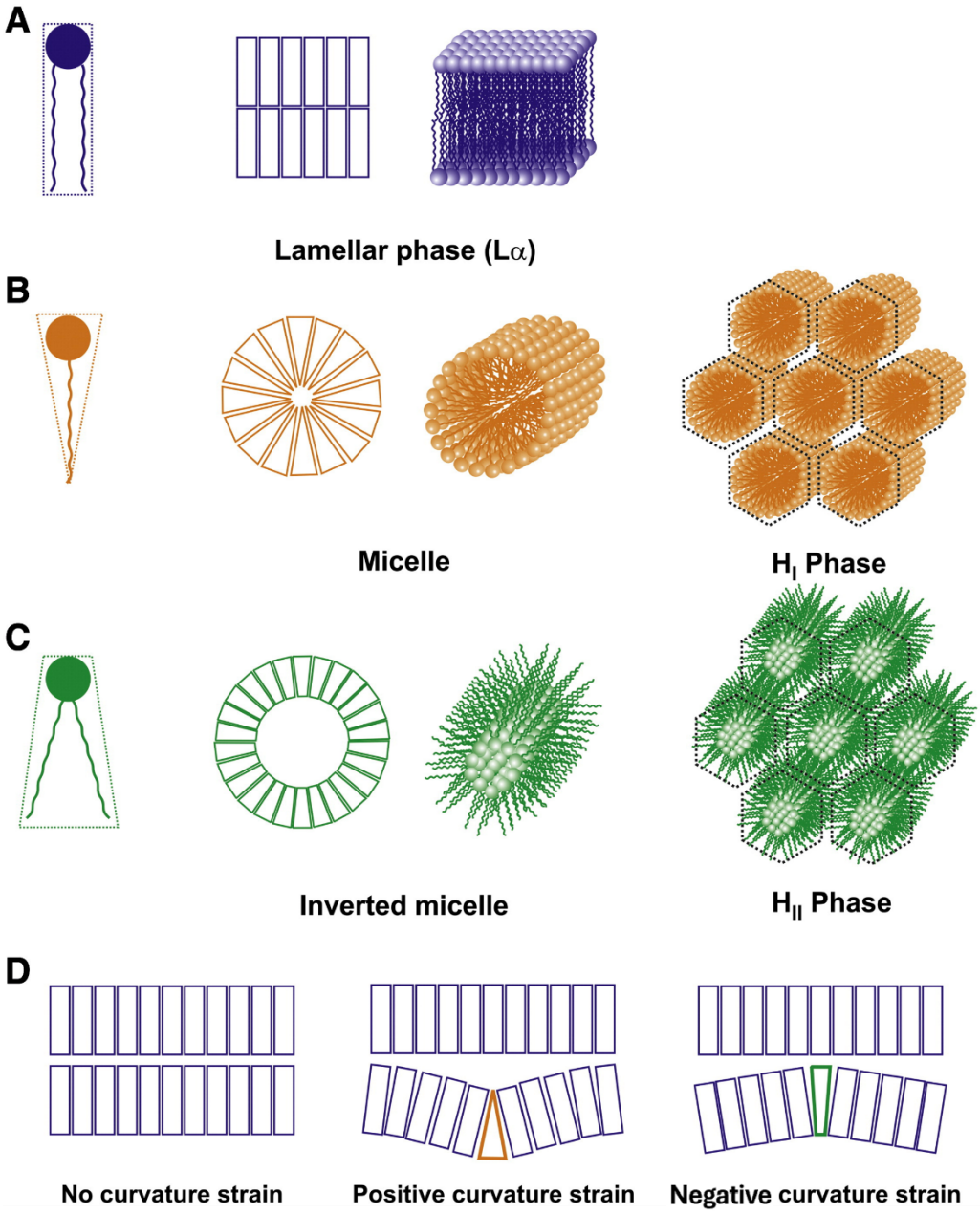


Figure 1.5 – Curvature, structures, and phases associated with each type of lipid. Source: [49]

1.4. Model membranes: vesicular systems

Three primary types of building blocks have been used to create model membranes: polymers for polymersomes, amphiphilic proteins for proteinosomes, and lipids for liposomes. Liposomes, being predominantly composed of lipids, have emerged as the most extensively studied system and are regarded as the optimal model. They can also serve as a platform for the incorporation of other building blocks such as polymers and proteins. Hence, lipids, are used in this research.

1.4.1. Artificial cells chassis

Phospholipid-based artificial cells are delimited by a lipid bilayer membrane. These vesicles are the starting point for the development of artificial cell systems. Two important factors can be tuned while making vesicles, depending on the purpose: the lamellarity and the diameter of the vesicles [50]. Depending on the number of bilayers, vesicles can be described as unilamellar (one bilayer), bilamellar (two bilayers), or multilamellar. Regarding the size, vesicles fall into three categories: small, large and giant vesicles (Figure 1.6). Small unilamellar vesicles (SUVs) (<100 nm) are usually produced by extrusion techniques, large unilamellar vesicles (LUVs) (between 100 nm and 1000 nm) are also extruded using bigger pores, and giant unilamellar vesicles (GUVs) (>1000 nm) are generate in bulk by electroformation, gel assisted swelling or emulsion phase transfer [51, 52]. Moreover, microfluidics can be applied to generate vesicles of all sizes [53]. Both LUVs and GUVs are used in this research and the techniques used to generate them are detailed in Chapter 2 – Methods.

In this research, more complex structures such as nested and multicompartment vesicles are employed. Nested vesicles are vesicles, usually GUVs, containing smaller vesicles inside the lumen which can be used for compartmentalisation. Multi-compartment vesicles are formed by vesicles binding to each other [54].

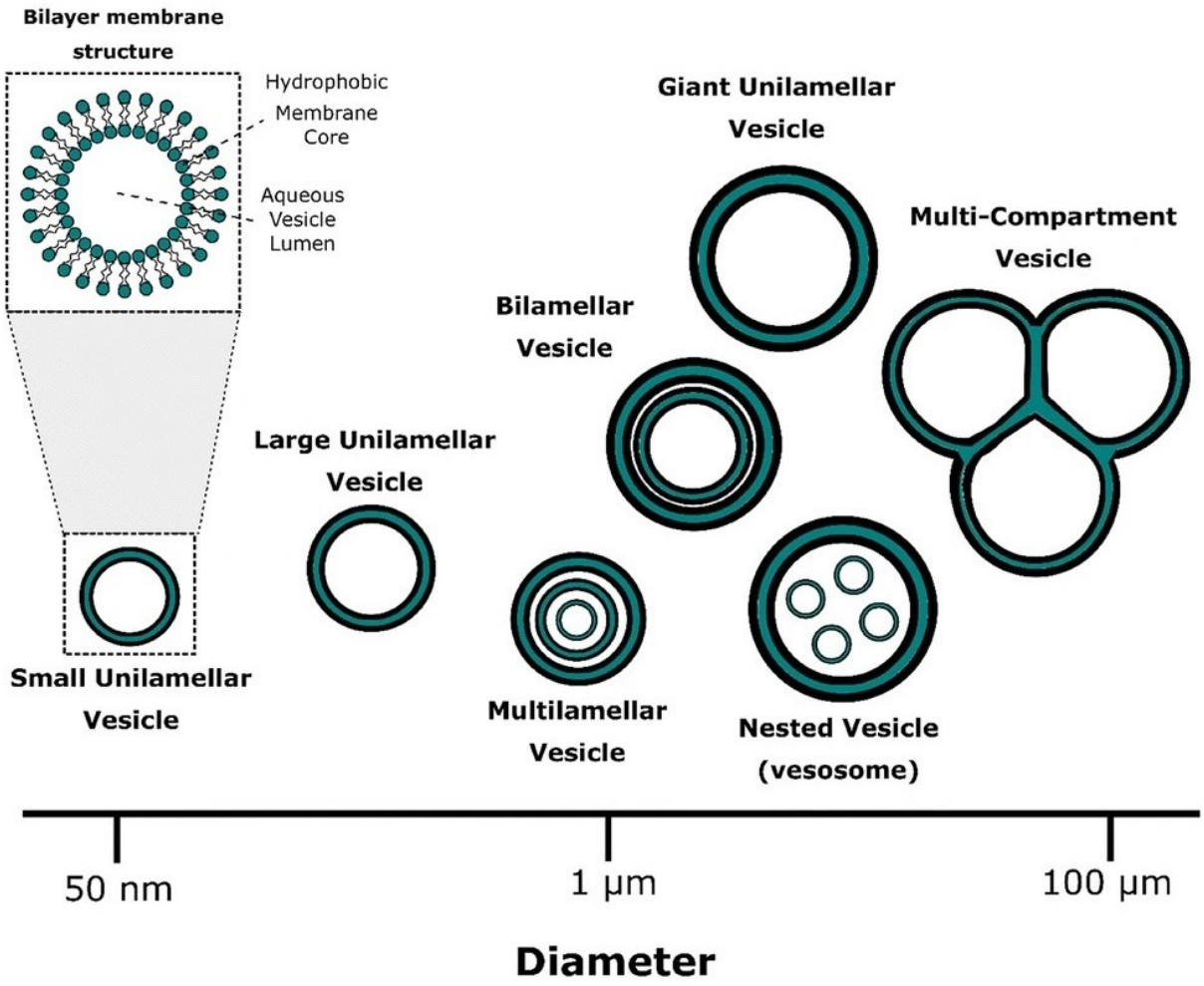


Figure 1.6 – Lipid vesicle classification. Liposomes are classified according to their level of lamellarity, as well as their diameter. The most frequent vesicles are SUVs (small unilamellar vesicles), LUVs (large unilamellar vesicles) and GUVs (giant unilamellar vesicles). Source : [55].

1.4.2. Membrane functionalisation

Artificial cell membranes represent an ideal platform for cell functionalisation, as functional lipids, proteins, or other molecules can be incorporated into the membrane. A variety of tools for functionalities have already been described [15, 55, 56]. The incorporation of membrane proteins has been used to mimic natural cellular processes such as transport, and biomolecules such as antibodies or enzymes have been used to create specific recognition sites for binding or biosensing. Nanoparticles have also been incorporated into the membrane for biomedical applications. Finally, lipids have been chemically modified to introduce specific chemical groups relevant to the desired application. Despite all the work that has already been done, membrane functionalisation for artificial cells is still a bottleneck, and developing new tools will

participate in making advances in the field. One approach to developing membrane functionalisation is through the lipids involved in the formation of the artificial cell, particularly the headgroup. By modifying the lipid headgroup, various functionalities can be achieved within the membrane, depending on the chemical properties of the headgroup. For instance, incorporating an imidazole function into the headgroup could facilitate interactions with other compounds (such as his-tagged proteins). Introducing an aldehyde function on the headgroup could attract amino functionalities, while a nucleotide headgroup might promote the formation of hydrogen bonds similar to those found in DNA. Similarly, a thiol function could lead to the creation of disulfide bridged resembling those found in proteins.

Therefore, developing a platform to synthesise artificial phospholipids with specific functionalities would be a huge step-forward in the development of membrane functionalisation and artificial cells.

1.4.3. Membrane fusion

Membrane fusion is key to biological functions where cells or liposomes are brought together to create larger structures, with mixed membranes and inner content. Understanding and finding ways to control membrane fusion is crucial to reproducing biological behaviours or imagining new applications for artificial cells, such as recreating endocytosis or enhancing cell-cell communication [57, 58]. Membrane fusion happens in nature through proteins and peptides, through small fusogenic molecules or ions [59]. In this research, ion-induced fusion will be the principal focus.

The presence of certain divalent ions has been shown to induce fusion in artificial membranes. Among all, Ca^{2+} and Mg^{2+} are the most studied ones and promote membrane fusion by interaction with negatively charged membranes [60]. The binding of positively charged ions to lipids changes the polarity of the surface, modifying the repulsion forces between two membranes. This establishes an instability in the membrane, facilitating membrane fusion (Figure 1.7). The lipid composition of the membrane also plays a crucial role in membrane fusion, as the lipids need to adopt some levels of bending and curvature for the membranes to fuse [61] . Phosphatidylethanolamine (PE), phosphatidic

acid (PA), phosphatidylserine (PS) and cardiolipin (CL) have been shown to induce membrane fusion in the presence of Ca^{2+} and Mg^{2+} [60]. Other biologically relevant divalent ions (Zn^{2+}, Mn^{2+}, La^{3+}) have been shown to promote membrane fusion [62]. Understanding and inducing fusion in a controlled manner would unlock new applications for artificial cells, for biomedicine or biotech.

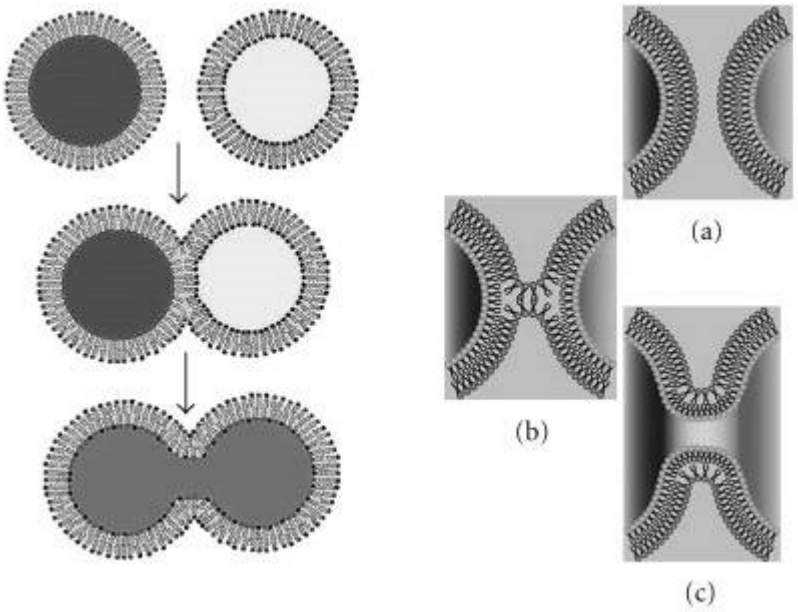


Figure 1.7 – The three main steps in membrane fusion with (a) vesicles attracted to each other and making contact through their membranes, (b) inter-membrane lipid mixing (c) mixing of the inner content of vesicles Source: [59].

1.5. Lipid synthesis

1.5.1. Organic and biochemical synthesis

Phospholipids were traditionally synthesised using organic chemistry methods such as the Baer and Fischer technique, which involves many intermediary steps and is performed in harsh conditions [63-65]. These organic chemistry techniques also involve the use of large amounts toxic solvents (organic solvents, metal catalysts), which in turn, complexify the purification steps, decrease in yield and increase the production cost. Biochemical synthesis of phospholipids offers an alternative to chemical synthesis, with a few advantages. It involves the use of enzymes, implying a very high specificity for the reaction, mild conditions, and little amounts of deleterious solvents [66]. The product purification is simplified, losses are reduced, and phospholipids are safer to use for the food, pharmaceutical and cosmetics fields.

Biochemical synthesis offers a more sustainable way to synthesise phospholipids and responds to most of the green chemistry principles.

Green chemistry was introduced at the end of the 20th century, as a response to the negative effect of polluting industries (textile, dyes, chemicals, steel) on the environment and human health [67]. This concept has been created to minimize the use of hazardous substances, reduce the generated waste, and energy consumption to create more sustainable processes [68].

Green chemistry is based on 12 principles developed by Anastas and Warner in 1998 [69]: (i) waste prevention, (ii) atom economy, (iii) less hazardous chemical synthesis, (iv) designing safer chemicals, (v) use of benign solvents and auxiliaries, (vi) energy efficiency, (vii) use of renewable feedstock, (viii) reduce derivatives, (ix) use of catalysis, (x) design of degradation, (xi) real-time analysis for pollution prevention, and (xii) accident prevention. Biological methods have been widely used to replace some chemical processes, using natural enzymes [70, 71], bacteria [72], fungi [73] or engineered microorganisms [74] to generate the product of interest. They offer several advantages such as operation in milder reaction conditions, they are very selective, and lower environmental and physiological toxicity. This is the case for lipid synthesis, where enzymes have been extensively utilised and developed for industrial applications, in pharmaceuticals or in biofuels.

1.5.2. Phospholipase enzymes

Phospholipases are an essential group of enzymes that hydrolyse phospholipids (PLs), generating a certain product depending on the class of enzyme. Phospholipase A (PLA) hydrolyses the ester bond at the sn-1 (PLA_1) or sn-2 position (PLA_2), releasing respectively a fatty acid molecule and generating a lysophospholipid [75]. Phospholipase B (PLB) combines the activities of PLA_1 and PLA_2. Phospholipase C (PLC) hydrolyses the phosphodiester bond, releasing a diacylglycerol and a phosphorylated head group. Finally, phospholipase D (PLD) catalyses the hydrolysis of phospholipids by cleaving the phosphodiester bond between the phosphate group and the headgroup, generating phosphatidic acid (PA) and the corresponding free headgroup (Figure 1.8) [76]. PLD has

been chosen for this research project, for the synthesis of novel lipids, which will be further discussed.

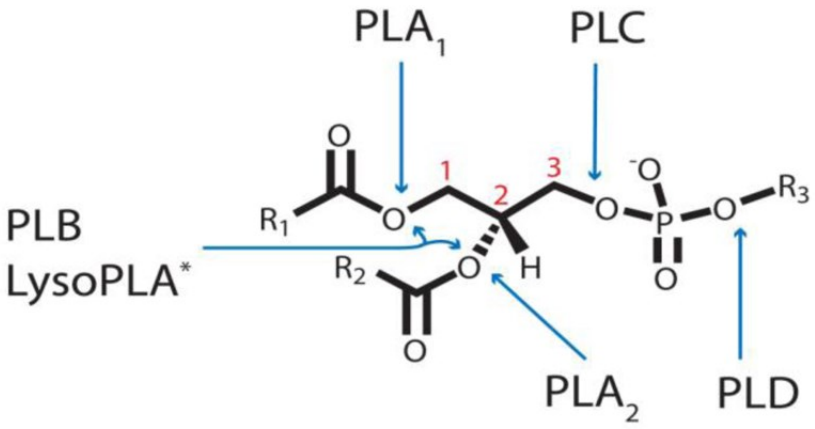


Figure 1.8 – Phospholipases and their cleaving sites. PLA and PLB hydrolyse the ester bond, while PLC and PLD hydrolyse the phosphodiester bond. Source: [77]

1.5.3. Phospholipase D and transphosphatidylation

PLDs belong to the enzyme family of phosphodiesterase and are found in nature in a large variety of organisms including animals, plants, bacteria and fungi [78]. The formation of PA (phosphatidic acid) generated by the reaction plays an important role in cell signalling, for processes such as cell proliferation, cytoskeletal rearrangement, and cell survival in eukaryotic cells [79]. In bacteria, PLDs are usually responsible for their virulence.

Under certain conditions and in the presence of hydroxyl-containing substrates, usually alcohols, PLDs can show a transphosphatidylation activity, where the lipid headgroup is exchanged with the function carried by the substrate [80]. This leads to the formation of a new phospholipid. For example, in the presence of ethanolamine, phosphatidylethanolamine (PE) is formed. Phosphatidylserine (PS) plays an important role in neurological processes, and for this reason, has generated interest in the biomedical industry [81]. PS has been successfully synthesised through transphosphatidylation from DOPC as starting material [82]. PE can also be generated through this enzymatic reaction and has shown to be more efficient than chemical processes [83, 84]. PE is one of the most common phospholipids in eukaryotic cells and has been associated with diseases such as Alzheimer's, Parkinson's and non-alcoholic liver disease [85] (Figure 1.9).

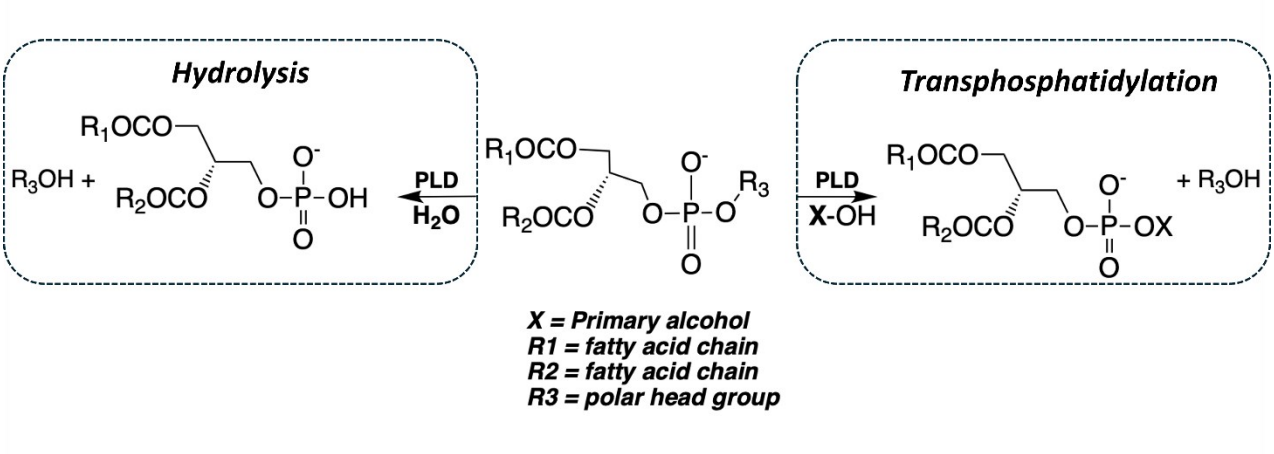


Figure 1.9 – PLD transphosphatidylation and hydrolysis competing reactions. The transphosphatidylation reaction will generate a new phospholipid on the presence of a primary alcohol, while the hydrolysis reaction will generate PA in the presence of H_2O.

However, not all the PLDs can do transphosphatidylation. The PLD superfamily is divided into two groups, the HKD PLDs and non-HKD PLDs. The HKD PLDs carry a conserved HKD motif (Histidine, Lysine, Aspartic acid) in the catalytic site, with the histidine playing an important role in the enzymatic activity [86, 87]. These are the PLDs capable of catalysing the transphosphatidylation reaction. Some non-HKD PLDs have also shown catalytic activity on phospholipids. Among the HKD PLDs, many PLD strains, especially from bacteria, have been studied and used for industrial applications. It is difficult to compare PLD strains, as the activity of the enzyme will be dependent on many factors such as the alcohol used, the solvent and the reaction conditions [88]. PLD from *Streptomyces* species have displayed the highest transphosphatidylation activity among all bacterial PLD, and for this reason, it has been widely used for the synthesis of artificial and natural lipids at industrial scale and will also be used in this research for the synthesis of a novel lipid [84].

1.5.3.1. Proposed synthesis reaction

To synthesise the desired novel phospholipid for this research, PLD was used, with a primary alcohol, L-Histidinol as the substrate. The proposed reaction (A) and novel phospholipid generated (B) are displayed in Figure 1.10. The goal is to synthesize a phospholipid carrying an imidazole group, capable of chelating metal ions. Similarly to protein purification columns, our imidazole-lipid would be a platform for other his-

containing moieties such as his-tagged proteins [89]. L-Histidinol is an ideal substrate for the reaction as it is a primary alcohol, it carries an imidazole group for functionality and an amine group for monitoring the reaction. L-Histidinol is also a naturally occurring compound involved in the biosynthesis of L-Histidine, making the lipid more compatible for biomedical applications [90].

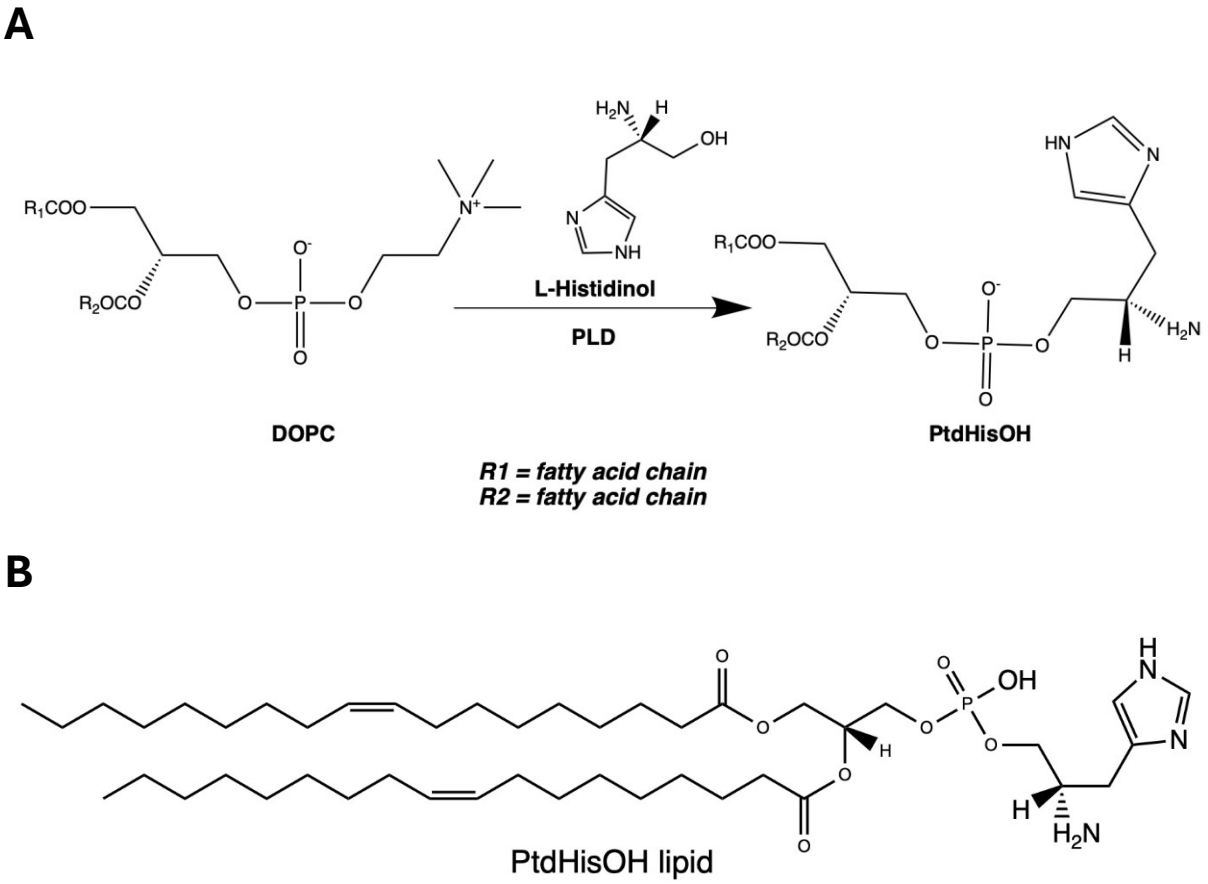


*Figure 1.10 – Proposed transphosphatidylation reaction (**A**) for the synthesis of the novel phospholipid (**B**) using L-Histidinol as the substrate.*

1.6. Imidazole catalysis

Imidazole is a nitrogen-containing heterocycle ring, found in important natural products such as histidine, histamine, purines, biotin and nucleic acids. Despite being small, imidazole has a unique chemical complexity, as it is both a good donor and acceptor of hydrogen bonds through its two nitrogen atoms [36]. Imidazole is widely used for chemical synthesis as a catalyst for hydrolysis (phenyl acetates, sucrose [91, 92]), and hydrolysis has shown to be

boosted in the presence of metal ions such as Cu^{2+} and Zn^{2+} [93]. Imidazole is also used as a catalyst for the transfer of activated acyl groups and nitro-aldol reactions [94, 95]. Understandably, imidazole has been utilized to build artificial enzymes, including ribonucleases [96, 97], acylases [98] and esterases [99, 100].

Histidine is an essential amino acid that plays a crucial role in biological enzymatic reactions, through their imidazole group contained in the side chain. In enzymes, histidines can coordinate with metal ions, stabilising the reaction intermediate and providing a platform for the substrate to bind the enzyme [101-103]. For example, histidines have been found in the catalytic sites of esterases [101], proteases [104], phosphatases [105] and decarboxylases [102]. Histidine is also essential in metalloenzymes as it captures the metal ions that serve as cofactors for the reaction [106].

Imidazole has been employed in the context of liposomes, as a tool for pH detection [107, 108] and for nanodelivery of nucleic acids [109], but there is no current work showing catalytic properties of an imidazole-containing lipid in the context of artificial cells.

By synthesising an artificial lipid carrying an imidazole group, catalytic properties are expected. This offers a new range of applications of the lipid in artificial cells. PtdHisOH could be employed to mimic biological functions such as cell-signalling or creating microreactors for localised enzymatic-like reactions [110, 111].

1.7. Aim & objectives

Cell functionalisation is crucial in artificial cells and therefore, necessitates the development of new tools to functionalise the membrane. One approach is to modify the lipid headgroups involved in the formation of the artificial cell bilayer. To explore this route, we aim to synthesise, characterise, and apply a newly functionalised lipid, thereby adding functionality to a membrane. This will involve the incorporation of histidine, a well-known amino acid used in catalytic enzymes. Catalytic abilities of the novel lipid will be investigated, as well as its potential as a binding tool for interacting with metal-dependent entities. This will be pursued through four objectives:

(i) Develop and scale-up the synthesis of phosphatidyl-histidinol artificial lipid through enzyme-assisted synthesis.

(ii) Characterise the new lipid metal-binding functionality by developing a high throughput assay.

(iii) Investigate the catalytic abilities of the novel lipid in the context of lipid presentation and specificity/dependency.

(iv) Use the novel lipid in the context of artificial cells and develop experiments for proof of concept of protein-coated artificial cells, metal-induced interactions between cells, and catalytic microreactors.

2. Chapter 2: General Materials and methods

This chapter outlines the general methods and procedures used throughout this research project. Variations in the standard procedures, or additional steps specific to an experiment, will be pointed out in the relevant chapters. The optimal conditions for the experiments developed will be shown in this chapter, while the optimisation process will be described in the relevant results chapter.

2.1. PtdHisOH lipid synthesis

2.1.1. Lipids

All lipids used in this thesis were purchased from Avanti Polar Lipids, Inc. (USA). The structures and chemical names of the lipids are listed in Figure 2.1. The lipids were either purchased in chloroform and stored at -20°C in glass vials, or they were acquired as powder and stored as 20 mM stock solutions in chloroform at -20°C in glass vials.

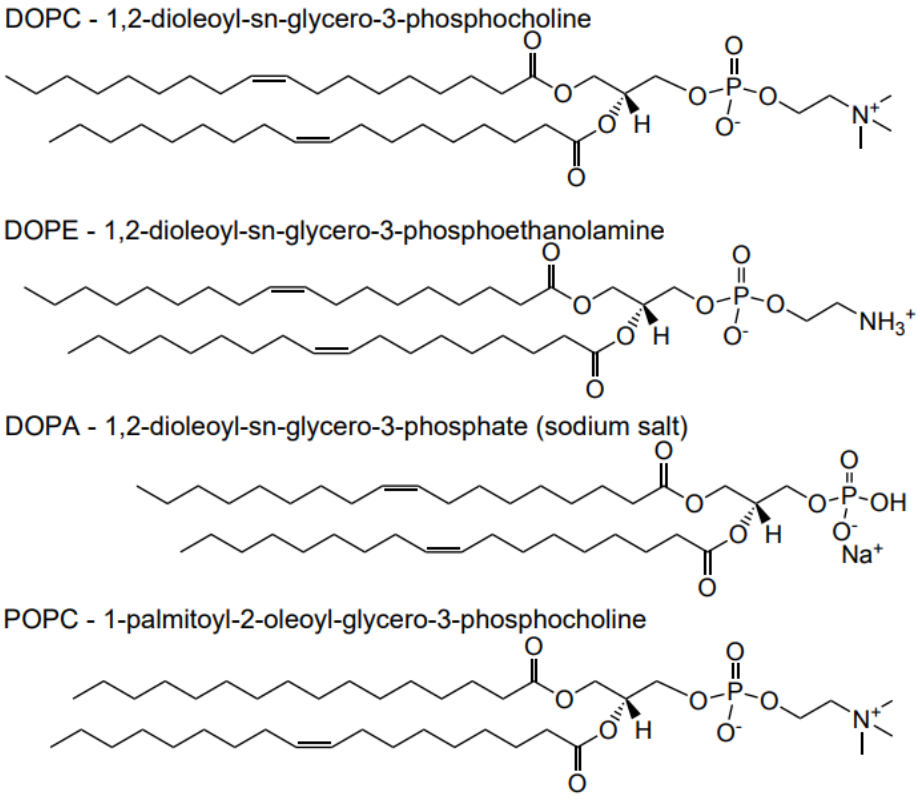


Figure 2.1 – Chemical structure of phospholipids used in this research project.

DOPC is used as starting material for the synthesis, DOPC, DOPE and POPC are employed in LUVs and GUVs generation, and DOPC and DOPA used for TLC standards.

2.1.2. Lipid coating

For experiments requiring coated lipids on 96-well plates, 10 mM stocks of DOPC lipids in chloroform : methanol (ratio 1:1.5 v/v) were prepared. 10 µL of this stock is deposited at the bottom of each well of a white polystyrene 96-well plate (BRANDplates®), using a multistep pipette. The plate is airdried for 30 minutes in a fume hood, on a microplate shaker at 1200 rpm.

2.1.3. Synthesis in the coating system

The transphosphatidylation assay in the coated system was developed by H. Yang (2022) [112], and adapted towards the histidinol alcohol acceptor for this research. The section below describes the optimised standard conditions (optimisation in section 3.1 - Chapter 3).

For a standard reaction in the coated system, 10 µL of 10 mM PC in $CHCl_3$: MeOH (1:1.5 v/v) are coated on the bottom of a white 96-well plate, as outlined in section 2.2.1.

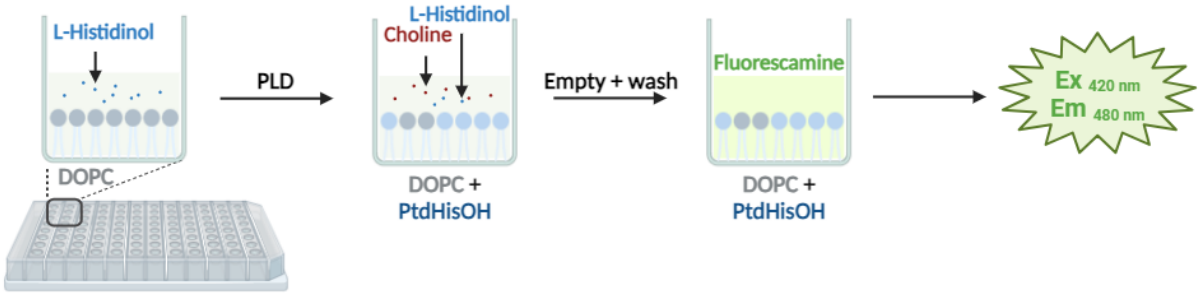


Figure 2.2 – Standard protocol for transphosphatidylation in the coating system. PC is coated on a 96-well plate and topped up with buffer containing PLD, L-Histidinol and BSA. After a 30 min incubation at 37°C, the plates are emptied and washed with buffer and H_2O. Fluorescamine is then added to detect the presence of primary amines by fluorescence.

The main steps for the standard protocol of transphosphatidylation in the coated system are depicted in Figure 2.2. In each well, 50 µL of a mixture containing 100 mM sodium acetate buffer at pH 5.6, 0.02 units of PLD from *Streptomyces sp.*, and 400 mM L-

Histidinol prepared in the same buffer is added. The plate is then incubated at 37°C in a shaking incubator for 20 minutes. Following the reaction, the solution is removed, and the wells are washed three times with 100 µL of buffer, followed by three washes with ultrapure water. This step ensures the removal of all unreacted L-Histidinol and accumulated choline, leaving only the coated lipids in the wells.

2.1.4. Detection of the product

To detect the product, 50 µL of HPLC-grade water is added to each well, followed by the addition of 50 µL of a 5 mM Fluorescamine in acetone (Tokyo Chemical Industry Co.). Fluorescamine stocks solution in acetone were stored at 4°C. Fluorescamine reacts with primary amine moieties present in the newly synthesized PtdHisOH and becomes fluorescent [113] (Figure 2.3). The plate is shaken for 5 seconds, and the fluorescence is monitored over time using a SpectraMax M3 spectrometer, with $Ex_{420\ nm}/Em_{480\ nm}$ and at room temperature. The Fluorescamine reaction is monitored for 120 minutes or until saturation is reached, and the endpoint value is saved.

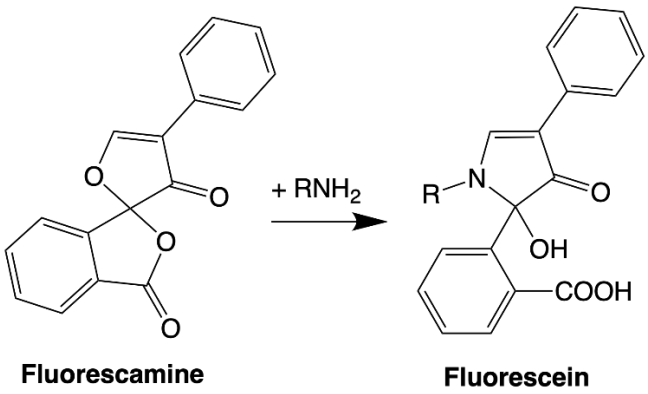


Figure 2.3 – Fluorescamine reacts with primary amines and becomes fluorescent.

Yields for the reaction are calculated based on the L-histidinol calibration curve, depicted in Figure 2.4.

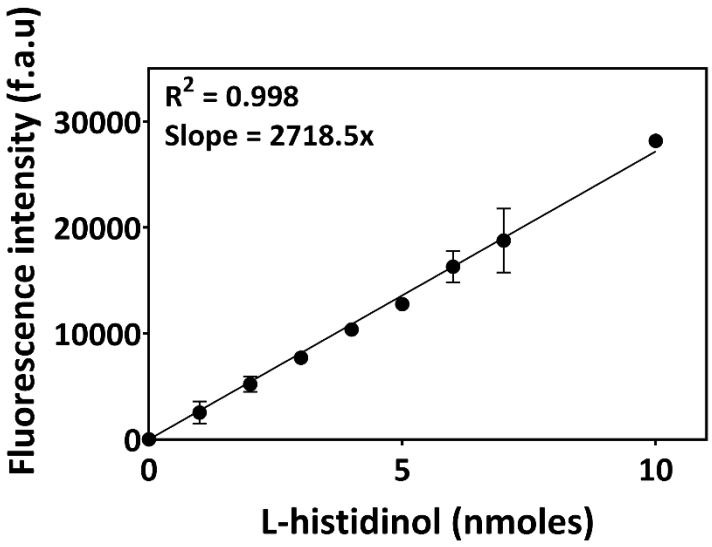


Figure 2.4 – L-Histidinol calibration curve with fluorescamine. Increasing amounts of L-Histidinol in sodium acetate pH 5.6 are mixed with 2.5 mM fluorecamine in acetone. The reaction is monitored at room temperature with a spectrometer at $Ex_{420\ nm}/Em_{480\ nm}$ until saturation, and the endpoint value is plotted. The graph shows the average of 6 replicates from 3 independent experiments (n = 6) and standard deviation is represented in error bars.

2.1.5. Scaling-up the reaction

2.1.5.1. Synthesis in the 2-phase system

The 2-phase system will be used for scaling up the reaction, and therefore, the reaction is first tested at a similar scale, comparable to the coating system [114, 115].

For the transphosphatidylation in the two-phase (or biphasic) system, the reaction is conducted in 2 mL Eppendorf LoBind tubes, with 100 µL of aqueous phase and an equal volume of organic phase. The aqueous phase is composed of 100 mM sodium acetate buffer at pH 5.6, 0.02 units of PLD, and 400 mM L-Histidinol (prepared in the same buffer and adjusted to pH 5.6). The organic phase contains 2 mM DOPC in chloroform.

The two phases are combined in an Eppendorf tube and incubated horizontally in a shaking incubator at 330 rpm, 37°C, for 20 minutes. This positioning enhances the exchange surface between the two phases.

After 20 minutes, the tubes are centrifuged at 13,000 rpm for 3 minutes to separate the two phases, and 50 µL of the organic phase containing the product is collected. The product is then coated onto a 96-well plate and detected using fluorescamine. Yields are calculated based on the calibration curve from Figure 2.4.

2.1.5.2. Scale-up synthesis

To accumulate more PtdHisOH lipid per reaction, the lipid production was scaled up from the microliter scale to the millilitre scale as illustrated in figure 2.5 [115]. The two-phase system is employed, with up to 10 mL of each phase. The reaction is conducted in a 50 mL round-bottom flask and incubated for 20 to 40 minutes on a hot plate at 37°C, with a stirrer bar for agitation at 250 rpm.

Once the reaction is complete, the content of the flask is distributed into Eppendorf tubes and samples are centrifuged, to aid the separation of the phases. The organic phase containing the product is then collected and stores at -20°C in a glass vial.

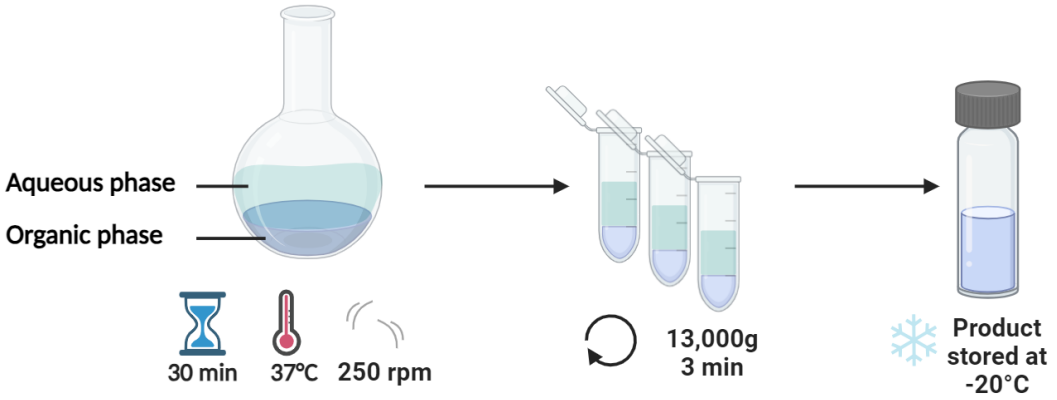


Figure 2.5 – Standard protocol for transphosphatidylation in the 2-phase system (scale-up). An aqueous solution containing the enzyme and the alcohol in sodium acetate buffer is mixed with an organic solution containing PC in chloroform (1:1 volume ratio). The synthesis is carried out for 30 minutes at 37°C and 250 rpm. After the reaction, the two phases as separated by centrifugation and the product is collected in the organic phase.

2.2. Chemical characterisation of the synthesized lipids

2.2.1. TLC analysis & stains

One step in the validation of the new product is to conduct Thin Layer Chromatography (TLC), comparing the new product with standards. TLC is a chromatographic method used to separate and analyse mixtures of compounds according to their solubility in the solvent. The sample is deposited on a plate, the stationary phase, which is eluted in a solvent mixture known as the mobile phase. The solvent migrates by capillary action up the plate, carrying the samples at different rates according to their partition coefficients. Retention factors can then be calculated to identify the products, as described in Equation 1. [116].

A 2 µL aliquot of the product from the two-phase system or of DOPC and DOPA standards is spotted onto a TLC plate (silica gel 60 matrix from Sigma-Aldrich). The plate is then developed into a chamber containing the eluent composed of Chloroform : Methanol : Ammonium hydroxide (65 : 25 : 4) [117, 118]. Once the eluent has reached the top, the plate is airdried in the fume hood for 5 minutes and stained with a solution of (i) Molybdenum blue [119], (II) Ninhydrin [120] or (III) Fluorescamine [121]:

(I) For Molybdenum blue (Sigma-Aldrich), 200 µL to 500 µL of reagent was applied to the surface of the plate, depending on its size. The colour development occurs in the dark for 5 to 10 minutes at room temperature, and the blue spots appearing on a white background correspond to the phospholipids.

(II) For Ninhydrin (Alfa Aesar), a stock solution is prepared by dissolving 0.3 g in 100 mL of ethanol with 3% acetic acid. The mixture is stirred at room temperature until the solution becomes clear. The TLC plate is immersed in the staining solution and air-dried at room temperature under the fume hood. To reveal the colour, the plate is then heated at 100°C for 3 minutes. Purple spots will appear against a white background, corresponding to the compounds carrying amines.

(III) For Fluorescamine, the plate is immersed in 5 mM Fluorescamine in acetone for 5 seconds, and airdried in the fume hood at room temperature. After 10 minutes, the fluorescence is revealed under a UV lamp, showing fluorescent spots in the presence of primary amines.

Using lipid standards and comparing the results from the different staining techniques, the R_f (retention factor) of each compound can be calculated according to the following formula (Figure 3.13):

$$Rf = \frac{Distance\ travelled\ by\ compound}{Distance\ traveled\ by\ solvent\ front}$$

Equation 2.1 – Retention factor Rf

2.2.2. Mini column chromatography

To purify the product PtdHisOH, which may contain DOPC (starting material) and DOPA (byproduct of hydrolysis), a mini column chromatography was prepared [122].

For the purification, a small column is made using a glass Pasteur pipette plugged with a small amount of cotton to prevent the silica gel from leaking out. The silica gel 60 (0.063-0.200 mm from Millipore Sigma) is packed into the column to a height of 3 to 5 cm.
The dry silica column is washed four times with 500 µL of the eluent of choice, usually the mobile phase used for the TLC (Chloroform : Acetone : Methanol : Acetic acid : Water - 65 : 20 : 10 : 10 : 3 v/v). The concentrated sample is then applied to the top of the column, representing a volume of 20 to 50 µL. 200 µL of eluent is added to the column, and the flow through is collected as a fraction. This step is repeated until 2 mL of eluent have flowed through the column. 2 µL of each fraction is deposited on a TLC plate to identify the fractions that contain the product (see section 3.1). The fractions containing PtdHisOH are pooled together, and place under a desiccator to remove the eluent. The purified product is then resuspended in chloroform and stored at -20°C.

2.2.3. Mass spectrometry

The sample is analysed by mass spectrometry. A Single Mass Analysis is performed using a Shimadzu MALDI 8030 equipment. The analysis is performed by a member of the Chemistry Mass Spectrometry facility at Imperial College.

2.3. Catalysis

2.3.1. BNPP assay

The BNPP (Bis(4-nitrophenyl) phosphate) assay enables testing for phosphodiesterase activity. BNPP is a compound comprising two nitrophenol groups linked by a phosphate [123, 124]. Phosphodiesterases, like PLD, can cleave this molecule, releasing p-nitrophenol.
P-nitrophenol undergoes a colour change from clear to yellow under alkaline conditions, resulting in absorbance changes at 405 nm. The reaction mechanism is illustrated in Figure 2.6.

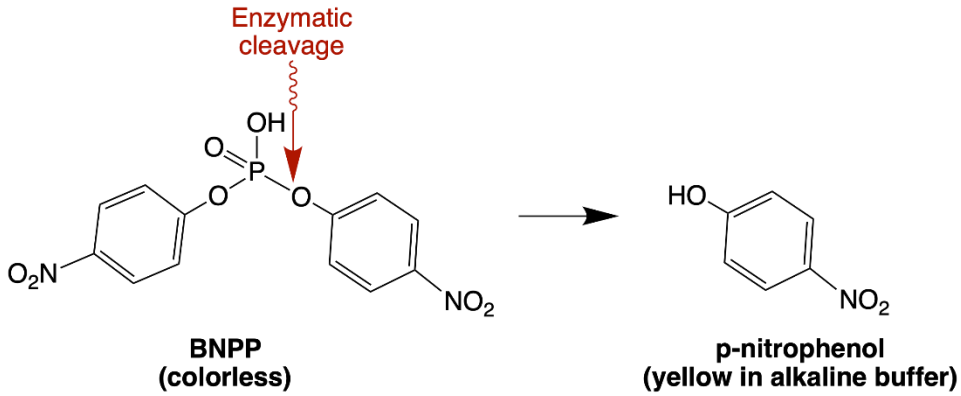


Figure 2.6 – Reaction mechanism for BNPP hydrolysis. Colorimetric compound enabling phosphodiesterase activity detection.

BNPP was purchased from Sigma-Aldrich as a powder, and 2 mM stock solutions were prepared in HPLC-grade water and stored at 4°C.

For a standard assay, 20 µL of PtdHisOH LUVs (or PC, PE LUVs for control) are incubated without or with 20 nmols Zn^{2+} in HEPES buffer pH 7.4, to a final volume of 50 µL. The incubation is carried out at room temperature, on a shaking incubator for 30 minutes, in a clear 96-well plate. The wells are topped with a 50 µL solution of 2 mM pNPP or BNPP respectively, and samples are incubated for 30 additional minutes, at 37°C in a shaking incubator. 10 µL of 750 mM NaOH is added to each well to stop the reaction as well as increasing the phenolate proportion in the mixture to increase absorbance sensitivity. The plate is shaken again for 5 minutes, and subsequently, the absorbance is measured using a SpectraMax M3 spectrometer, along with the SoftMax Pro software.

2.3.2. pNPP assay

The pNPP (p-Nitrophenyl Phosphate) assay enables testing for phosphatase activity. pNPP contains one nitrophenol groups linked a phosphate [125, 126]. In the presence of phosphatases, the phosphate group will be cleaved, releasing p-nitrophenol (yellow in alkaline conditions). The reaction mechanism is illustrated in Figure 2.7. The catalysis experiment is carried out in the same way as with BNPP, but with 2 mM pNPP instead. pNPP was purchased from Sigma-Aldrich as a powder, and 2 mM stock solutions were prepared in HPLC-grade water and stored at 4°C.

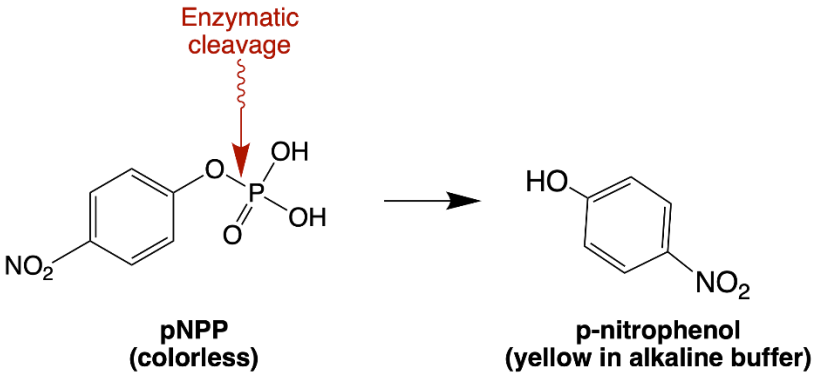


Figure 2.7 - Reaction mechanism for pNPP hydrolysis. Colorimetric compound enabling phosphatase activity detection.

2.3.3. FDA

Fluorescein diacetate (FDA – Sigma Aldrich) is a compound used in the detection of esterase activity. It is a non-fluorescent compound that release a fluorescent fluorescein molecule when hydrolysed [127] (Figure 2.8).

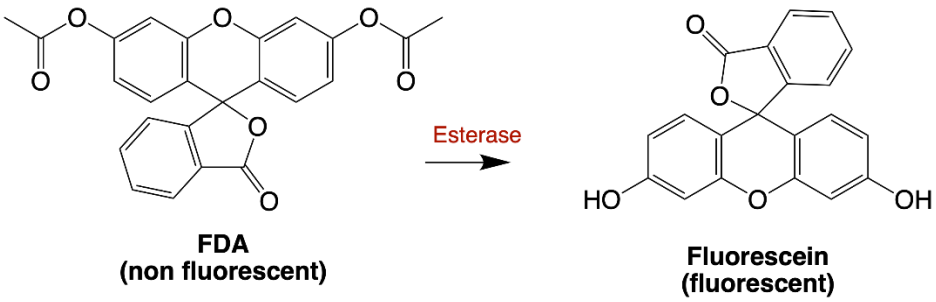


Figure 2.8 - Reaction mechanism for FDA hydrolysis.

For a standard assay, 20 µL of LUVs are incubated without or with 20 nmols Zn^{2+} in HEPES buffer pH 7.4, to a final volume of 50 µL. The incubation is carried out at room temperature, on a shaking incubator for 30 minutes, in a white 96-well plate. After the incubation of LUVs with Zn^{2+}, samples are topped with 49 µL of HEPES buffer and 1 µl of 1 mM FDA. The reaction is monitored with the spectrometer at $Ex_{480\ nm}$ and $Em_{520\ nm}$ for 1 hour. Average catalytic rates were determined using the corresponding calibration curves. For each reaction, the slope was calculated from a 500 second time frame. The significance of errors was calculated with a standard t-test, with $p>0.1234$ (ns), $p>0.0332$ (*), $p>0.0021$ (**), $p>0.0002$ (***), $p<0.0001$ (****).

2.4. Vesicles and micelles

2.4.1. Lipid films

To make vesicles or micelles, the first step is to prepare lipid films. For LUVs or GUVs, 5 mg lipid films are made. For micelles, 1 mg lipid films are made.

The appropriate lipids in chloroform needed for an experiment are mixed in a 7 mL glass vial and vortexed for 30 seconds to ensure appropriate mixing in the case of a lipid mixture. A nitrogen stream, N2 (g) is used to evaporate the chloroform. The lipid film forms at the bottom of the vial's wall. The vial is then placed under a vacuum in a desiccator, for a minimum of 4 hours and up to 48 hours. Once dried, the lipid film will be immediately employed for LUVs or GUVs generation.

2.4.2. Preparation of LUVs by extrusion (large unilamellar vesicles)

For LUVs, the dried lipid film is rehydrated in 1 mL HEPES buffer (pH 7.4) to a concentration of 5 mg/mL, and vortexed for 5 minutes to ensure thorough resuspension of the lipid. At this stage, multilamellar vesicles are formed and need to be extruded to obtain unilamellar vesicles. A mini extruder (Avanti Polar Lipids) is placed on a heating stage set at 60°C, and the vesicles are extruded 21 times through a 200 nm pore-size polycarbonate filter (Avanti Polar Lipids) [128, 129]. The newly formed LUVs are collected in an Eppendorf tube and stored at 4°C for a maximum of 2 days. The quality of SUVs is verified using the particle sizer (DLS) – section 2.5.

2.4.3. Preparation of GUVs by emulsion phase transfer

The emulsion phase transfer or inverted emulsion method was chosen to produce Giant Unilamellar Vesicles (GUVs), as it is a suitable technique for encapsulating smaller vesicles and is compatible with charged lipids such as PtdHisOH [130, 131].

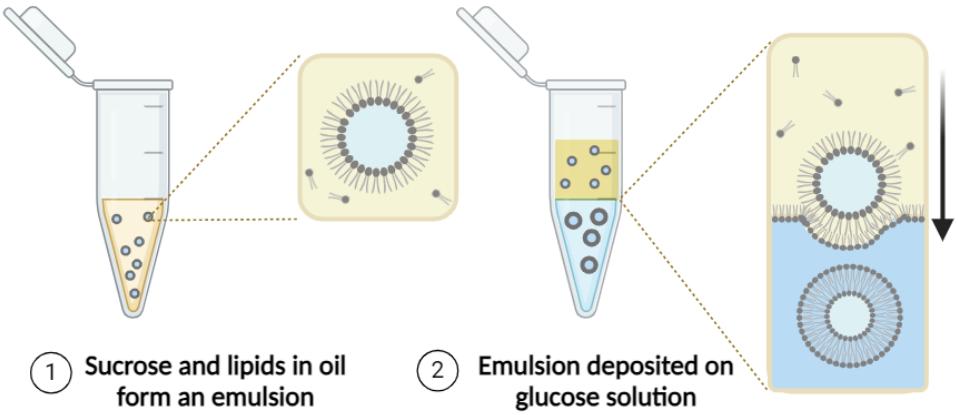


Figure 2.9 – Phase transfer is used to generate GUVs. In step (1) an emulsion is made with the lipid mixture in oil and a sucrose solution. In step (2) the emulsion is deposited on a glucose solution and the sample is centrifuged to form a lipid bilayer.

For this technique, dried lipid films are dissolved in mineral oil (Sigma-Aldrich) to a concentration of 5 mg/mL and vortexed for 5 minutes. To disrupt the multilamellar vesicles, the lipids are sonicated in an ultrasonic bath for 45 minutes at 37 kHz and 40°C. As illustrated in Figure 2.7, in a 1.5 mL Eppendorf tube, 200 µL of phospholipid in oil is layered on top of a 20 µL sucrose solution (0.5 M). A water-in-oil emulsion is created by pipetting up and down 10 times. In a second 1.5 mL Eppendorf tube, the emulsion is then layered on top of a 300 µL glucose solution (0.5 M).

The tube is incubated at room temperature for 10 minutes without shaking to allow the lipids to reach the interface between the aqueous and oil phases. The samples are then centrifuged for 40 minutes at 10,000 g.

During centrifugation, the sucrose-filled water-in-oil droplets sink through the oil layer into the glucose solution, forming a lipid bilayer. The density difference between sucrose and glucose promotes the sinking of the vesicles, which ultimately form a small pellet at the bottom of the Eppendorf tube (Figure 2.9).

After centrifugation, the mineral oil and glucose solution are removed, and the pellet is resuspended in 300 µL of fresh 0.5 M glucose for a washing step. Vesicles are pelleted at 9,000 g for 10 minutes and finally resuspended in 200 µL of fresh glucose solution. The samples are stored at 4°C for a maximum of two days.

2.4.4. Preparation of detergent mixed micelles

Lipid-detergent micelles are prepared fresh, from a 1 mg lipid film (see section 2.4.1). The lipid film is resuspended in HEPES buffer pH 7.4 and 10 mM OG (beta-D-Octyl glucoside) to a concentration of 5 mg/mL. Lipids in solution are vortexed for 2 minutes before being sonicated for 10 minutes in a sonicator bath (Elmasonic P, Arcane Industries).

2.5. Particle sizer

To measure the size of LUVs, dynamic light scattering (DLS) was used [132, 133]. In a semi-micro polystyrene cuvette (BRAND), 20 µL of LUVs in buffer are mixed with 400 µL of HEPES pH 7.4 buffer, and metals as indicated in the corresponding figure legends.
The size distribution of the sample is measured with the Zetasizer Nano particle characterisation system (Malvern Panalytical) and the data is visualised on the ZS explorer software, with the following settings: the cuvette is set to micro-cuvette; the material to liposome; and the equilibration time to 2 minutes.

2.6. Fluorescence wide-field microscopy and confocal microscopy

GUVs are big enough to be analysed by fluorescence microscopy imaging. FITC and DAPI filters are used for mEGFP and Fura-2 fluorophores, respectively, ensuring specific wavelength detection. The Nikon Eclipse TE 2000-E Inverted Microscope connected to a Ximea MQ013MG-E2 camera is employed.

Confocal microscopy allows one to image different focal planes, providing a high spatial resolution and contrast [134]. A Leica TCS SP5 confocal microscope is employed for this purpose. Fluorescent images are acquired using an Argon laser (488nm), and subsequent image analysis and editing are performed using ImageJ software. Figure 2.10. shows the main components of fluorescence wide-field and confocal microscopy.

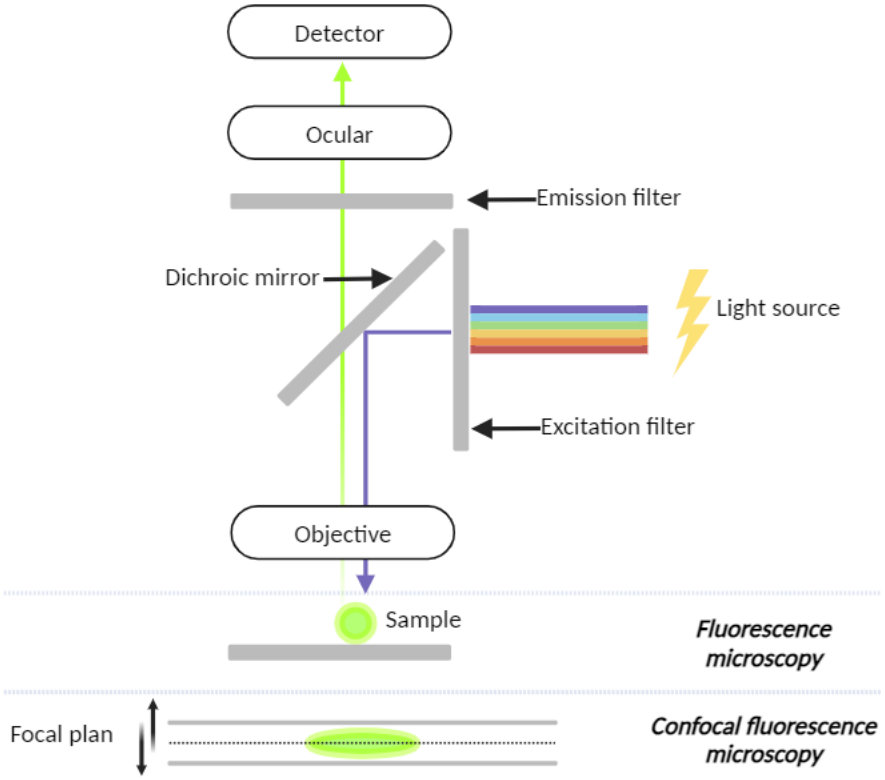


Figure 2.10 – Schematic depiction of fluorescence wide-field and confocal microscopy.

2.7. His-mEGFP

2.7.1. Protein expression and purification

For this research project, we expressed and purified His-mEGFP using plasmid #29663 (Addgene – Scott Gardia Lab). The protein expression was carried out in *E. coli* BL21(DE3) cells, utilizing a plasmid containing a kanamycin resistance cassette (Figure 2.11).

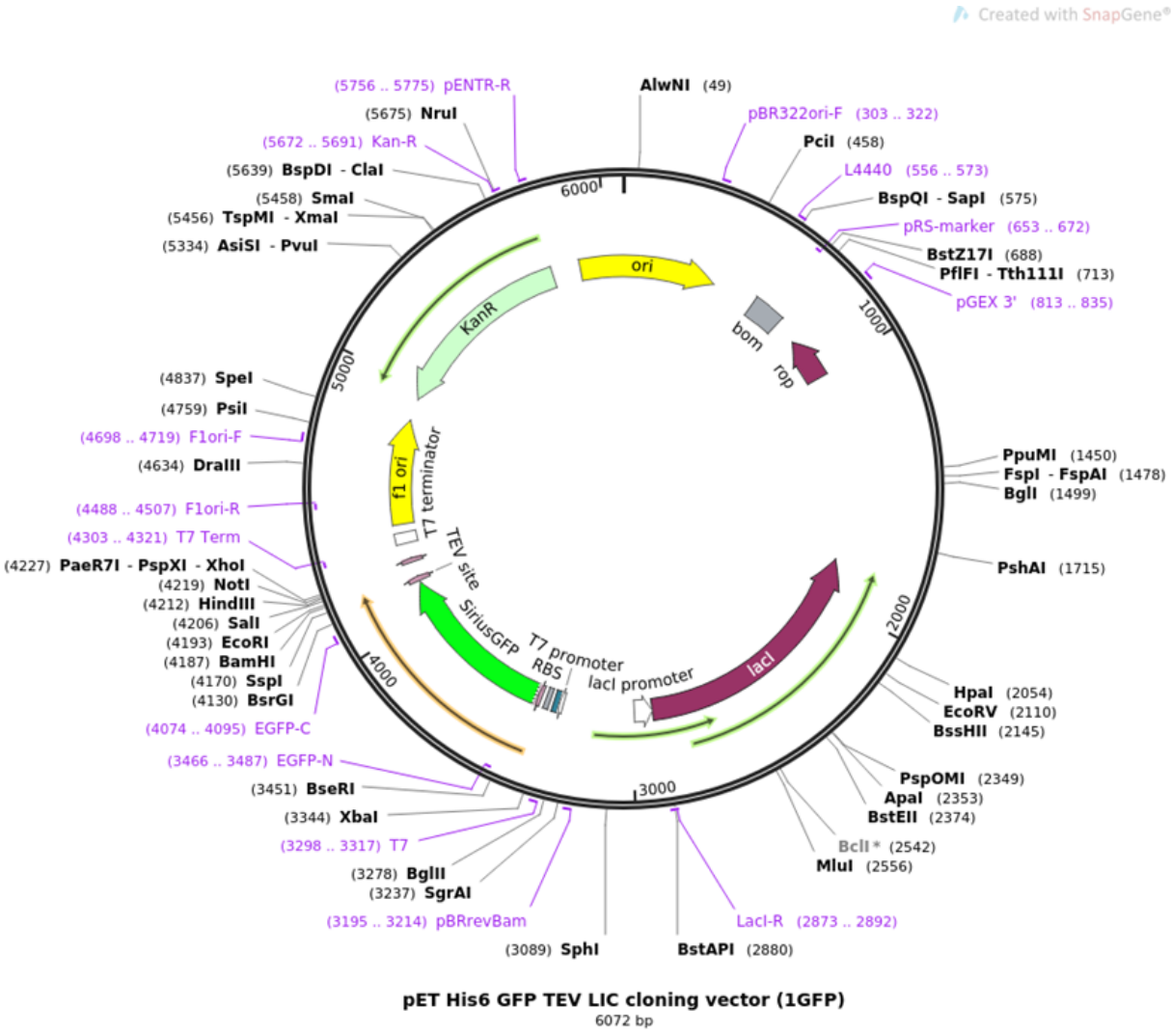


Figure 2.11 – Schematic representation of the plasmid vector employed for his-mEGFP expression. The plasmid contains a kanamycin resistance gene and the expression of his-mEGFP is controlled by an inducible T7 promoter. The plasmid was transformed into E. coli BL21(DE3) for protein expression and purification.

The protein expression and purification was adapted from a method described earlier [135]. To initiate protein expression, overnight liquid cultures are prepared from glycerol stocks in LB medium supplemented with 50 µg/mL of kanamycin. These cultures are then incubated overnight at 30°C in an orbital shaker set to 220 rpm under aerobic conditions. The following day, a 3 L glass conical flask is filled with 1 L of LB supplemented with 50 µg/mL of kanamycin, and inoculated with the overnight culture to an optical density at 600 nm ($O.D._{600}$) of 0.03 to 0.06 a.u. Subsequently, the flask is incubated at 37°C and 180 rpm until mid-log phase is reached (approximately $O.D._{600}$ = 0.3 – 0.5 a.u.). At this point, the culture is induced by adding 1 mM IPTG (Isopropyl β-D-1-thiogalactopyranoside) to

the flask. His-mEGFP expression is monitored every hour, and the maximum expression is detected after 6 hours.

Upon completion of expression, the cells are harvested by transferring the culture into centrifuge tubes and centrifuging at 5,500 g for 15 minutes at 4°C. Subsequently, the supernatant is discarded, and the cells are resuspended in 20 mL of buffer A (composed of 150 mM NaCl, 100 mM HEPES-NaOH, pH 7.5).

To lyse the cells, a tip sonicator is utilized, employing a 22-minute cycle (3 seconds ON; 9 seconds OFF). Following lysis, cell debris is separated from the protein by ultra-centrifugation at 35,000 g for 1 hour at 4°C. The resulting supernatant, containing the protein of interest, is collected, and set aside for purification. Figure 2.12. shows the aspect of the cells at each step.

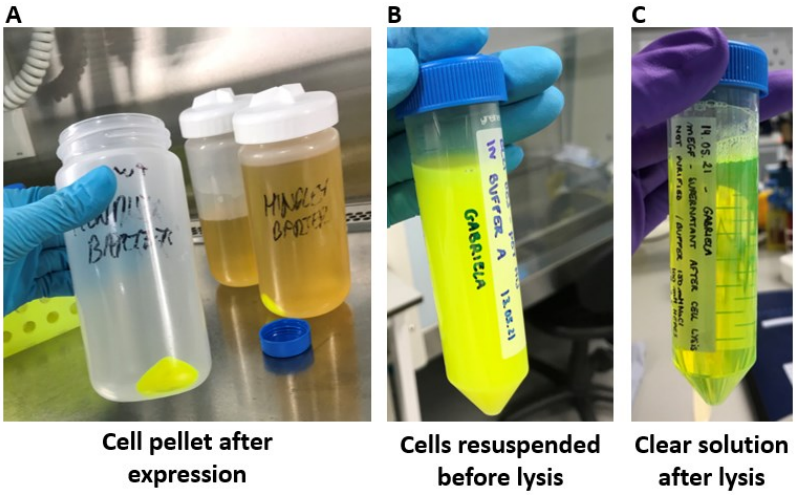


Figure 2.12 – (A) Cell pellet after expression of his-mEGFP and centrifugation. (B) Cell resuspended in buffer A before lysis. The solution is very opaque. (C) Cell resuspended in buffer A after lysis; the solution is not cloudy anymore, indicating a good lysis of the cells.

For the purification, a HisPur™ Cobalt resin (ThermoFisher), boasting a binding capacity exceeding 10 mg/mL, is employed. A 5 mL column is prepared using buffer A, and all purification steps are executed in a cold room maintained at 4°C for optimal protein stability.

Following column preparation, the column is washed thrice with buffer A to equilibrate it. Subsequently, 20 mL of the protein sample is applied to the column, and the flow-through is collected in a Falcon tube. The column is then washed with 20 mL of Buffer A

supplemented with 10 mM imidazole to minimize nonspecific binding, with the flow-through also collected in a Falcon tube.

A step-elution is performed by gravity, with 6 mL of buffer B (composed of 200 mM imidazole, 150 mM NaCl, 100 mM HEPES-NaOH, pH 7.5). The purified protein is collected in a Falcon tube. Figure 2.13. shows the different fractions collected during the purification steps.

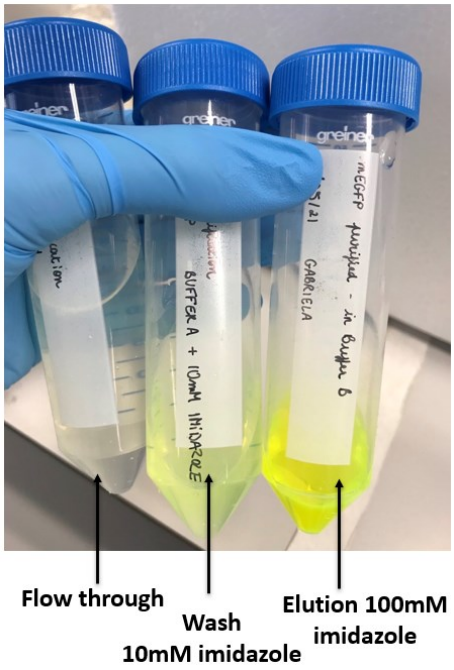


Figure 2.13 – Fractions collected during purification: Flow through, washes and purified protein are shown. The clear colour of the flow through shows a good retention of the his-tagged protein, while the bright yellow colour in the third tube indicated the elution of the purified protein.

The purified protein is concentrated using an Amicon Ultra-4 centrifugal filter device, spinning the tube at 5,000 g for 25 minutes at 4°C. Following concentration, the protein is transferred to a PD-10 desalting column for buffer exchange, to remove buffer B and replace it with 100 mM HEPES buffer at pH 7.5. The spin protocol from the manufacturers recommendations is followed. If necessary, the protein can be concentrated again.

For storage, 20 µL aliquots are prepared in PCR tubes, flash frozen in liquid nitrogen, and stored at -80°C until use.

2.7.2. SDS-page protein gel

To validate the expression and purification of the protein, SDS-PAGE analysis was conducted using NuPAGE™ reagents from Invitrogen, and following manufacturer's instructions.

Samples are first diluted (2-fold and 10-fold dilution) and mixed with NuPAGE™ LDS Sample Buffer (4X) and NuPAGE Sample Reducing Agent (10X). The mixture is then heated to 70°C for 10 minutes to denature the proteins.

Subsequently, the prepared samples are loaded onto a 12% NuPAGE™ Bis-Tris gel and electrophoresed at 200V for 40 minutes. SeeBlue™ Pre-stained Protein Standard is used for the molecular weight marker.

After the electrophoresis run, gels are stained with Bio-Safe™ Coomassie G-250 stain (Bio-Rad) for 1 hour and then destained overnight in water. Imaging is performed using a transilluminator.

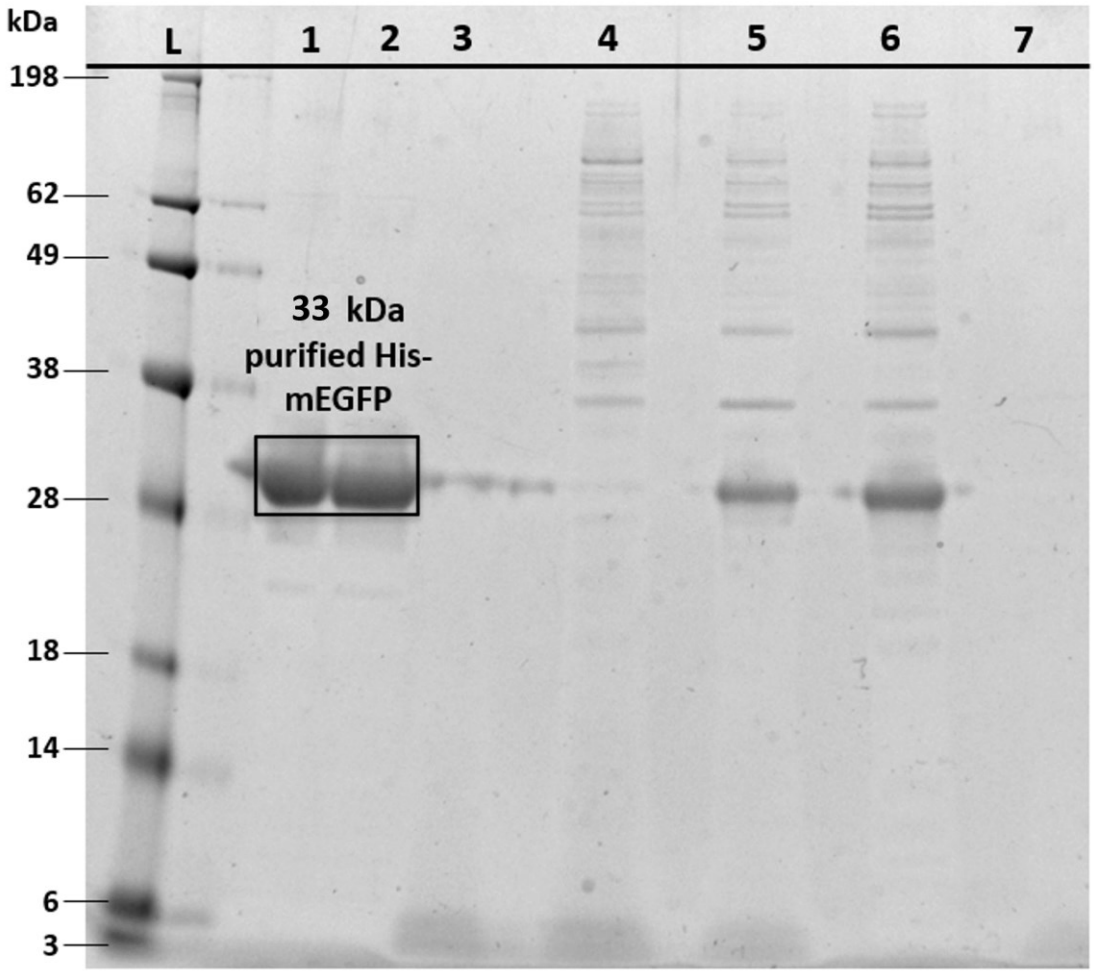


Figure 2.14 – SDS-page for his-mEGFP. L: Ladder; 1 & 2: Purified His-mEGFP, 3: LB, 4: E. coli culture uninduced, 5: E. coli culture induced +6hours, 6: Unpurified His-mEGFP, 7: Supernatant of cell pellet after protein production.

Figure 2.14 shows the outcome of the His-mEGFP protein expression and purification process. Lines 1 and 2 containing the purified protein, show its presence after purification. Lines 5 and 6, containing the induced *E. coli* culture cell extract, exhibit bands corresponding to his-mEGFP as well as bands for many other proteins present in cells. In contrast, line 4, representing the uninduced culture cell extract displays bands corresponding to various proteins, but minimal amount of His-mEGFP is detectable. These results show successful expression and purification of the protein of interest.

2.7.3. Quantification

To quantify the amount of protein expressed and purified, the Bradford Assay was employed [136]. Initially, a standard curve spanning from 0 mg/mL to 1.4 mg/mL of BSA is prepared in duplicates. Then, 5 µL of each sample to be analysed are mixed with 240 µL of Bradford reagent (VWR) in a clear 96-well plate.

The plate is then placed in a plate reader, and the samples are shaken for 5 minutes to ensure homogeneity before measuring the absorbance at 595 nm. From the calibration curve, the amount of protein produced can be calculated.

2.8. Flow cytometry for fusion assays

To analyse the fusion behaviour of SUVs containing PtdHisOH lipid in the presence or absence of metals, a nanoflow cytometer was used, allowing multiparameter measurements at the single-particle level. This method uses flow cytometry principles with highly sensitive detectors and specialised fluidic systems to measure the size (scatter) and fluorescence of individual particles from a population.

For the experiment, the Nanoparticle Flow Cytometry (NanoFCM) was used and calibrated with 0.25 µm Fluorescent Silica Microspheres (quality control and fluorescence), and Silica Nanospheres Cocktail #3 (from NanoFCM). The experiments were carried out using standard procedures suggested by the provider.

2.9. Software for figures

All graphs in this thesis are generated using GraphPad Prism 9. Schematic cartoons are made using BioRender. Chemical structures and reactions are made using ChemDraw Professional 23.0. Microscopy images are edited using ImageJ 1.54. SoftMaxPro was used to collect and analyse data from the spectrometer. The software FlowJo was used to analyse nanoflow cytometry data.

3. Chapter 3: PtdHisOH synthesis & chemical characterization

To synthesize the novel lipid PtdHisOH, enzyme-assisted synthesis was selected for its environmentally friendly and cost-effective benefits compared to conventional organic synthesis [137]. Enzymatic synthesis methods typically employ phospholipases due to their high specificity and selectivity [138]. Additionally, enzymatic reactions are conducted under mild conditions and generate phospholipids that are not easily obtained through conventional organic synthesis processes [139]. Specifically, phospholipase D (PLD) was used for this synthesis. The use of PLD in chemical synthesis has been widely characterised in literature and used for the synthesis of natural and unnatural phospholipids [83, 87, 140]. In brief, the enzyme catalyses the exchange of the phospholipid headgroup with the functional group carried by an alcohol, leading to the synthesis of a novel phospholipid [141].

For the synthesis of PtdHisOH, a novel imidazole-containing phospholipid using PLD, L-histidinol was chosen as the substrate. This choice was made because L-histidinol is a natural primary alcohol compatible with the enzyme, it contains the imidazole group required for the intended applications, and it possesses a primary amine that will be utilized for detection (Figure 3.1).

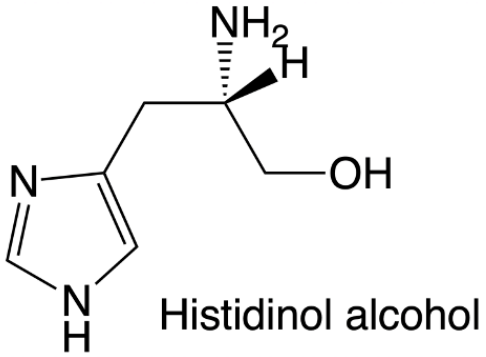


Figure 3.1 – Structure of L-histidinol alcohol. L-histidinol is a derivative of the amino acid histidine, and has a primary alcohol group, a primary amine group and an imidazole ring.

3.1. Optimisation of the transphosphatidylation reaction in the coated system

3.1.1. Introduction of the coated system

The coated system developed in Yang *et al.*, (2022) has been chosen as a high-throughput method to optimise the transphosphatidylation of DOPC into PtdHisOH [112]. As described in more detail in the methods chapter (Section 2.2.3), it consists of immobilising the phospholipids of choice to the bottom of a polystyrene 96-well plate. The lipids stick to the plastic through hydrophobic interactions, making a binding that is resistant to washes.

This technique is very convenient for the nature of the experiments that this project requires, as it allows one to test several conditions at once and it uses little amounts of material (2-times more for the 2-phase system in Eppendorf tubes and 200-times more for the scaled-up synthesis). However, there is a significant decrease in yield observed with the coating system compared to the 2-phase system, estimated to be approximately 10-fold.

3.1.2. Optimal reaction time

To find out the optimal reaction time, a time course experiment was conducted in the coated system. For the development of the assay, the optimum time would be within a linear phase rather than at saturation, to detect the effect of other parameter modifications on the system. This experiment allows to test different incubation times simultaneously.

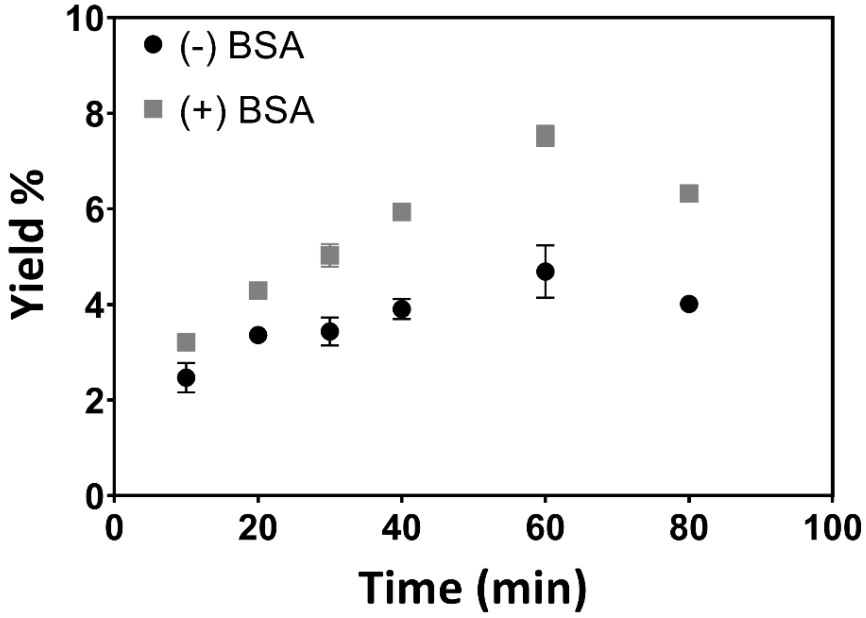


Figure 3.2 – Optimisation of PLD reaction time for the synthesis of PtdHisOH in the coated system. The reaction is a time course for transphosphatidylation reaction in the coated system, carried as described in the methods section, with 100 nmol of DOPC, 200 mM L-histidinol and 0.02 units of PLD. Black rounds correspond to the experiment without BSA; grey squares correspond to the experiment supplemented with 0.05 mg/mL of BSA. The experiment shows an average of n = 6 replicates, with the standard deviation being shown as error.

In Figure 3.2 (-) BSA, we observe a burst in activity in the first minutes, followed by a linear phase from 10 minutes to 60 minutes, where the yield increases with the reaction time. After 60 minutes, the yield stops increasing, indicating that the reaction is completed. For the following experiments and to test other parameters, a reaction time of 20 minutes is optimal, as it is in the linear region.

3.1.3. Reducing unspecific interactions of PLD enzyme

It has been depicted in literature that proteins can be damaged at the air/water interface [142]. This phenomenon is called surface tension denaturing and can also affect the PLD enzyme in the transphosphatidylation reaction, as we use the enzyme at low concentrations. To avoid this denaturation process, Bovine Serum Albumine (BSA) has been used in some other wokr, as it unfolds at the surface interface [143], creating a protection for the other proteins.

Therefore, in our experiments, adding BSA at a low concentration in the reaction mix leads to the saturation of the interface in protein, protecting the PLD enzyme from the air/water interface and giving it more stability.
The following experiment is done to determine the impact of BSA on our reaction. A transphosphatidylation reaction was performed in the coated system, without or with BSA in the aqueous mix, at the final concentration of 0.05 mg/mL.

In Figure 3.2. (+) BSA, the increase in yield overtime follows a similar trend than (-) BSA, with the delta between the two data sets increasing over time. The maximum delta is observed after 60 minutes of reaction, reaching a yield of almost 8%.
The increase in yield in the reactions containing BSA indicates that the PLD, as many other proteins, is affected by the surface tension present at the water/air interface. BSA will therefore be used for the synthesis of PtdHisOH.

3.1.4. Optimal substrate concentration: L-histidinol gradient (Km/Vmax)

As L-histidinol is a new substrate for PLD, it is important to find out the kinetic parameters of the enzyme towards the new substrate, and more specifically, the K_M and V_{MAX}. V_{MAX} is the maximum rate of the reaction achieved when all the enzyme sites are saturated with L-histidinol. K_M is the Michaelis-Menten constant, which is the substrate concentration needed for the reaction to reach half of the maximum velocity. As the amount of enzyme is kept constant, these values allow one to better understand the enzymes activity and how the substrate interacts with the active site. This will enable to optimise the amount of L-histidinol required for a reaction, thereby minimizing substrate carry-over in the product, particularly in the 2-phase system.

The following reaction is a dose-response curve for PLD transphosphatidylation in the presence of increasing concentrations of substrate L-histidinol (figure 3.3). The reaction is done using standard conditions, except for the increasing concentrations of L-histidinol. The K_M and V_{MAX} values are determined using GraphPad Prism.

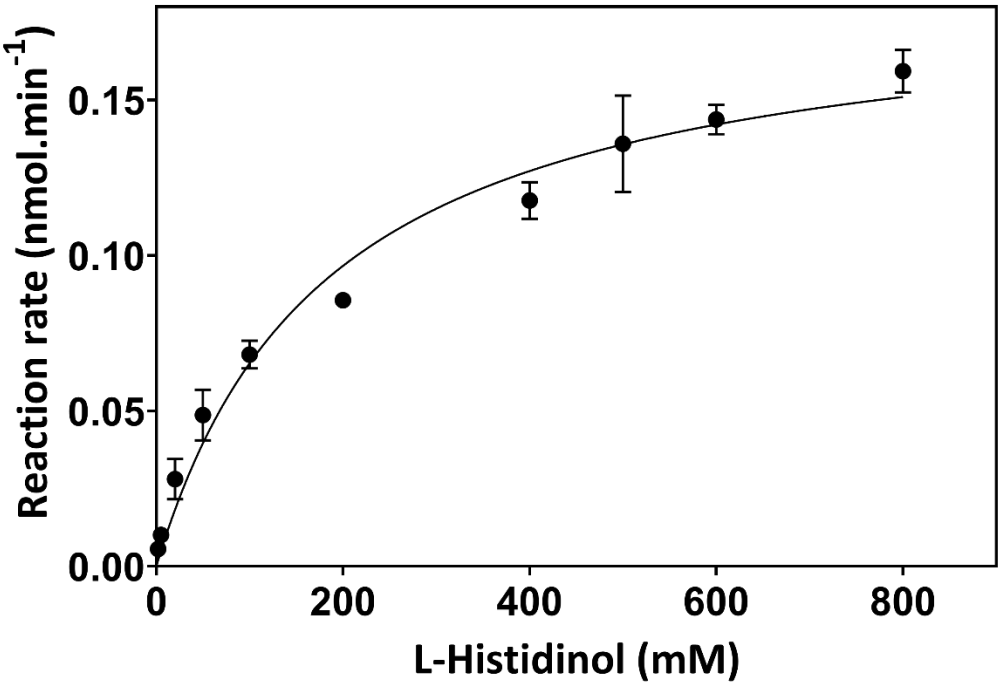


Figure 3.3 – Kinetic properties of PLD towards L-histidinol in the coated system. The reaction contains 0.02 units of PLD, 0.05 mg/mL BSA, and L-histidinol at the indicated concentration, in sodium acetate buffer pH 5.6. The reaction is carried out for 30 minutes at 37°C in a shaking incubator set at 330 rpm. The experiment shows an average of n = 6 replicates, with the standard deviation being shown as error.

Figure 3.3. shows a dose-response curve using DOPC as a starting material and L-histidinol as a substrate. We observe a linear phase from 0 to 100 mM L-histidinol, and the beginning of the saturation at 200 mM L-histidinol. After 200 mM of substrate, the yield keeps increasing at a slower rate until 400-500 mM. From 500 mM, the yield increases at a much lower rate, eventually reaching saturation. The best fit values were determined using GraphPad, where V_{MAX} = 0.18 nmol.min^{-1} (± 0.01) and K_M = 184.5 mM (± 35). The yields obtained are in line with other studies done in the same conditions, with ethanolamine as a substrate [112].

For the following optimisation experiments, 400 mM L-histidinol will be used, as it is the highest concentration of substrate that can be used before the reaction saturates. This concentration will allow one to obtain the maximum yield with the minimum carry over of L-histidinol in the synthesis experiments.

3.1.5. Optimal PLD units for the reaction

To further optimize the reaction, different PLD units were tested with the previously determined concentration of substrate. It has been demonstrated that lower amounts of PLD can be used in the coating system compared to the 2-phase system [112]. Additionally, since this is a novel substrate, the optimal PLD concentration may differ from that reported for other substrates in the literature.

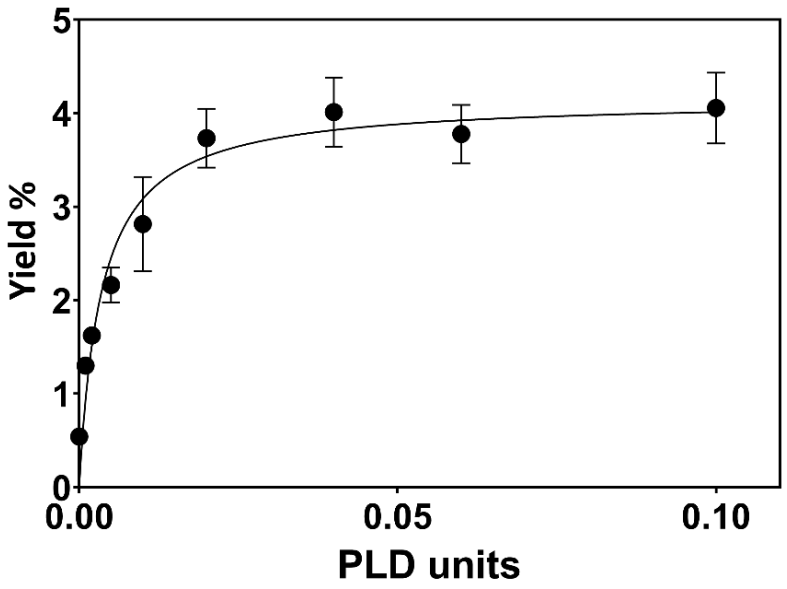


Figure 3.4 – Optimisation of PLD units for the synthesis of PtdHisOH in the coated system. The reaction is carried out as described in the methods section, with 400 mM L-histidinol, BSA 0.05 mg/mL and increasing amounts of PLD (0-0.001-0.002-0.005-0.01-0.02-0.04-0.06-0.1 units) in sodium acetate pH 5.6. The experiment shows an average of n = 6 replicates, with the standard deviation being shown as error.

In Figure 3.4, we observe a linear increase in yield from 0 to 0.01 units of PLD per reaction. 0.02 units of PLD per reaction is the amount of enzyme giving the highest yield (3.7%) before the reactions reaches a plateau and saturates. This is the first value in the saturation zone, and adding more PLD will only make the reaction more costly. Therefore, 0.02 units of PLD was used in the next experiments. This is half of the amount used in other studies for the synthesis of simple phospholipids such as DOPE [144], and five times less than for synthesis of diethanolamine [145].

3.1.6. Temperature

Despite optimising the enzyme and substrate concentration, the maximum yield obtained for this reaction at 37°C is low compared to what has been achieved with DOPE, with the yield approximately halved [112]. Many studies using PLD have demonstrated that the enzyme's optimal temperature for activity is 60°C [84, 146, 147].

In the 2-phase system used for the synthesis, the maximum temperature will be maintained at 37°C. This choice is made because 50°C would approach the boiling point of chloroform (61°C). However, to enhance the yield of the transphosphatidylation reaction in the coated system, the synthesis was conducted at three distinct temperatures: room temperature (±22°C), 37°C, and 50°C. The experiments were done in parallel, using 3 different shaking incubators, and controls with no PLD were also done to monitor the changes in the baseline related to the temperature increase.

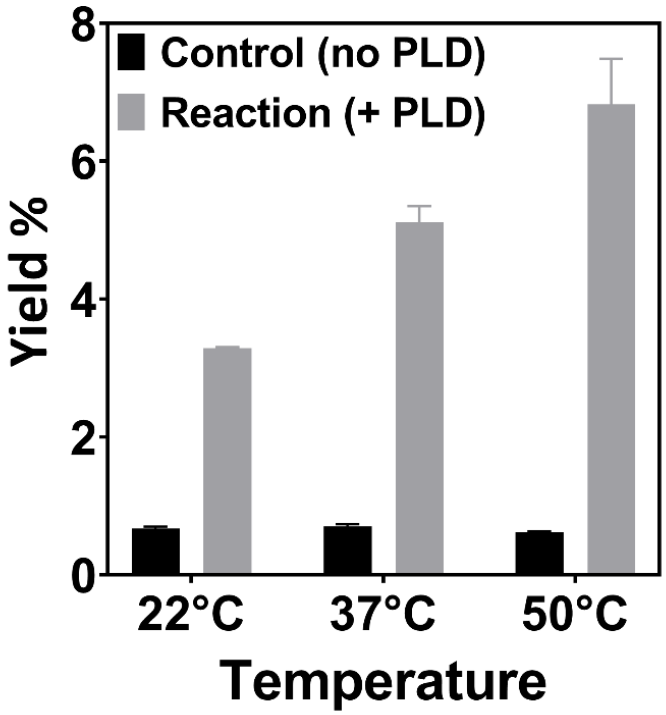


Figure 3.5 – Temperature optimisation for the synthesis of PtdHisOH in the coated system. The reaction is carried out as described in the methods section, with 0.02 units PLD, BSA 0.05 mg/mL, L-histidinol 400 mM in sodium acetate pH 5.6. The plate is incubated for 20 minutes on shaking incubator set at 330 rpm set at room temperature (22°C), 37°C or 50°C. The experiment shows an average of n = 6 replicates, with the standard deviation being shown as error.

Figure 3.5 shows that the control is constant at all temperatures and sets the baseline at 0.6%. For the reaction, the yield increases with the increase of the temperature: we observe a yield increase of 1.6-fold from 22°C to 37°C, and a similar jump from 37°C to 50°C (1.3-fold). These results tie well with previous studies showing the boost in the PLD activity at higher temperatures.

In this first section, we have established and optimised the novel synthesis of PtdHisOH by transphosphatidylation of DOPC using PLD *Streptomyces* sp., in the presence of L-histidinol in the coated system. These conditions will serve as a starting point for scaling up the reaction, even though some parameters will need to be adjusted.

3.2. Optimisation of the reaction is the 2-phase system

The two-phase system, also called biphasic system, is a system composed of an aqueous phase and an organic solvent phase. This system has been widely used in the studies of PLDs derived from *Streptomyces sp.* due to the strong tolerance of the enzyme to solvents. The most commonly used solvents are dichloromethane [114], chloroform [115], diethyl ether or ethyl acetate [148], ranked from best to worst. The biphasic technique is also very convenient for the synthesis of a lipid to be used for further applications, as the aqueous phase is easily separated from the organic phase containing the product of interest.

The following set of experiments are done with the objective to validate the best parameters for the biphasic system based on the optimised parameters in the coating system. The time, the substrate concentration, the temperature, and the amount of enzyme are verified.

3.2.1. Optimal reaction time

As previously done in the coated system, the first step is to validate the optimal reaction time in this new system. As described more in detail in the methods chapter (section 2.2.4.), 100 µL of organic phase composed of DOPC in chloroform is mixed with the equivalent volume of aqueous phase, containing L-histidinol, PLD and BSA in sodium

acetate buffer pH 5.6. The reaction is carried out in a 2 mL Eppendorf tube. The tubes are placed horizontally in a shaking incubator for the corresponding amount of time. The detection is done using fluorescamine, as for the coated system (see methods - section 2.2.3.).

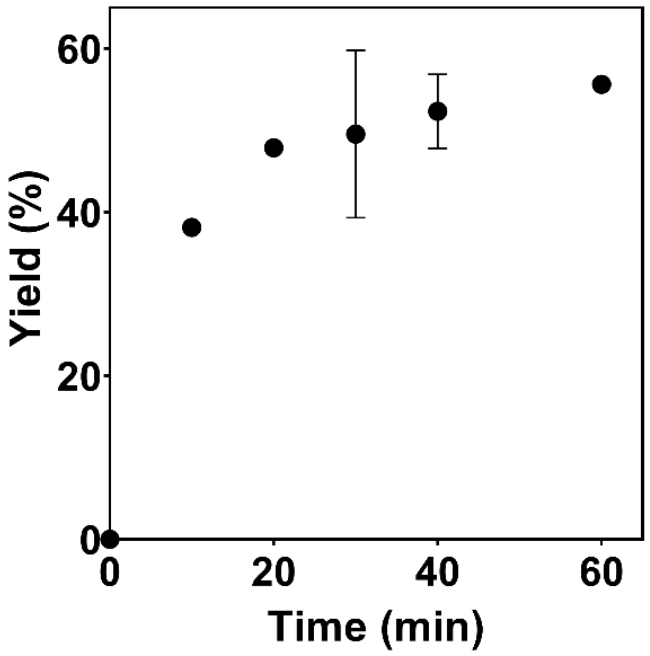


Figure 3.6 – Optimisation of the PLD reaction time in the biphasic system. The reaction is carried out as described in the methods section, with 0.02 units PLD, BSA 0.05 mg/mL, L-histidinol 400 mM in sodium acetate pH 5.6. The tubes are incubated for the time indicated on the figure, on a shaking incubator set at 330 rpm and at 37°C. The experiment shows an average of n = 4 replicates, with the standard deviation being shown as error.

As shown in Figure 3.6, a quick increase in the yield from 0 minutes to 20 minutes incubation time, with a yield reaching up to 50%. After 20 minutes, the yield increase slows down considerably, and a slow drift is recorded. It may reach saturation after 60 minutes. These results are in accordance with the optimisation of the time in the coated system (section 3.1.2).

3.2.2. Optimal substrate concentration

As previously performed in the coated system, a dose-response curve is also conducted in this system to determine the new kinetic parameters of PLD under these conditions.

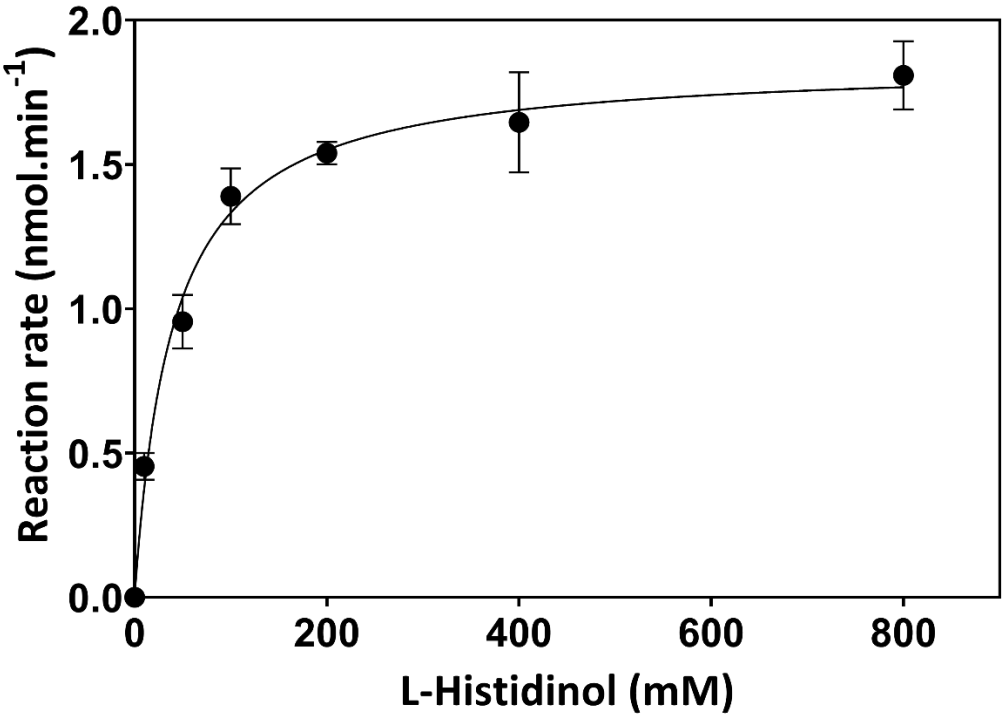


Figure 3.7 - Kinetic properties of PLD towards L-histidinol in the biphasic system. The reaction was carried out using standard conditions, with an increasing concentration of L-histidinol as indicated on the figure. The tubes are incubated for 20 minutes at 37°C, 330 rpm and for 20 minutes. The experiment shows an average of n = 4 replicates, with the standard deviation being shown as error.

As expected from the previous system, the reaction still follows the Michaelis-Menten equation. The yield increases in a linear way from 0 to 100 mM and starts slowing down at 200 mM, reaching approximately 50%. After 200 mM, the curve flattens, indicating that the reaction saturates. For this reaction, the kinetic parameters are K_M = 55.63 mM and V_{MAX}= 1.8 nmol.min^{-1}.

3.2.3. PLD units

From previous experiments (section 3.1.5.), the optimal amount of PLD in the coating system is 0.02 units per well containing 50 µL in total. In the bi-phasic system, the volume

of the aqueous phase is doubled so the amount of enzyme used will most probably need to be adjusted. The following graph shows the PLD dose-response curve.

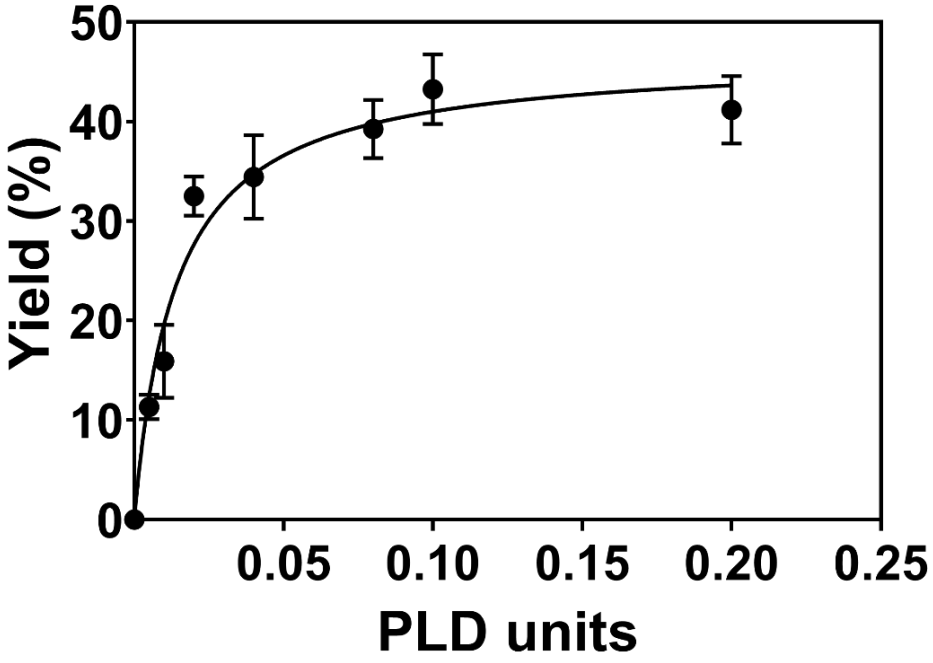


Figure 3.8 – PLD dose response curve in the bi-phasic system. The reaction was carried out using standard conditions, with an increasing amount of PLD as indicated on the figure. The tubes are incubated for 20 minutes at 37°C, 330 rpm and for 20 minutes. The experiment shows an average of n = 4 replicates, with the standard deviation being shown as error.

Similarly to what has been described in the coating system, we observe a linear increase in yield from 0 to 0.02 units per reaction, with the reaction starting to saturate after 0.02 units of PLD. With 0.02 units of PLD, the yield reaches 35%, and up to 40% with higher amounts of PLD.

To produce the new PtdHisOH and in order the stay the most economic as possible, 0.02 units PLD will be used for a 200 µL reaction.

3.2.4. Temperature

As discussed previously and based on literature, PLD activity is stronger at higher temperatures. In the following experiment, the reaction is carried out in the biphasic system at room temperature (± 22°C), 37°C and 50°C, as done previously in the coated

system. As the temperature gets close to chloroform's boiling point, some evaporation is expected. The volume loss will be accounted for in the calculation of the yields.

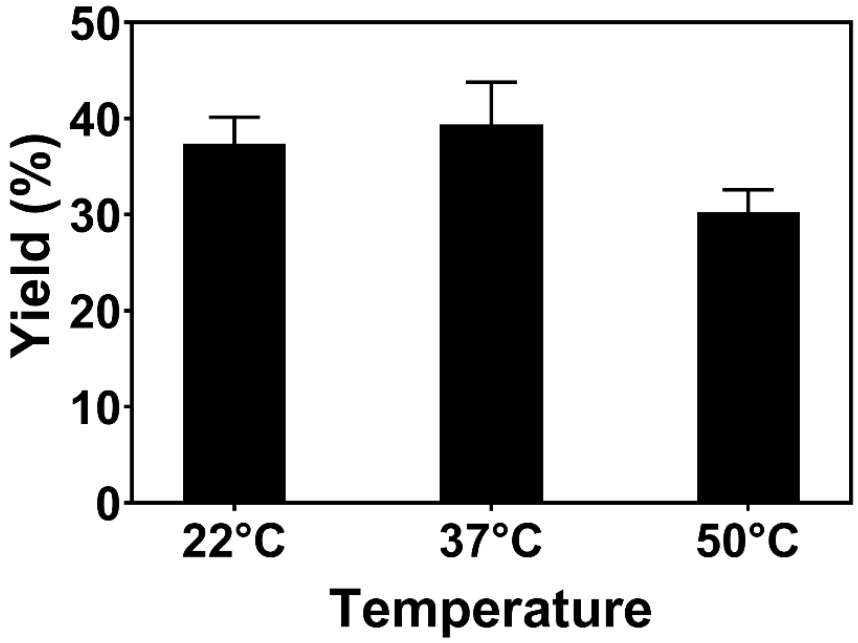


Figure 3.9 – Transphosphatidylation of DOPC to PtdHisOH in the biphasic system with a temperature gradient. The experiment is carried out using standard conditions, with Eppendorf tubes being incubated at the indicated temperatures. The experiment shows an average of n = 4 replicates, with the standard deviation being shown as error. Note: a loss of chloroform was noticed due to evaporation and all yields were corrected according to the final volumes of chloroform measured.

Figure 3.9 shows the yields obtained after the incubation of the reaction at different temperatures. There is no significant increase between the yields obtained after incubation at 22°C and 37°C, that stay between 35% and 40%. At 50°C, the yield drops by 10%, reaching a maximum of 30%. These results are not in line with our previous findings that showed a boost in the yield at higher temperatures. Here, we observe an opposite effect. This might be due to the increased evaporation of chloroform when heated, leading to a disruption in the 1:1 ratio between the organic phase and the aqueous phase, and thus to a drop in the yield. Another parameter that might play a role in the yields obtained in the use of this system is that the Eppendorf tubes that contain the reactions are laid horizontally in the incubator to maximise the exchange surface between both phases. However, it is important to note that the tubes are not sealed with parafilm, and

that the leakage of organic phase must be considered. To conclude on the temperature, 37°C will be used for the following experiments.

3.2.5. Evaporation of chloroform/leaking chloroform

The following experiment aimed to determine whether placing the tubes horizontally in the shaking incubator increased the risk of leakage. For each reaction, tubes were placed horizontally or vertically in the shaking incubator. The reactions were conducted utilizing the optimal parameters established in the standard methods, with 100 µL of each phase employed.

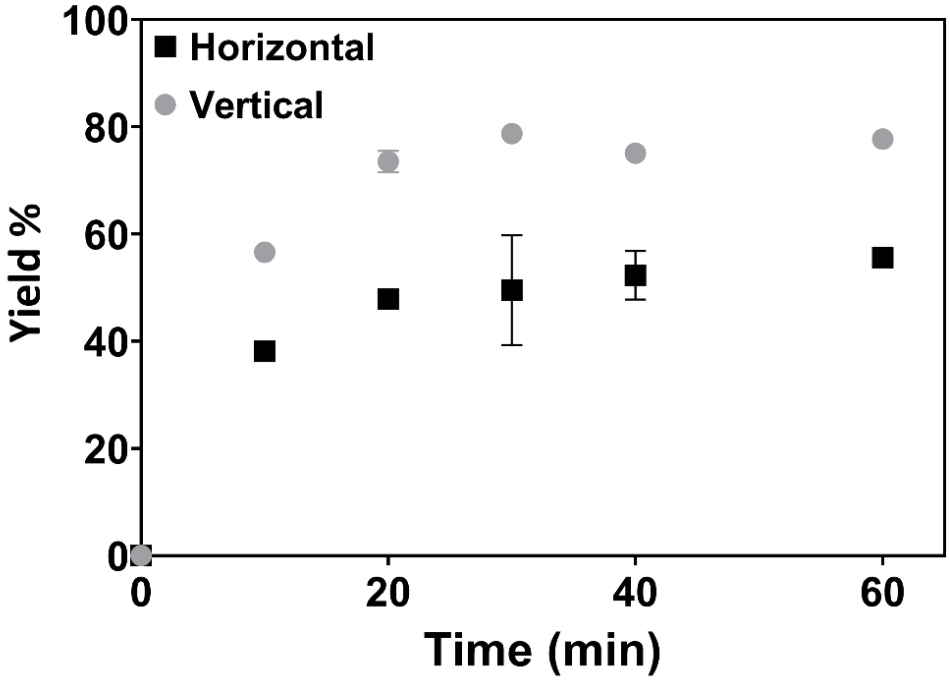


Figure 3.10 – Optimisation of the biphasic system in Eppendorf tubes. The experiment is carried out using standard conditions, with Eppendorf tubes being incubated horizontally or vertically, at 37°C, 330 rpm, and for the indicated amount of time. The experiment shows an average of n = 4 replicates, with the standard deviation being shown as error. The maximum amount of PtdHisOH produced in the bi-phasic system is 130 µg per reaction.

	Vertical	Horizontal
Time (min)	Vol. after reaction (µL)	
0	100	100
10	95	82
20	90	78
30	89	75
40	87	71
60	83	65

Table 3.1 – Volumes measured after transphosphatidylation in the 2-phase system, in tubes placed vertically or horizontally.

Table 3.1 indicates the volumes of the organic phase measured after the reaction. Following 30 minutes of reaction time, a 10% reduction in organic phase volume was observed in the vertical tubes, compared to a 25% reduction in the horizontal tubes. This indicates that, in addition to evaporation, chloroform leakage occurs through the lids of the horizontal tubes. Placing the tubes vertically in the incubator avoids leakage and reduces evaporation of the organic phase.

3.3. Scaled-up reaction in a glass vial

To increase the production of PtdHisOH, we moved from the synthesis in Eppendorf tubes, to the synthesis in round-bottom flasks (5 mL, 10 mL and 50 mL), allowing the use of much bigger volumes for the reaction. The compositions of the aqueous phase and organic phase and the conditions for the reaction used in the glass vials are stated in Table 3.2, together with the yields achieved.

The scale-up is done in a step wise manner, moving from the 200 µL scale (Eppendorf) to 3 mL reaction, then 7 mL reaction and finally 20 mL reaction. This is done to monitor the yield when increasing volumes, making sure that the yield does not drop.

One condition that is different in the round-bottomed flask is the mixing of the 2 phases: in the Eppendorf tubes, the mixing is done in a shaking incubator, limiting the mixing of the two phases. In the round-bottom flask, the shaking is done using a stirrer bar on a magnetic hot plate, allowing a much stronger mixing of the two phases.

Yield %			Conditions				
Average	**Std dev**	**n=**	**Vol. for each phase before reaction**	**Vol. organic phase after reaction**	**Time**	**Temp.**	**Stirring**
47.9	1.044	6	0.1 mL	0.078 mL	20min	37°C	Shaking incubator
85.5	9.697	6	1.5 mL	1.3 mL	20min	37°C	Stirring bar
65.7	4.913	3	3.5 mL	3.1 mL	20min	37°C	Stirring bar
81.7	5.695	6	10 mL	8.3 mL	40min	37°C	Stirring bar

Table 3.2 – Summary table with yields and conditions for each step of the scale up

From 200 µL (line 1) to 3 mL (line 3), the reaction volume is increased 15 times, and the yield is 1.8-fold higher, reaching 85%. This is unexpected, as usually a drop in the yield can be observed when scaling up a reaction to larger volumes. In this case, the increase in yield can be attributed to the change in the stirring method, increasing the exchange surface between the two phases, and therefore, leading to a higher yield.
Increasing the reaction volume from 3 mL to 7 mL (x 2.3 times) showed a drop of 20% in the yield, which is a significant drop, but still acceptable for our purpose. This might be due to the increase of the volumes used, reducing the efficacy of the mixing between the two phases.

The goal of the scaling up process is to reach a total reaction volume of 20 mL in order to produce enough material for several experiments.
The conditions are kept the same, except for the reaction time that is doubled, going from 20 minutes to 40 minutes. The decision to increase the reaction time to 40 minutes was taken after observing the drop in the yield from 3 mL preparations to 7 mL preparations (Table 1). The time course experiments (Figure 7, Figure 11) showed that after 20 minutes, the reaction would saturate and the yield would stay constant, so increasing the reaction time would not lead to a drop in the yield but would give more time for the two phases to come into contact. Increasing the reaction time allowed to reach a similar yield than in the 3 mL reaction, but with much larger volumes. The average yield obtained in the 20 mL reaction fluctuates around 82%, with a 5% error.

3.4. Yields

The yield obtained from a transphosphatidylation reaction using PLD is very variable from one reaction to another, depending on the enzymatic source used, the nature of the substrate and its concentration, the media used for the reaction [84]. It has been shown in different studies that for the same reaction, different sources of PLD lead to very different yields, with up to 40% difference (*Streptomyces* sp., Cabbage, Peanuts…) [66, 149]. Using primary, secondary or tertiary alcohols for the substrate also impacts the yield by 2-fold, with primary alcohols being the best substrates for the reaction [140]. The choice of the organic solvents for the reaction in the biphasic system will also impact the rate of the reaction and the hydrolysis activity. Chloroform gives one of the best rates, and was used for convenience [117]. Finally, the concentration of substrate is also crucial to obtain the best yield with minimum hydrolysis [150]. The synthesis of PtdHisOH in the scaled-up system yielded 81%, which aligns with the highest yields reported in the literature for the synthesis of simple phospholipids, typically around 90% [84].

3.5. Chemical characterisation on TLC

To qualitatively analyse the synthesis of the novel PtdHisOH, Thin Layer Chromatography is used as a first step in characterisation, as it is quick and commonly used in chemistry. As this is a novel lipid, there is no standard for PtdHisOH that can be used to compare the product of the reaction. We also need to find the best eluent system to separate the product PtdHisOH from the other lipids that might be present in the chloroform phase, such as DOPC (starting material) and DOPA (product of the competing reaction).

To find the right eluent and distinguish between the three possible lipids, a set of three staining solutions is tested: Molybdenum blue is used to identify all the phospholipids on the TLC (DOPC, DOPA and PtdHisOH) [119], while Ninhydrin is used to detected primary amines [120], and would stain PtdHisOH as well as L-histidinol. Fluorescamine has been used for the detection of PtdHisOH in the coated system, and therefore can be used in parallel of Ninhydrin, to confirm that the stained lipids are PtdHisOH. Using these set of stains with the standards for DOPC and DOPA will allow to discriminate between the phospholipid stained with Molybdenum blue.

The next step is to find the eluent that will allow one to separate DOPC, DOPA and PtdHisOH, as these three lipids have close molecular weights: 722 g/mol for DOPA, 786 g/mol for DOPC and 824 g/mol or PtdHisOH, but different polarities.

The first eluent tested is commonly used to separate phospholipids [151]. It is composed of Chloroform : Acetone : Methanol : Acetic acid : Water (65 : 20 : 10 : 10 : 3). DOPC, DOPA and L-histidinol are deposited on the plate as standards and the reaction mix to be analysed (PtdHisOH) is deposited last. The plate is then stained with Molybdenum blue or Ninhydrin.

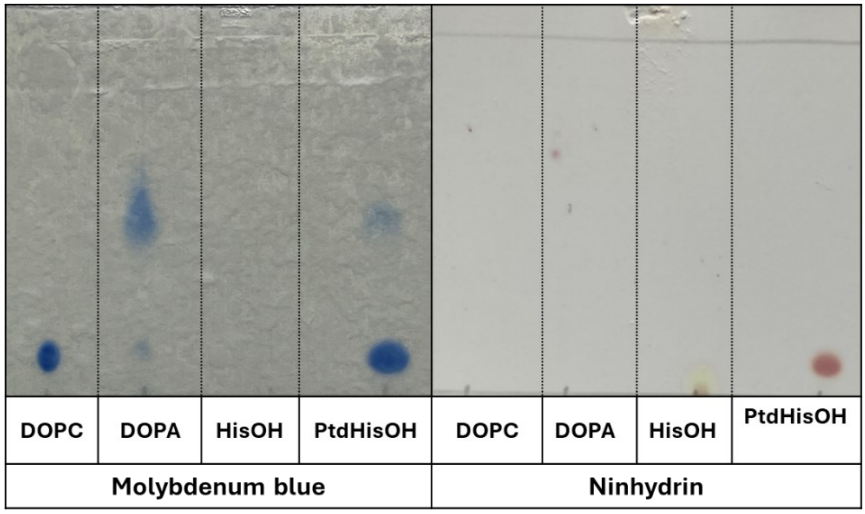


Figure 3.11 – TLC plate stained with Molybdenum blue or Ninhydrin. The mobile phase used in this experiment is Chloroform : Acetone : Methanol : Acetic acid : Water (65 : 20 : 10 : 10 : 3). Roughly, 4 nmol of lipids are deposited. In this system, DOPC and PtdHisOH run at an R_F = 0.08, DOPA at an R_F = 0.5, and HisOH at an R_F = 0.

In Figure 3.11, in the first TLC stained with Molybdenum blue, DOPC and DOPA (1st and 2nd column) run differently, DOPC being much lower than DOPA. The 3rd column containing L-histidinol (free alcohol) is not stained as it is not a phospholipid. In the 4th column containing labelled PtdHisOH containing the reaction mix, two different spots are visible: the top spot migrates with similar R_F values to DOPA standard and the bottom one to the DOPC standard. This staining method does not allow to determine if PtdHisOH is present in the product. Ninhydrin is used as an alternative stain to Molybdenum blue to visualise PtdHisOH. In the 2nd TLC plate stained with Ninhydrin, the first two columns corresponding to DOPC and DOPA are empty as expected, as these compounds do not

contain any amine group. The 3rd row shows a spot for the alcohol L-histidinol, that has not migrated with the mobile phase. The 4th column containing the product shows a clear spot corresponding to the product PtdHisOH. The combination of these two staining methods allows to conclude that:

- PtdHisOH is successfully synthesised.
- There are some traces of DOPA detected in the reaction mix column stained with Molybdenum blue, indicating that part of the DOPC is being hydrolysed instead of being transphosphatidylated.
- No L-histidinol is detected in the reaction mix, indicating that there is no carry over of the alcohol to the reaction mix.
- DOPC and PtdHisOH are not separated in this eluent system, which does not allow determine if there is DOPC remaining in the product.

To separate DOPC and PtdHisOH, a new eluent system is tested. The composition is the same than the first eluent system, without Acetic acid to avoid the acidic pH that would change the charge of PtdHisOH and its movement on the TLC. This eluent system contains Chloroform : Acetone : Methanol : Water (65:20:10:3).

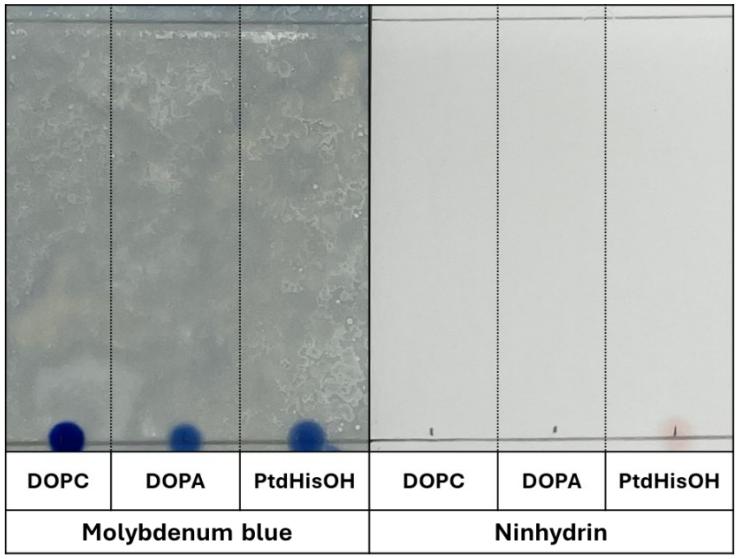


Figure 3.12 - TLC plate stained with Molybdenum blue or Ninhydrin. The mobile phase used in this experiment is Chloroform : Acetone : Methanol : Water (65:20:10:3). Rf values are equal to zero for all 3 lipids. L-histidinol was not included.

In the first TLC plate stained with Molybdenum blue, we can clearly see that none of the 3 lipids (DOPC, DOPA and PtdHisOH) move in this eluent system. The 2nd TLC plate stained with Ninhydrin confirms that PtdHisOH is present but does not migrate. This eluent system is not suitable for separating our phospholipids.

A 3rd eluent system containing ammonium hydroxide is tested, to find a pH where the PtdHisOH is neutral instead of being charged. It has been shown that ammonium hydroxide is useful to separate phospholipid by polarity and charge, and is often used in the presence of amines as it can modify the analytes retention towards the stationary phase [152, 153]. This eluent system is composed of Chloroform : Methanol : Ammonium hydroxide (65 : 25 : 4) [117, 118].

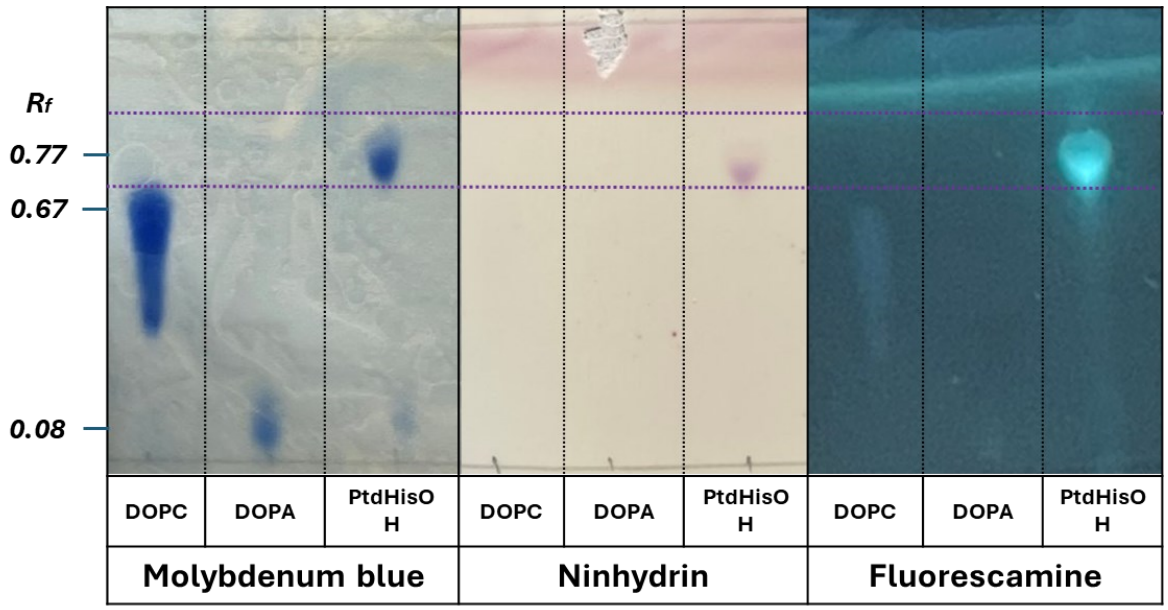


Figure 3.13 - TLC plate stained with Molybdenum blue, Ninhydrin or Fluorescamine. The mobile phase is composed of Chloroform : Methanol : Ammonium hydroxide (65 : 25 : 4). In this system, DOPC runs at an R_F = 0.67, PtdHisOH run at an R_F = 0.77, and DOPA at an R_F = 0.08.

In the 1st plate stained with Molybdenum blue, DOPC runs quite high, at an R_f = 0.67. DOPA moves very slowly in this system and reaches an R_f = 0.08. In the 3rd column corresponding to the reaction mix, there is a first spot very faint that corresponds to the same R_f than DOPA, and a higher spot that does not correspond to any of the standards. In the 2nd plate stained with Ninhydrin, the 3rd column shows a spot at this same R_f (0.77), indicating that the spot corresponds to PtdHisOH. The 3rd plate stained with

fluorescamine and visualised with a UV light confirms that the spot corresponds to PtdHisOH, with an R_f = 0.77.

The combination of these staining methods in this eluent system demonstrates that there is no detectable DOPC remaining in the reaction mix, and that hydrolysis happens at a much lower rate as compared to the transphosphatidylation reaction, leading to a reaction mix containing low amounts of DOPA. This technique can therefore be used to separate and detect the product with the appropriate standards.

3.6. Purification and chemical characterisation through mass spectrometry

Using a silica column as described in the methods chapter [see methods – section 2.3.2] and the TLC eluent system that allows to separate DOPC, DOPA and PtdHisOH (see figure 14), the reaction mixture was purified for mass spectrometry analysis, using the MALDI (matrix-assisted laser desorption/ionization) technique [see methods – section 2.3.3].

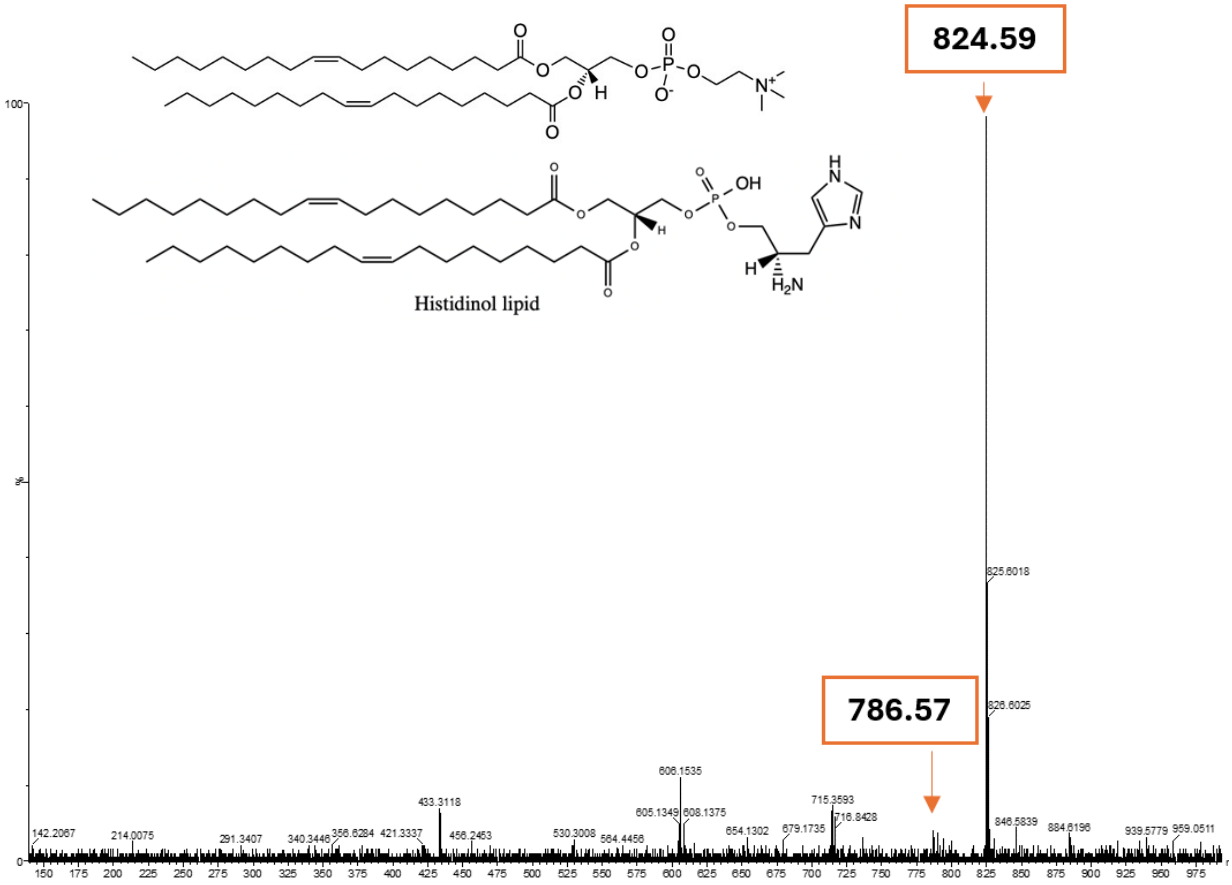


Figure 3.14 – MALDI mass spectrum for purified PtdHisOH.

The graph above shows the result of the mass spectrometry, with a very small peak at 786.57 m/z corresponding to DOPC, and a very high peak at 824.59 m/z, reaching 100% relative abundance, corresponding to PtdHisOH.

This result in combination with the TLC result, validates the successful synthesis of PtdHisOH by PLD transphosphatidylation.

3.7. Conclusions

Chapter 3 details the development and optimisation of the PtdHisOH lipid by enzyme-assisted synthesis. This chapter highlights the optimisation of the lipid synthesis in the coating system initially, aiming for high throughput and minimal use of consumables. Subsequently, we transitioned to the 2-phase system and scaled up the reaction to a maximum volume of 20 mL. Throughout this process, we maintained high yields at approximately 80%, meeting the

requirements for our intended applications of the lipid. Successful purification and chemical characterisation were achieved through plate reader assays using fluorescamine, with TLC and mass spectrometry, validating the novel lipid synthesis.

4. Chapter 4: Characterization of PtdHisOH metal-binding properties

The PtdHisOH lipid has been developed to create a novel lipid capable of binding metal ions, through the histidine present in the lipid, and more precisely through the imidazole group.

Imidazole is an aromatic heterocycle containing two nitrogen atoms, which gives the ability to the compound to bind metal ions [154]. Imidazole can coordinate with a wide range of metal ions including Cu^{2+}, Zn^{2+}, Ni^{2+}, Fe^{2+} and Co^{2+}, with the binding capacity dependent on factors such as solvent, pH, and temperature [155-159].

The coordination chemistry of imidazole has been extensively investigated due to its crucial role in metalloproteins, where imidazole-containing residues such as histidine facilitate metal chelation and catalysis [160]. For instance, numerous studies have highlighted the significant role of Zn^{2+} in catalysis by enzymes containing histidines [161, 162].

Imidazole also exhibits versatility in coordination, capable of acting as a mono-, bi-, or tridentate ligand depending on the coordination requirements of the metal ion and the resulting complex's geometry [163].

Imidazole coordination is widely found in nature, and finds applications in biotechnology, including catalysis and metal extraction, due to its ability to interact with metal ions effectively and selectively [36].

4.1. Lipid functionality – metal binding assay development

To test PtdHisOH metal-binding functionality, a new assay was developed based on the lipid coating technique detailed in the methods chapter (section 2.2.1). Briefly, the lipid is coated on the bottom of a 96-well plate and incubated with a metal ion in solution. The unbound metal is washed away, and the metal bound to the lipid is detected using a suitable detection method as outlined below.

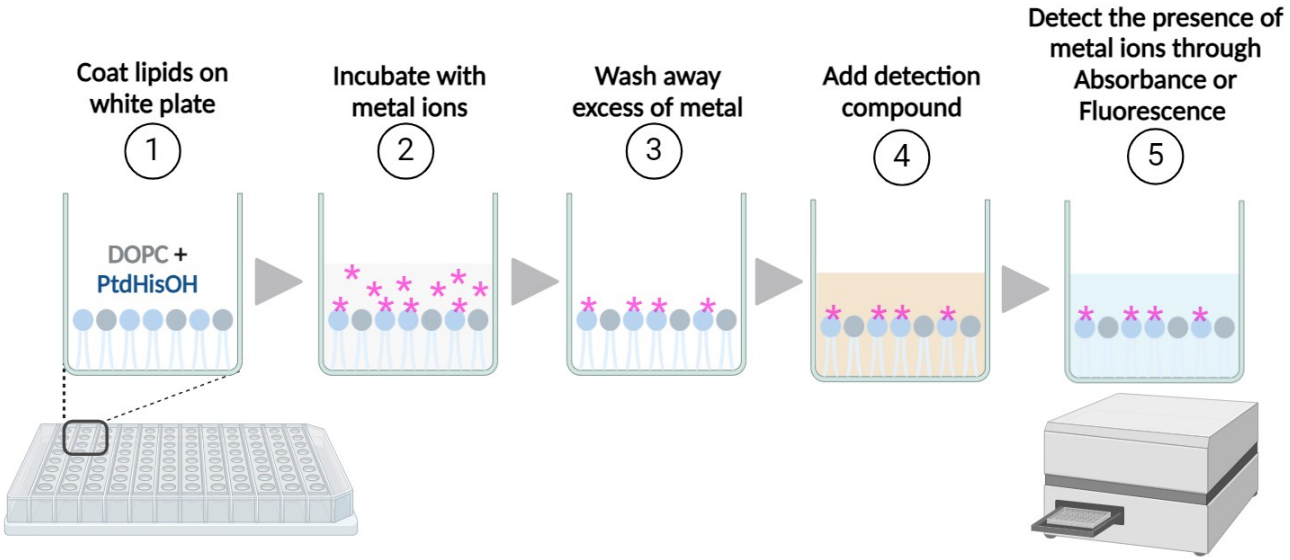


*Figure 4.1 – Schematic of the assay development for the detection of metal binding. (**1**) A mix of DOPC and PtdHisOH in Chloroform : Methanol (1:1.5 v/v) is coated at the bottom of a well, following standard lipid coating procedures (methods chapter – section 2.2.1.). (**2**) Incubate the lipids with an excess of metal ions in HEPES buffer pH 7.4. (**3**) Wash the abound metal ions away by removing the supernatant and washing the well with HEPES buffer pH 7.4. (**4**) Add the detection compound to the wells (zincon, calcein). (**5**) Detect the change in absorbance or fluorescence using a plate reader.*

For the detection assay development, Cu^{2+} was chosen as metal ion as it offers several advantages, including stronger binding, ease of detection, and intrinsic absorbance properties that can be exploited [164]. A selection of other metal ions (Zn^{2+}, Co^{2+}, Fe^{2+}) that have shown to form complexes with histidine in literature will be tested later on.

4.1.1. Zincon: a chelating chromophore

Zincon monosodium salt (ZI) is one of the most commonly used colorimetric reagents for the detection of Zn^{2+} and Cu^{2+}, as well as other metals such as Co^{2+} and Ni^{2+} [165-167]. Its simple spectroscopic detection makes Zincon the ideal probe for determining the functionality of the new lipid.

To confirm values from literature showing an absorbance of peak at 599 nm for the Cu^{2+}/Zincon complex (CuZI), an absorbance spectrum and a Cu^{2+} titration curve was done.

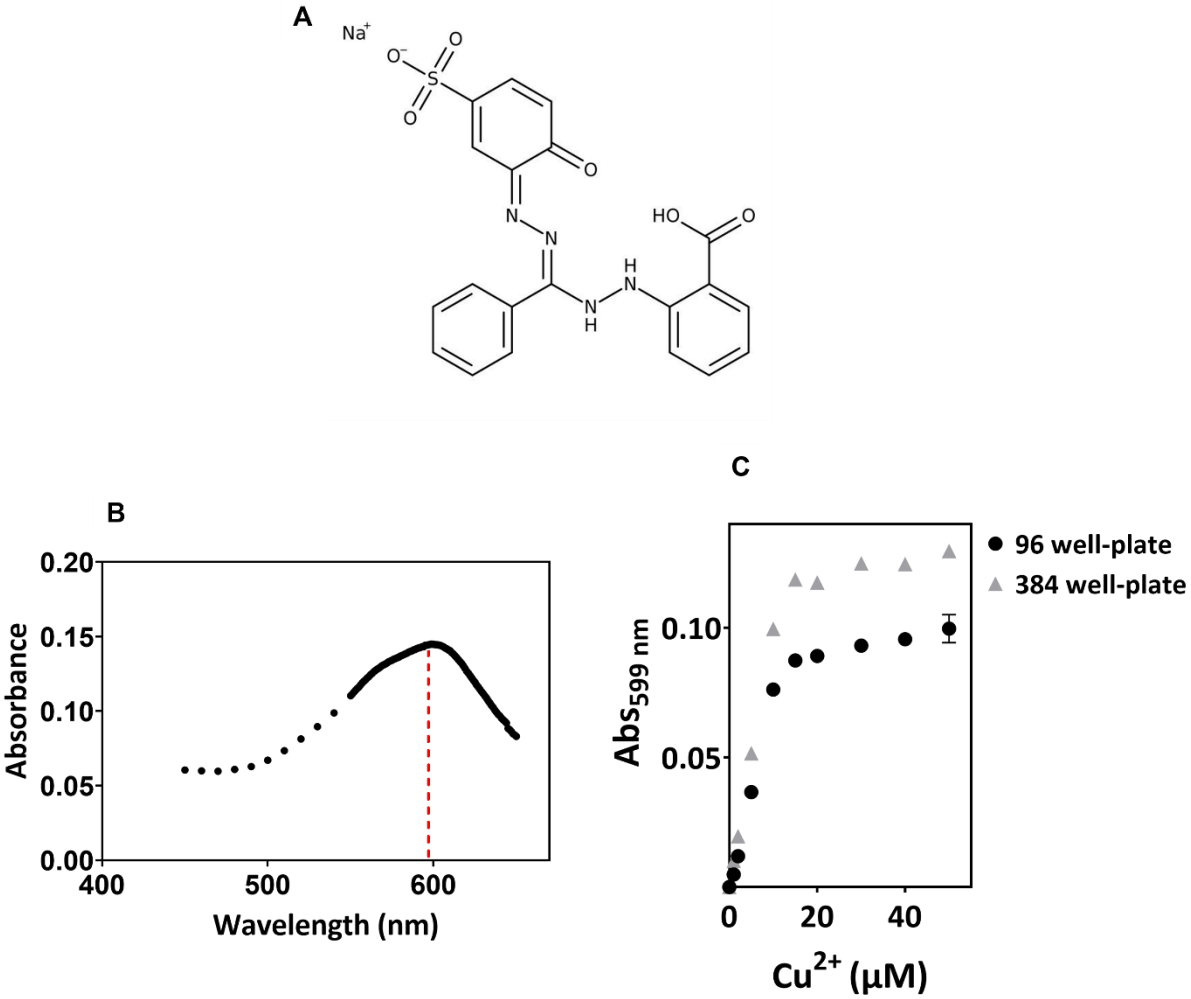


Figure 4.2 – Detection optimisation for ZI/Cu2+ complex. The measurements were done in clear 96-well or 384-well plate and measured with a UV-vis spectrometer. (A) Chemical structure of Zincon Monosodium Salt. (B) The absorbance spectrum for the complex CuZI is measured in a 96-well plate where 20µM Cu2+ and 20 µM Zincon are mixed in a HEPES buffer at pH 8.2. (C) A titration curve was done using the indicated concentrations of Cu2+ and 20 µM Zincon in HEPES pH 8.2, both in a 96 and 384-well plate. The data shows an average of n=3 replicates with the standard deviation shown as error.

Figure 4.2-B shows the absorbance spectrum of CuZI at pH 8.2, with a peak at around 599 nm.

This data is consistent with values from the literature [165].

Figure 4.2-C shows the titration curve was conducted in both a clear 96-well plate and a clear 384-well plate to increase the path length and assess if higher absorbance values can be achieved. The results from Figure 1B display two curves corresponding to the two well-plates. Both curves exhibit the same shape, with absorbance values in the 384-well

plate being higher by 0.03 a.u. at saturation compared to the values in the 96-well plate. The graph demonstrates a linear increase in absorbance between 0 μM and 15 μM of Cu^{2+}, after which both curves reach saturation at 0.1 a.u. (96-well plate) and 0.13 a.u. (384-well plate). For this experiment, a concentration of 20 μM of zincon is utilized. Saturation occurs at the same concentration of Cu^{2+}, suggesting that the reagent is depleted and that CuZI forms 1:1 complex.

The minimum detection value is determined to be 1 μM Cu^{2+}. Although increasing the path length slightly boosts the absorbance values, it does not allow reaching the literature value of 0.5 a.u. at saturation [165]. This variation may be attributed to the use of quartz cuvettes in the paper's measurements, where a volume of 2 mL of solution was utilized, making the path length much longer compared to the path length that can be achieved in a plate.

The following experiment aims to detect whether Cu^{2+} can bind to PtdHisOH in the coated system, and to determine the optimal pH and temperature for the detection, using the CuZI complex formation.

DOPC or a mix of DOPC-PtdHisOH were incubated with Cu^{2+} for 30 minutes. The unbound Cu^{2+} was washed away, and Zincon dissolved in different pH buffers was added to each well. Two plates were prepared in parallel, one incubated at 22°C and the other at 45°C.

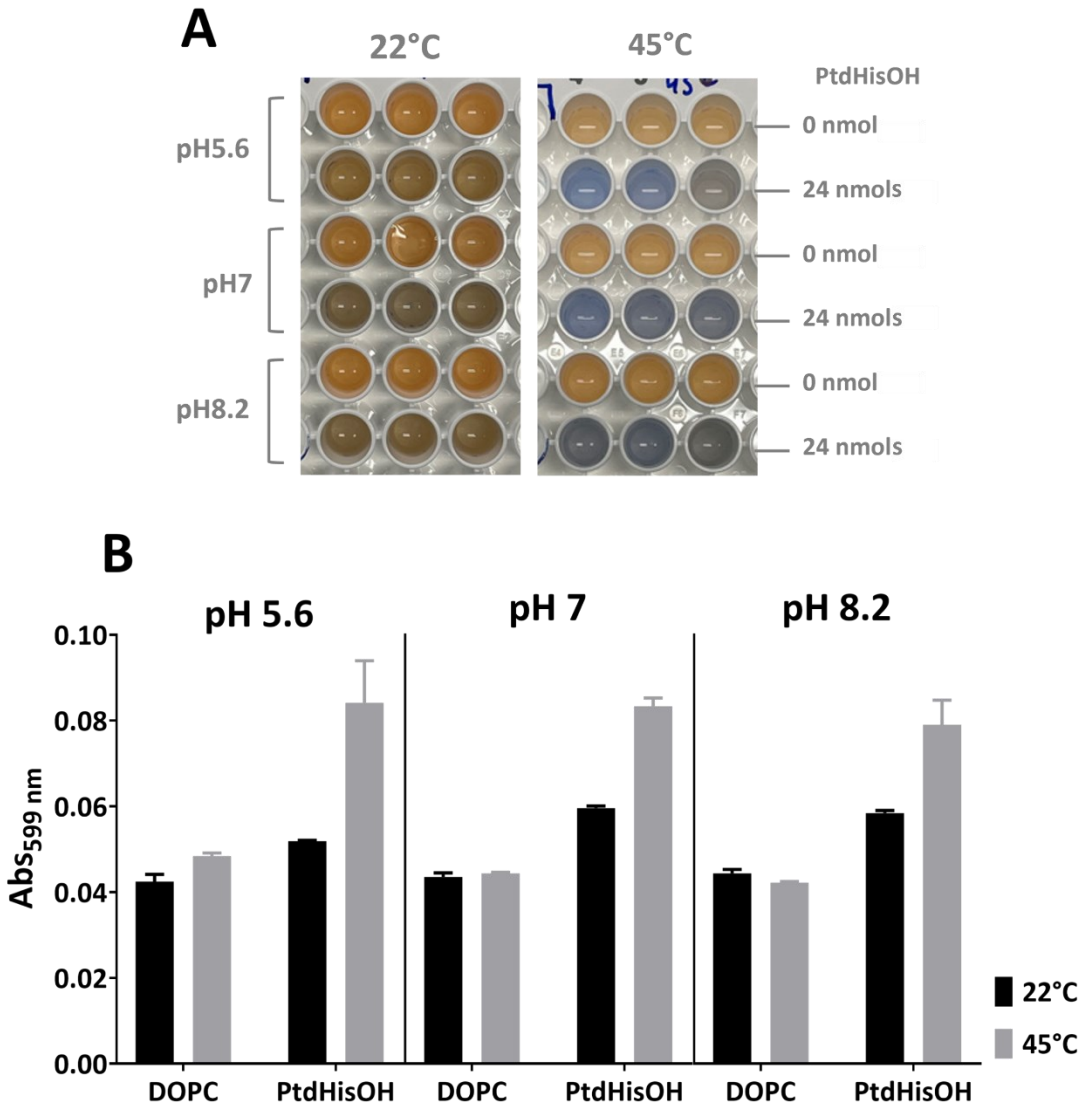


Figure 4.3 – Detection of Cu^{2+} bound to coated PtdHisOH. Either 50 nmol of DOPC or 24 moles PtdHisOH (and 25 nmol DOPC) are coated on the bottom of a white 96-well plate. The lipids are incubated with 1 mM Cu^{2+} (= 100 nmol) for 30 minutes, and the excess of Cu^{2+} is washed away. Subsequently, 20 µM Zincon at pH 5.6, pH 7.0 or pH 8.2 is added to the corresponding plate and incubated either at room temperature or 45°C for 30 minutes. The results are visually assessed (**A**) and the aqueous solution is transferred into a clear 96-well plate for absorbance measurements at 599nm. (**B**). The data shows an average of n=6 replicates with the standard deviation shown as error.

In Figure 4.3-A, a clear change in colour is observed in the wells coated with DOPC-PtdHisOH compared to those coated only with PC, transitioning from orange to a brownish colour at room temperature (22°C) and blue at 45°C. However, the colours are very similar at all three tested pH levels. Figure 4.3-B corresponds to the absorbance measurement for this experiment, for the control DOPC and for the DOPC-PtdHisOH.

The results show that Cu^{2+} is detected in the presence of PtdHisOH at room temperature (22°C) and incubating the plate at elevated temperatures enhances CuZI complex formation. The experiment also shows that the there is no pH dependency for the CuZI, which is in line with literature [165]. A buffer at pH 7.4 will be used for the next experiments based on literature.

The next experiment is a dose-response curve for PtdHisOH to evaluate the effect of increasing lipid concentrations on metal binding. The experiment is conducted at pH 7.4, at both 22°C and 45°C, with constant concentrations of Cu^{2+} and Zincon.

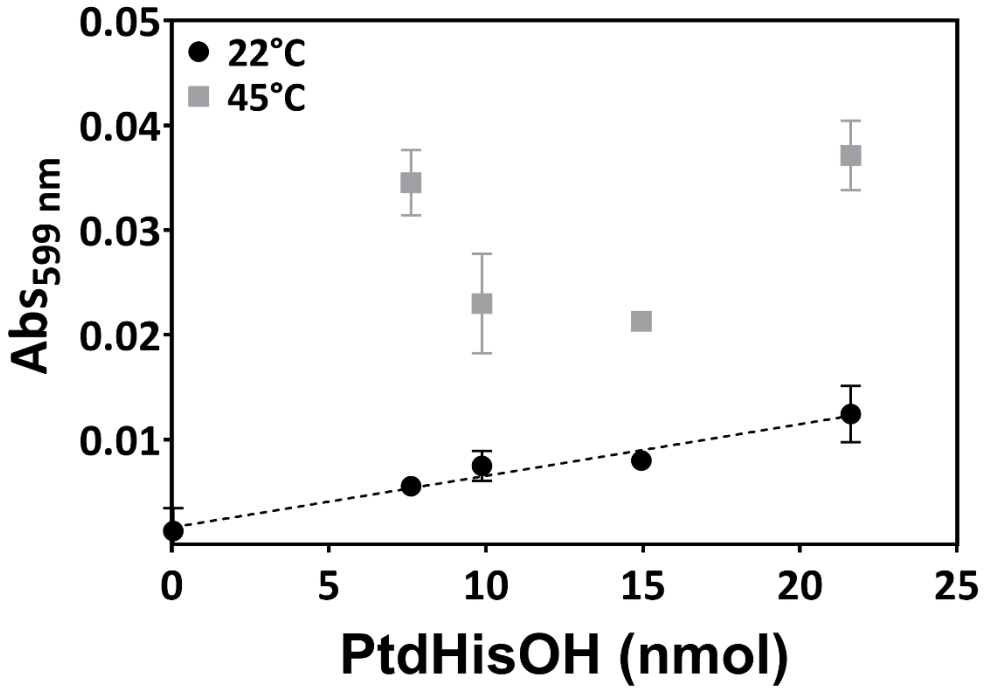


Figure 4.4 – PtdHisOH dose response for the binding of Cu^{2+}. An increasing amount of PtdHisOH is coated on a white 96-well plate, as indicated on the x-axis, with the remaining lipid to reach 50 nmol being DOPC. The lipids are incubated with 1 mM Cu^{2+} for 30 minutes, followed by washing away the excess Cu^{2+}. Subsequently, 20 µM Zincon at pH 7.4 is added to each well, and the plate is incubated either at room temperature or at 45°C for 30 minutes. The aqueous phase is transferred to a clear plate for absorbance measurements at 599 nm. The black dots correspond to the experiment conducted at 22°C, and the grey squares to the experiment conducted at 45°C. n=6.

For the experiment conducted at 22°C, a slow and linear increase in absorbance is observed, ranging from 0 a.u. for 0 nmol of PtdHisOH coated to 0.01 a.u. for 24 nmol of

PtdHisOH coated. This indicates that more metal is bound with higher amounts of PtdHisOH.
In the second dataset corresponding to the experiment conducted at 45°C, the absorbance varies between 0.02 a.u. and 0.04 a.u., with the variations not being correlated to the amount of PtdHisOH coated on the well.

The low increase in absorbance may be attributed to the procedure used for this experiment. A white plate is needed for lipid coating, and a clear plate is needed for absorbance measurement. By transferring the supernatant from a white plate to a clear plate after incubation, part of the sample might be lost. In the presence of PtdHisOH in the coating, some residual blue colour remains in the coating and can't be transferred to the clear plate. For this reason, absorbance measurements might not be optimal for these experiments. Therefore, a fluorescent probe may be more suitable as the whole experiment would be done in the same well in a white plate.

These experiments, utilizing the complex formation CuZI, allow us to conclude that PtdHisOH is functional and allows the binding of Cu^{2+}. This method showed a temperature dependency, and a pH independency, matching literature values. However, absorbance values were not as high as in literature, making the differences between conditions difficult to detect. This colorimetric tool is not optimal for the designed experiment.

4.1.2. Quenching of calcein

To enhance the detection of small amounts of metal ions bound to PtdHisOH and to align with the workflow of the designed experiments (coated lipids in a white plate), a fluorescent probe for the detection of metal ions was chosen: calcein.
Calcein's fluorescence is known to be rapidly quenched in the presence of divalent metals such as Cu(II), Zn(II), Co(II), and Ni(II) [168]. While quenching represents a loss of signal and inherently gives higher error potential compared to signal enhancement, this fluorescent dye has been successfully employed in metal ion detection in literature. Its versatility allows testing with various metals and makes it suitable for our experiment

[168-170]. Moreover, it is extensively utilized in monitoring vesicular mechanics, hinting at potential future applications for this lipid [131, 171].

The first step is to determine the minimum amount of Cu^{2+} that can be detected with calcein to establish the detection limit. A fluorescence emission spectrum (Figure 4.5-A) is conducted with increasing amounts of Cu^{2+}.

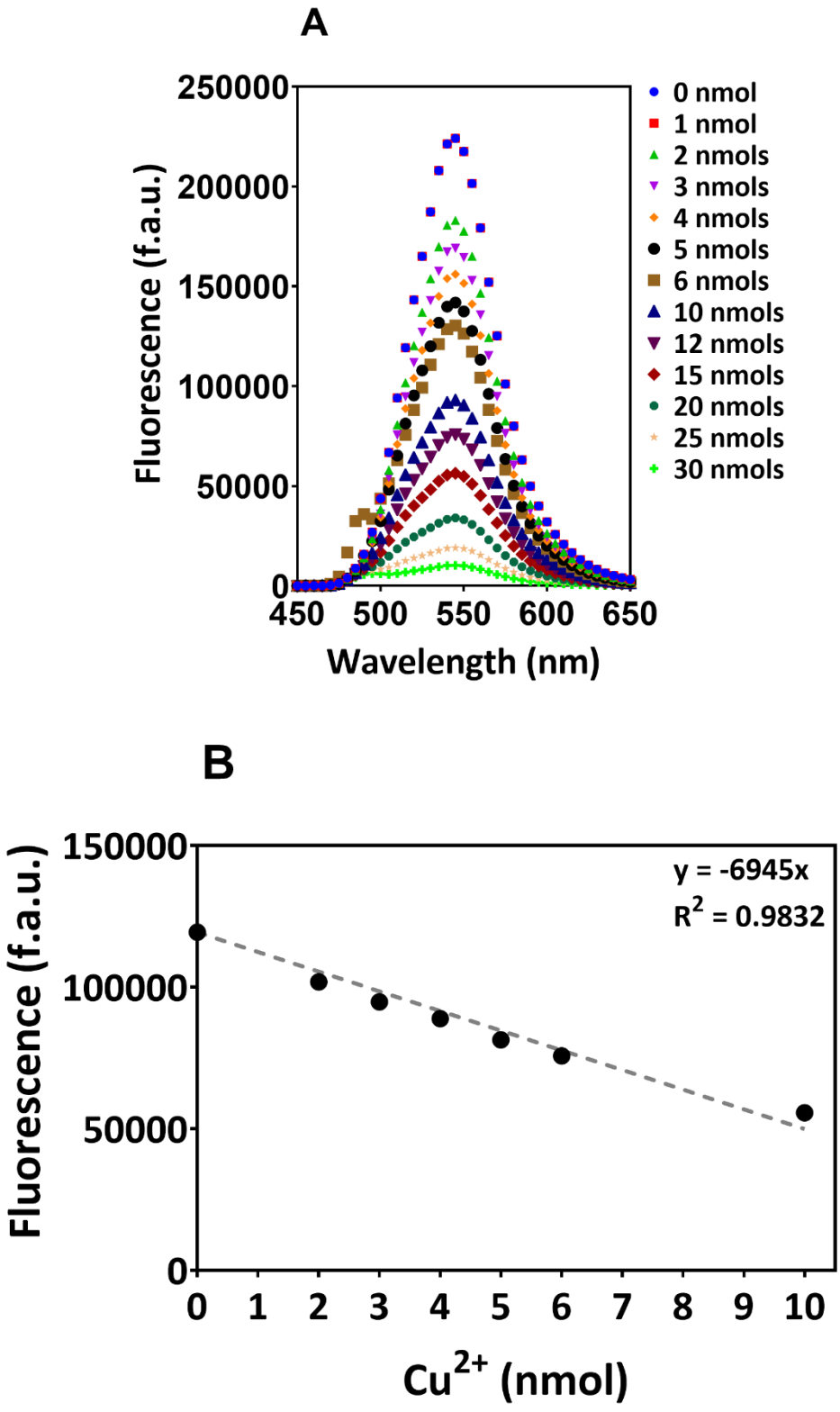


*Figure 4.5 – Calibration curve for calcein quenching by Cu^{2+}. The emission spectrum for calcein incubated with the indicated amount of Cu^{2+} is done at $Ex_{496\,nm}$ with 0.25 mM of calcein (**A**). The calibration curve for calcein/Cu^{2+} at $Ex_{496\,nm}$ and $Em_{599\,nm}$ is then calculated, with a slope y = -6945x (**B**). An average of n=2 repeats is shown.*

Figure 4.5-A corresponds to the emission spectrum for calcein excited at 496 nm in the presence of increasing amounts of Cu^{2+}. The emission peak remains consistent for all metal concentrations; however, the intensity of fluorescence decreases as the concentration of metal increases. The decrease in fluorescence becomes detectable from 2 nmol of Cu^{2+} onwards, establishing the detection limit of this fluorescent dye to 2 nmol. This is comparable to the sensitivity achieved in the zincon calibration curve (Figure 4.2-B).

Figure 4.5-B is the standard curve for the quenching of calcein by Cu^{2+} at $Ex_{496\,nm}$ and $Em_{515\,nm}$. The plot demonstrates a linear regression between 0 and 10 nmol of Cu^{2+}.

The objective of the following experiment is to determine the correlation between the amount of PtdHisOH coated and the amount of Cu^{2+} detected using calcein. To do so, increasing amounts of PtdHisOH were coated in a 96-well plate, followed by incubation with constant concentrations of Cu^{2+}. Subsequently, the unbound metal was washed away, and calcein was added to each well. The decrease in fluorescence was monitored using a plate reader (see figure 4.1).

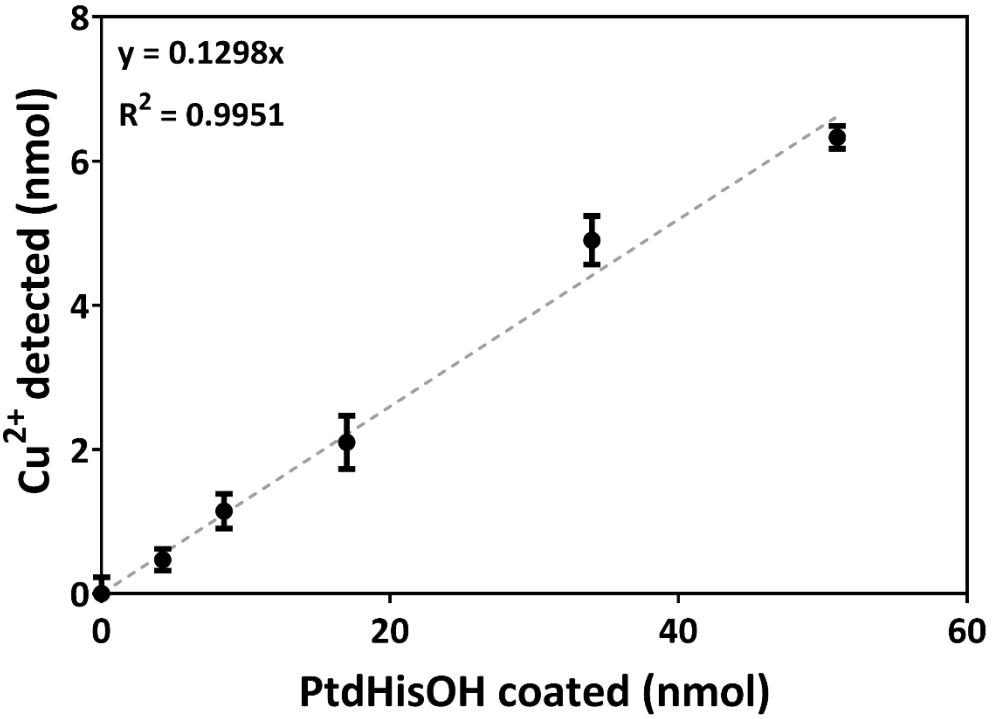


Figure 4.6 – Dose-response curve for gradient PtdHisOH coated and bound Cu^{2+}. Increasing amounts of PtdHisOH as indicated on the graph complemented with DOPC to reach 50 nmol total lipid, are coated on a white 96-well plate. The plate is incubated with 1 mM Cu^{2+}, and the excess of Cu^{2+} is washed away. 0.25 mM calcein in buffer at pH 7.2 was then added to each well and the quenching was measured in a spectrometer at Ex_{496} and Em_{515}. The amounts of Cu^{2+} detected were calculated from the standard curve. n=6.

Figure 4.6 illustrates the correlation between the amount of PtdHisOH coated and the amount of Cu^{2+} detected. A linear increase in Cu^{2+} detected is observed from 0 nmol to 50 nmol of PtdHisOH coated. For 20 nmol of PtdHisOH lipid coated, there is about 2.4 nmol of Cu^{2+} detected, indicating a ratio of lipid to metal of 8:1.

Using calcein for the detection of Cu^{2+} bound to PtdHisOH maintains the same level of sensitivity as with Zincon. This novel assay enables the determination of the amount of metal bound depending on the density of PtdHisOH in the coating. This experiments also demonstrate that the loss of material during the transfer of the supernatant from a white to a clear plate in the coating experiments with zincon is significant, as detecting the increase in metal bound to the increasing amounts of PtdHisOH coated becomes challenging. The development of a high-throughput method to determine the functionality of the novel lipid PtdHisOH is validated.

4.2. Functionality through protein binding in the coating

To further assess the metal binding capacity of PtdHisOH and explore one of its applications, the ability to bind His-tagged proteins via metal ions was tested. The experiment was optimized with Cu^{2+}, and metal selectivity was subsequently tested with other metal ions.

For the his-tagged protein, a monomeric EGFP protein was chosen due to its versatility and ease of detection, both in a UV-spectrometer and by microscopy, for future experiments.

His-mEGFP was produced in *E. coli* and purified following standard synthetic biology procedures, as detailed in the methods chapter (section 2.7).

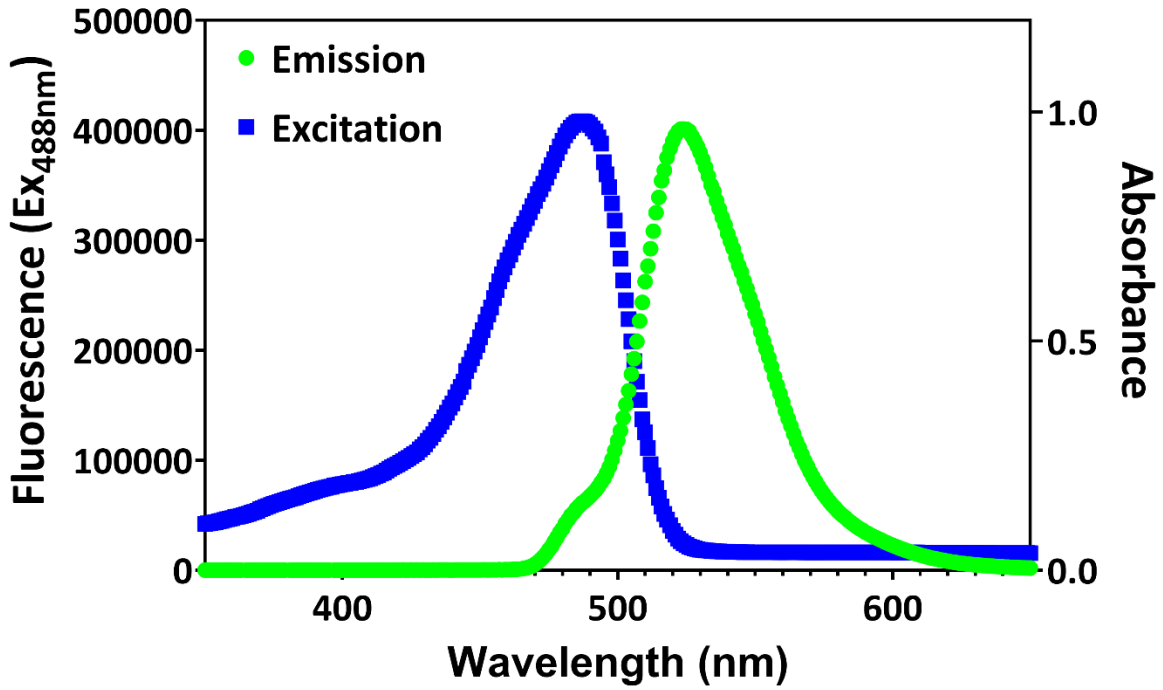


Figure 4.7 – Excitation (blue) and emission (green) spectra of his-mEGFP in buffer pH 7.4. 200 µM of his-mEGFP in HEPES buffer pH 7.4 is added to a clear plate for the absorbance scan (excitation curve), or to a white plate for the fluorescence scan (emission curve with $Ex_{488\ nm}$). Measurements are done in a spectrometer.

The absorbance/emission spectrum is shown in Figure 4.6, with $Ex_{487\ nm}$ and $Em_{520\ nm}$. The excitation values are the same as those reported in the literature, and the emission peak is similar, though shifted by 10 nm [172].

4.2.1. His-mEGFP - PtdHisOH binding through Cu^{2+}

The aim of this experiment is to determine whether a the PtdHisOH lipid can bind his-tagged proteins through the metal ion Cu^{2+}.

Studies have shown that one molecule of Me^{2+} (Cu^{2+}, Zn^{2+} or Ni^{2+}) coordinate with two to three imidazole groups from his-tags [173, 174]. Knowing from Figure 4.6 that the metal ion (in this case Cu^{2+}) is already in coordination with the imidazole groups from the PtdHisOH lipid, a calibration curve with excess PtdHisOH lipid coated, Cu^{2+}, and known amounts of his-mEGFP was done (Figure 4.8).

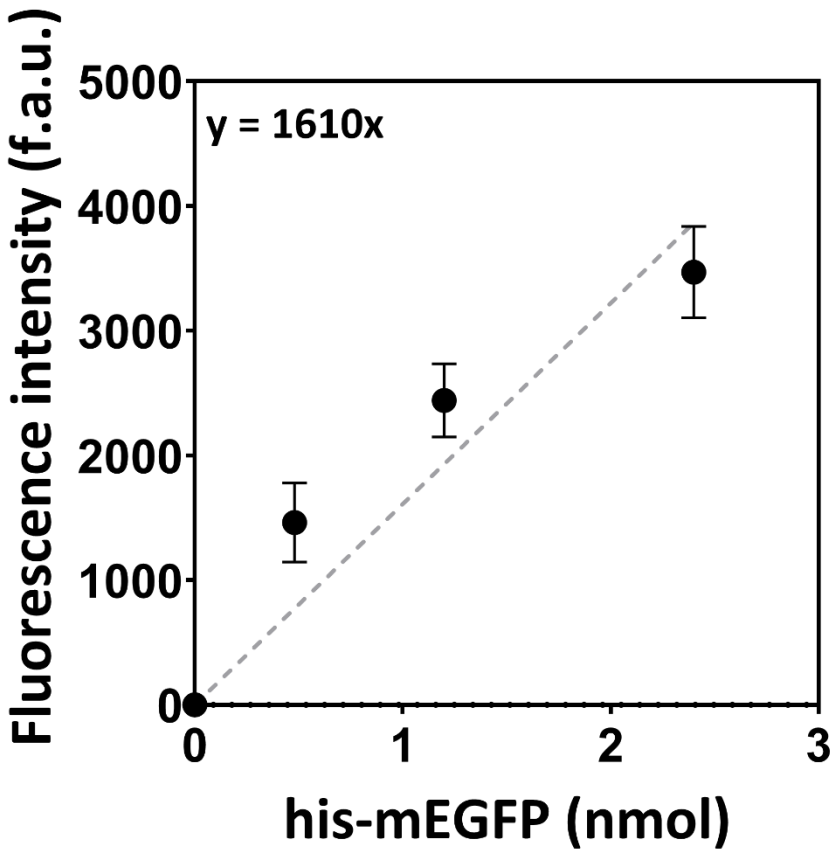


Figure 4.8 – his-mEGFP calibration curve in the coating system with PtdHisOH and Cu^{2+}. 16 nmol of PtdHisOH were coated in a well supplemented with DOPC. The lipid coating was incubated with an excess of Cu^{2+} 300 µM, and the unbound metal was washed. The indicated amounts of his-mEGFP were finally added to each well. This calibration curve was used to normalise the data from the following experiments.

The experiment begins by coating the surface with increasing amounts of PtdHisOH and incubating the lipid with Cu^{2+} for 30 minutes. After incubation, any unbound Cu^{2+} is

removed through washing, as done previously. Subsequently, His-tagged mEGFP is added to each well, followed by washing away any excess protein after another 30-minute incubation period.

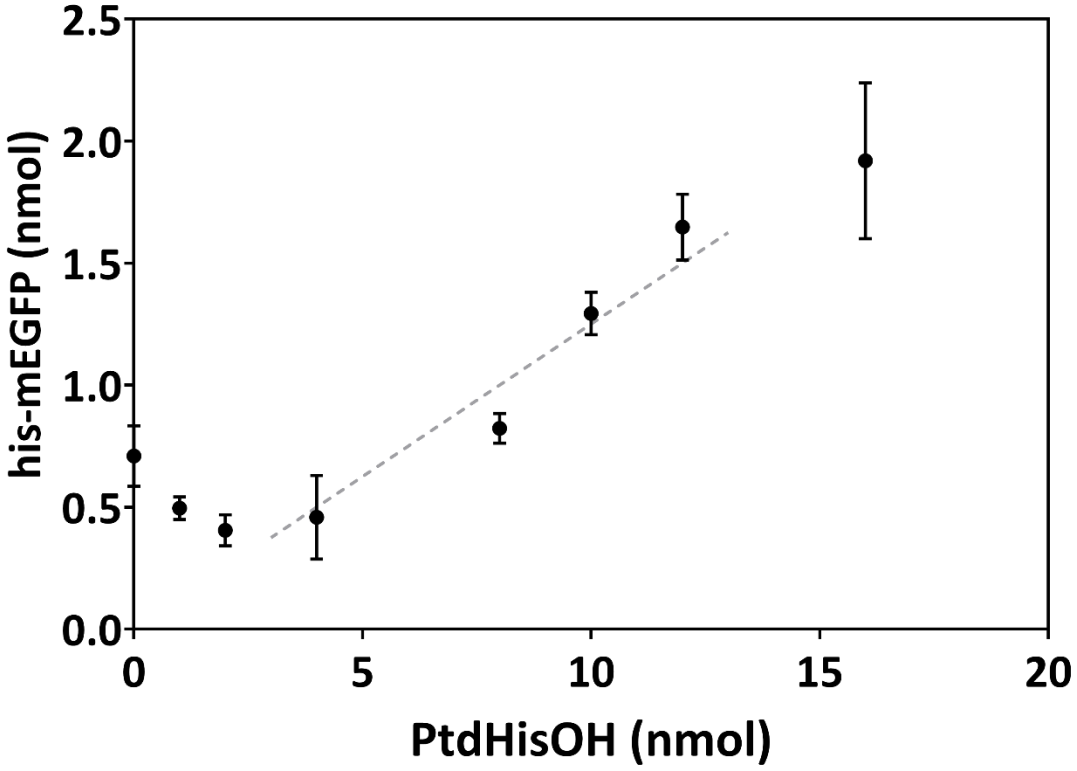


Figure 4.9 – his-mEGFP detected with gradient PtdHisOH coated. Gradient amounts of PtdHisOH are coated in a 96-well plate as indicated on the graph. The lipids are incubated with 300 µM Cu^{2+} for 30 min. The excess of metal is washed away, and 100 µM his-mEGFP is added to the wells and incubated for 30 more minutes. The excess of his-mEGFP is washed away. 100 µL of buffer is added into each well for fluorescence readings in a spectrometer. Amounts of his-mEGFP are normalised according to the calibration curve in Figure 4.6. The experiment shows n = 6 replicates with the standard deviation being shown as error.

Figure 4.9 shows his-mEGFP amounts ranging between 0.5 to 2 nmol with 0 to 4 nmol of PtdHisOH coated. A linear increase in his-mEGFP bound is observed from 4 to 12 nmol of PtdHisOH coated, reaching saturation with 18 nmol of PtdHisOH coated, at around 2 nmol of his-mEGFP. The initial fluorescence from 0 to 4 nmol can be attributed to background fluorescence resulting from the nonspecific interactions of his-mEGFP with polystyrene [175, 176]. The increase in fluorescence from 8 to 16 nmol is attributed to the

increase in bound his-mEGFP. This result indicates that the protein binds the lipid through the Cu^{2+} successfully.

4.2.2. Testing other metals

To assess the metal selectivity of PtdHisOH and his-mEGFP binding, various metal ions are tested in the following experiment. Zinc (Zn^{2+}) is chosen as it is the preferred metal ion due to its biological relevance. Additionally, Cobalt (Co^{2+}) is tested, as it was used in the column for purifying the his-mEGFP. Ni^{2+} is also commonly used for his-tagged protein purification but was not chosen for this study due to its high toxicity, which makes it not applicable for the artificial cell environment. Iron (Fe^{3+}) is included as a control, as it is not used for binding his-tagged proteins in literature.

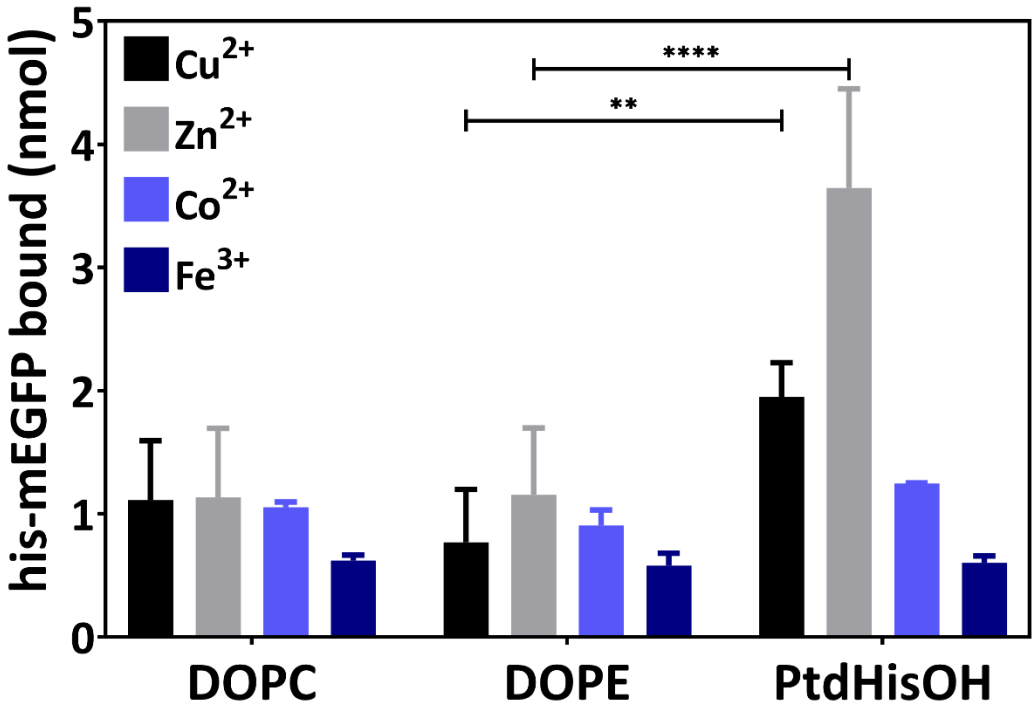


Figure 4.10 – Metal selectivity of PtdHisOH and his-mEGFP binding. A 96-well plate is coated with 40 nmol of lipid (100 mol% PC, 70 mol% PC-30 mol% PE or 70 mol% PC-30 mol% PtdHisOH). The lipids are incubated with 300 µM of the indicated metal for 30 minutes, before washing the unbound metal away. 100 µM his-mEGFP is added to the wells and incubated for 30 more minutes. The excess of his-mEGFP is washed away. 100 µL of buffer is added into each well for fluorescence readings in a spectrometer. The experiment shows n = 6 replicates with the standard deviation being shown as error.

Figure 4.10 shows the binding of his-mEGFP through different metal ions, with PC, PE or PtdHisOH coated. PC and PE are used as controls, as PC is mixed with PtdHisOH and PE carries an amine group such as PtdHisOH. Fe^{3+} is also used as a control to set the baseline.

The graph shows similar values for PC with any of the metal ions, around 1 nmol of his-mEGFP detected, with slightly lower values with Fe^{3+}. Similarly, PE shows stable his-mEGFP binding, around 1 nmol, with a slight reduction with Fe^{3+}. This data showing no difference between DOPC and DOPE proves that the amino group contained in DOPE and PtdsHisOH does not participate in the protein binding.
In contrast, PtdHisOH demonstrates significantly higher amounts of his-mEGFP bound with Zn^{2+} (4 nmol), and with Cu^{2+} (2 nmol of his-mEGFP bound) compared to DOPC or DOPE. While there is detectable protein binding with Co^{2+}, it is not significant enough to be applied in the next experiments. This might be due to the low affinity of Co^{2+} to his-tagged proteins, compared to Zn^{2+} and Cu^{2+}. The values for Fe^{3+} are comparable to the controls with PC or PE.
Cu^{2+} exhibits the strongest affinity for his-tagged proteins. Consequently, the introduction of his-mEGFP may displace some of the Cu^{2+} ions bound to the lipid [177, 178]. Zn^{2+}, on the other hand, has a slightly lower affinity for his-tags, enabling binding from both the his-tagged protein and the lipid.

This research on the binding capacities of the PtdHisOH lipid reveals that the lipid can bind divalent metal ions through the imidazole group. Achieving a certain density of the PtdHisOH lipid is necessary to facilitate binding, and adjusting this density can either enhance or diminish the strength of the bonds. Among the metal ions tested, Zn^{2+} gives the best results and will be used in future applications.
The chapter demonstrates the functionality of the PtdHisOH lipid in binding metal ions such as Zn^{2+} and Cu^{2+}. It also illustrates the lipid's ability to bind a his-tagged protein, specifically his-tagged mEGFP, mediated by a metal ion, with Zn^{2+} exhibiting the strongest binding affinity.

4.3. Conclusions & future work

Chapter 4 dives into the characterisation of the functionality of the lipid and more particularly its ability to bind metal ions. Within this chapter, a high-throughput method was established using the coating system to determine the optimal conditions for the binding. The experiments revealed that a minimum density was necessary to ensure proximity between PtdHisOH lipids. Moreover, the binding capability within the coating system was also employed to capture his-tagged mEGFP through the lipid. Results demonstrated successful his-tagged protein capture facilitated by the metal ion, with zinc ions Zn^{2+} being the most effective among the metals tested.

5. Chapter 5: Catalytic properties of PtdHisOH

Catalytic artificial cells could offer intriguing possibilities for mimicking and better understanding some biological processes, as well as being used for novel biomedical and biotechnological applications. Enzymes are integral to various cellular functions, and incorporating lipids with catalytic abilities could contribute to the reconstruction of sensory pathways involved in cell signalling and communication [179, 180]. Additionally, such catalytic lipids could play a role in regulating metabolic pathways within artificial cells [181].

Moreover, catalytic lipids hold promise in biomedicine for the development of on-site responsive drug synthesis, potentially enhancing therapeutic outcomes [182, 183]. This innovative approach could pave the way for advanced drug delivery systems capable of precisely tailoring drug synthesis to specific cellular needs or environmental cues.

The other important reason to investigate the catalytic abilities of the PtdHisOH lipid is to determine if incorporated into lipid membranes, the lipid could undergo auto-catalysis. This would convert the PtdHisOH lipid into a lysolipid, giving the lipid a more conical shape and therefore, impacting the membrane curvature [184].

The novel phospholipid lipid PtdHisOH carries one essential amino acid: L-histidine. L-Histidine is the only naturally occurring amino acid carrying an imidazole group and has demonstrated in many studies to play a role in enzymes catalytic sites [101, 102]. The catalytic property of L-Histidine is mediated by the imidazole group that has revealed to form part in the catalytic sites of many hydrolytic enzymes [36, 94, 102, 127, 185]. More specifically, imidazole has proven to play a role as artificial enzymes such as esterases [91, 99, 100], acylases [98] and ribonucleases [96, 97].

The catalytic properties of L-Histidine enzymes have demonstrated a strong dependency on zinc as a cofactor [107, 161, 186], and zinc is particularly important for esterase activity [162, 187].

The insertion of imidazole-based lipids in artificial lipid membranes has been investigated in the past in a few studies [188, 189], but there is no evidence of the catalytic properties

of these lipids incorporated to artificial membranes. Therefore, we decided to elucidate the catalytic properties of this PtdHisOH lipid incorporated to the membrane of vesicles. Another reason to test the catalytic activity of the lipid is as a control: the imidazole moiety is located in the headgroup of the phospholipid and could therefore access surrounding phosphodiester bonds. In the case of PtdHisOH showing a phosphodiesterase activity, the lipid could self-hydrolyse or hydrolyse the surrounding phospholipids, destroying our lipid or the vesicles formed with it. Esterase, phosphodiesterase, and phosphatase were investigated.

5.1. Catalytic abilities: esterase, phosphodiesterase, phosphatase activity

5.1.1. Phosphodiaestarase activity

Phosphodiesterases play essential roles in cellular signalling for gene expression, neurotransmission and muscle contraction by regulating the levels of nucleic acids and cyclic nucleotides [190]. Therefore, a dysregulation in PDE activity can be the cause cardiovascular and neurological disorders, as well as some types of cancers [191]. Increasing our understanding on PDEs and finding ways to inhibit their activity is crucial for new therapies.

Phosphodiesterase activity is also important to be tested as a control for the incorporation of the PtdHisOH into liposome membranes. It is described in literature that imidazole can catalyse phosphodiester bonds [192, 193]. In the case of our lipid, the imidazole can access the phosphate group, as it is located in the headgroup. This implies that PtdHisOH that if phosphodiesterase activity is detected, the lipid could be autocatalytic. This would result in a membrane containing lysolipids, changing its properties and curvature drastically.

Bis(p-nitrophenyl) phosphate has been widely used to estimate the phosphodiesterase activity (PDE activity) of an enzyme or a compound, including PLD [123, 124, 194]. It is a colorimetric compound that strongly absorbs at 405 nm when hydrolysed and in alkaline conditions. The colour change is also detectable by eye, with the solution being clear and turning yellow when hydrolysed, as it releases 4-nitrophenol. BNPP catalysis has shown

to be boosted by the presence of Zn^{2+} [195]. The PDE activity will be tested both without and with the presence of Zn^{2+}.

As detailed in the methods chapter (section 2.3.1), 200 nm LUVs were prepared and incubated without or with Zn^{2+}. 1 mM BNPP was added to all reactions and $Abs_{405\ nm}$ was measured using a spectrometer.

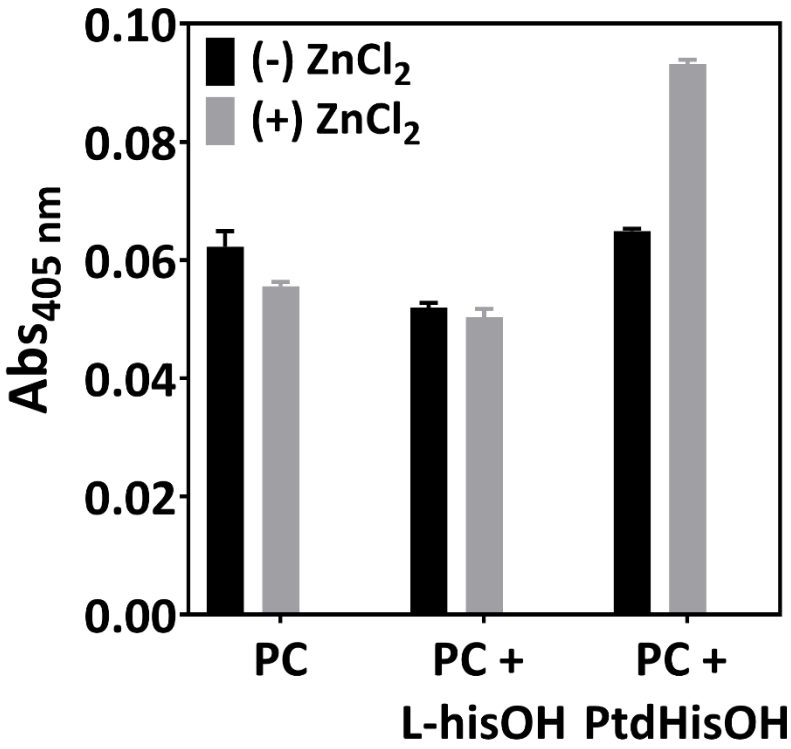


Figure 5.1 – Preliminary experiment for phosphodiesterase activity of PtdHisOH in LUVs. Vesicles containing PC 100 mol%, PC 100 mol% with L-Histidinol and PC 70 mol%-PtdHisOH 30 mol% were incubated with 1 mM bNPP and no metal (buffer) or Zn^{2+} for 30 minutes. Average of 2 separate experiments with triplicates (n = 6) and SD are shown.

In Figure 5.1, both conditions (no metal or Zn^{2+}) have similar absorbance values for PC vesicles, around 0.06 a.u. and for PC vesicles with L-Histidinol, around 0.05 a.u. The absorbance values in samples with PC-PtdHisOH vesicles are higher. When no metal is added, the absorbance is 0.065 a.u., so close to the control values. However, in the presence of Zn^{2+}, the absorbance values increase and reach 0.095 a.u.

This data suggests that the presence of PtdHisOH in LUVs together with a zinc boosts the PDE activity above the background absorbance values by 0.03 a.u.

To obtain a boost in PDE activity from PtdHisOH, one parameter that can be changed is temperature [196]: increased temperatures have shown in some bacterial PDEs an increased catalytic activity. Therefore, the same experiment was tried with Zn^{2+}, as it gave the best values, at 37°C and 50°C.

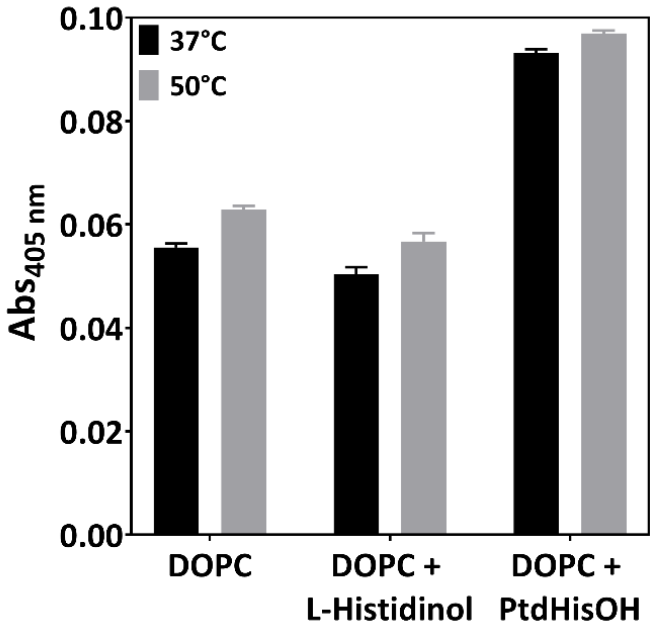


Figure 5.2 – Temperature gradient for phosphodiesterase activity of PtdHisOH in LUVs. Vesicles containing PC 100 mol%, PC 100 mol% with L-Histidinol and PC 70 mol%-PtdHisOH 30 mol% were incubated with 1 mM BNPP and Zn^{2+} at 37°C or 50°C for 30 minutes. Average of 2 separate experiments with triplicates (n = 6) and SD are shown.

For the three samples, the absorbance is slightly higher at 50°C than at 37°C, by about 0.005 a.u. (Figure 5.2). These values indicate that the PDE-like activity identified in PtdHisOH LUVs is not significantly boosted by an increase in temperature, which is not in accordance with literature. The data confirms PDE-like activity in PtdHisOH LUVs, albeit being rather low.

To further investigate the PDE-like activity in PtdHisOH LUVs, a time course was conducted to observe the evolution of the hydrolysis and measure the absorbance values over time.

PC LUVs and PtdHisOH LUVs were incubated with Zn^{2+} and BNPP for 0 to 50 minutes and the absorbance was measured at each time point.

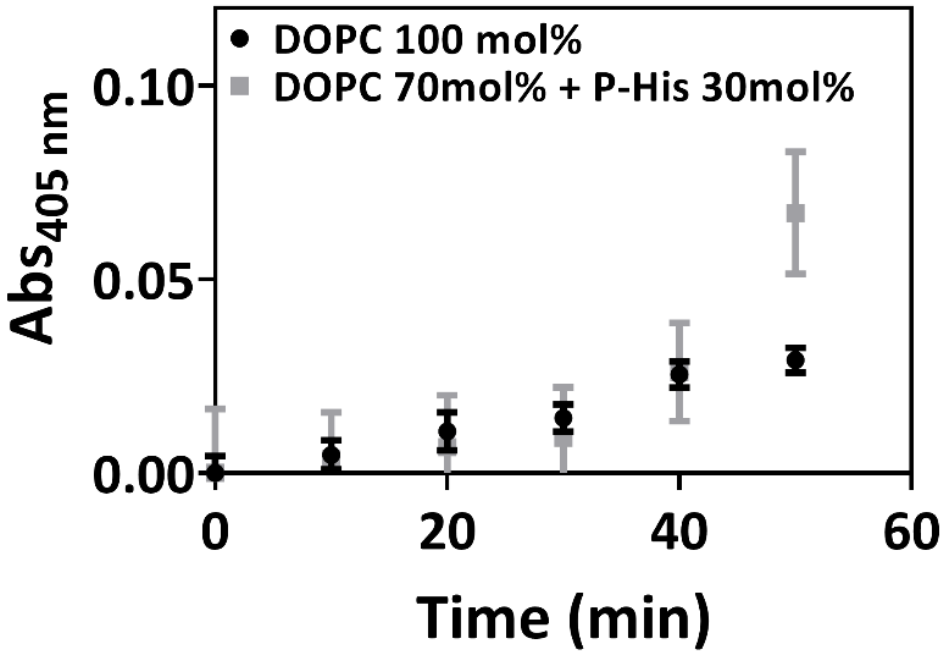


Figure 5.3 – Time course for phosphodiesterase activity of PtdHisOH LUVs. 100 mol% PC LUVs or 70 mol% PC LUVs – 30 mol% PtdHisOH LUVs were incubated for 0, 10 20, 30, 40, 50 minutes with Zn^{2+} and 1 mM BNPP. Average of 2 separate experiments with triplicates (n = 6) and SD are shown.

Figure 5.3 shows the two data sets corresponding to the time course for PC LUVs and the time course for PtdHisOH LUVs. The absorbance for the reaction with PC LUVs increases in a linear way over time, indicating a drift in the absorbance background. As discussed in Figure 1 for esterase activity, some BNPP might get hydrolysed overtime, moving the baseline from 0 to 0.025 a.u. The second data set for PtdHisOH LUVs follows an exponential growth and reaches 0.07 a.u. after 50 minutes. It is important to note that the error bars also increase over time, suggesting variability among the replicates. A noticeable increase in turbidity is observed visually in the wells containing PtdHisOH/Zn^{2+} over time, changing from a clear solution to an opaque solution. The increase in absorbance observed might therefore be due to the increase in opacity instead of the detection of hydrolysis. Moreover, there is only one observable absorbance difference between PC LUVs and PtdHisOH LUVs at the last time point.

The next experiment was done to elucidate the opacity increase and to conclude on the potential PDE-like activity. In this assay, BNPP was used, as well as pNPP. The hydrolysis of BNPP releases both a nitrophenol compound, and a pNPP molecule, so here, the two activities were tested (more on phosphatase activity in section 5.1.2). LUVs with an increasing concentration of PtdHisOH ranging from 0 mol% to 30 mol% were extruded. The LUVs were incubated either with Zn^{2+} only for the absorbance control, or with Zn^{2+} and BNPP, or Zn^{2+} and pNPP for the investigation of phosphatase activity. The objective is to measure the absorbance attributed to the increase in cloudiness, that might be due to LUVs clustering/binding together, and the absorbance attributed to the hydrolysis of the substrates BNPP or pNPP, releasing 4-nitrophenol.

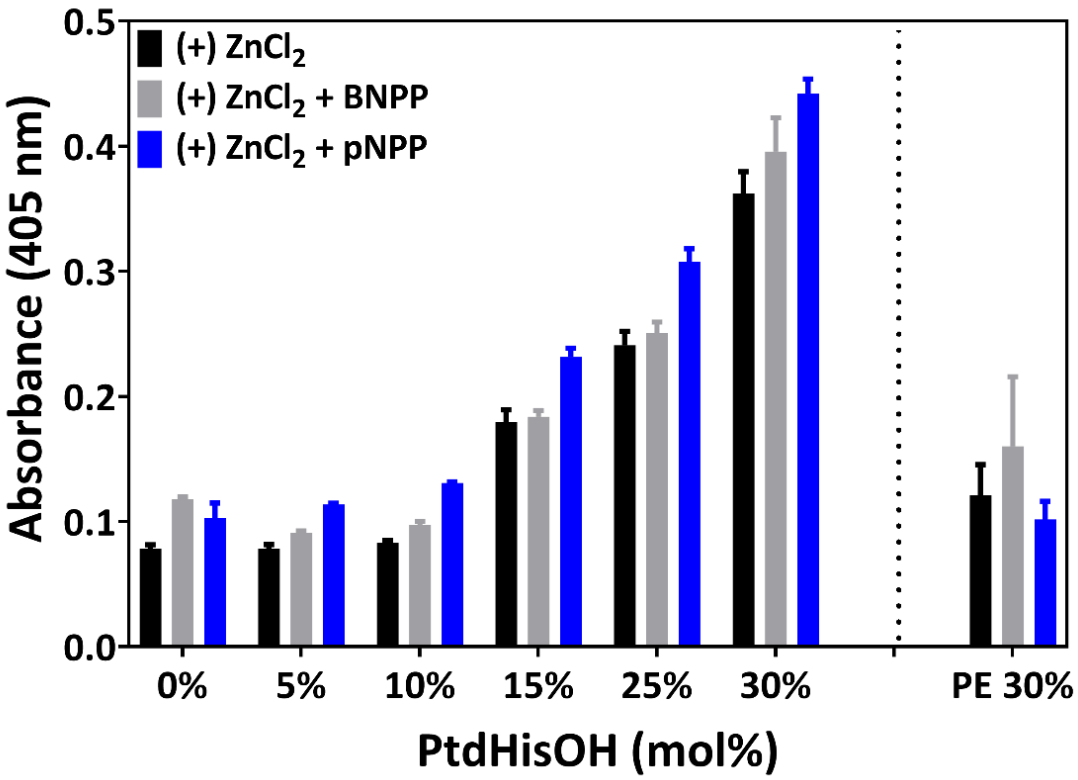


Figure 5.4 – Correlation between Abs_{405nm} and concentration of PtdHisOH in the presence of Zn^{2+}. LUVs with increasing amounts of PtdHisOH (0, 5, 10, 15, 25, 30 mol%) were incubated with Zn^{2+}. The Abs405nm was measured and compared to the Abs_{405nm} in the presence of the substrates 1 mM BNPP or 1 mM pNPP. Average of 2 separate experiments with triplicates (n = 6) and SD are shown.

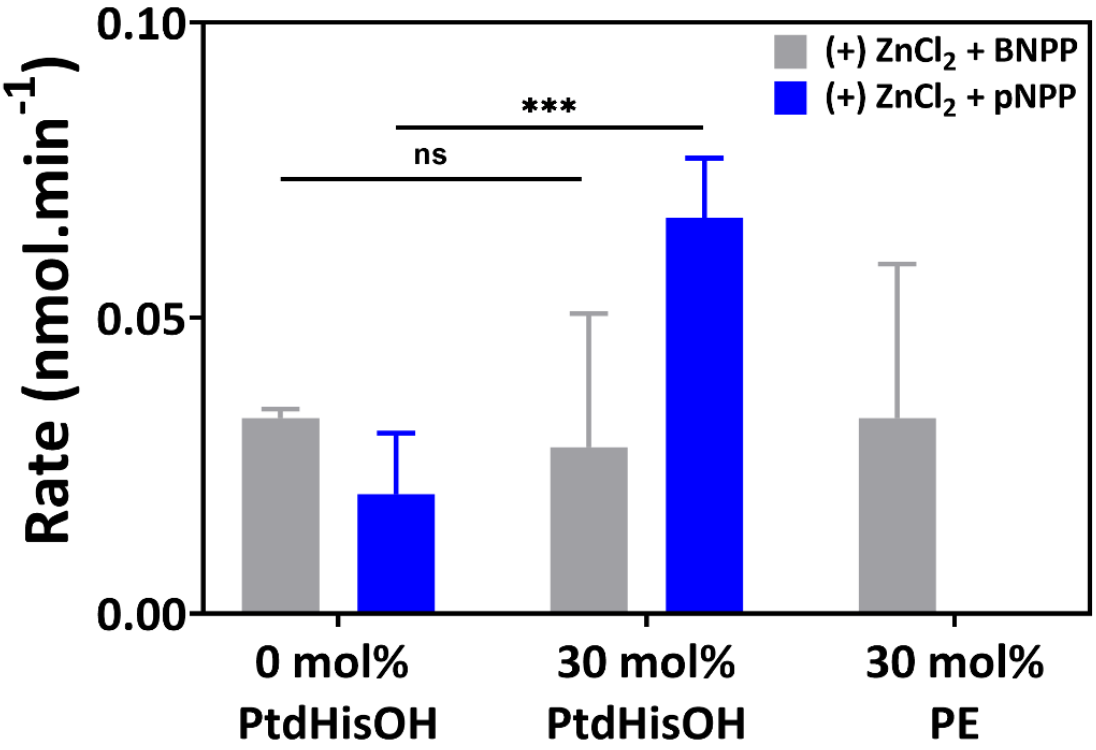


Figure 5.5 – Catalytic rates for 30 mol% PtdHisOH LUVs. Catalytic rates were calculated from the absorbance values in Figure 5.4. The data represents the catalytic rates where the background absorbance has been taken into account.

In Figure 5.4 and for the samples with PtdHisOH LUVs and Zn^{2+}(black), no increase in absorbance can be observed from 0 mol% to 10 mol%, with values below 0.1 a.u. From 15 mol%, we observe an exponential increase in absorbance reaching about 0.35 a.u. at the maximum PtdHisOH concentration. The same trend is observed for samples with BNPP and pNPP. For BNPP, the background absorbance between 0 mol% and 10 mol% is also just below 0.1 a.u. For the biggest concentration of PtdHisOH, the absorbance reaches 0.4 a.u. The values for BNPP are always equal or within the error of the absorbance values without BNPP, indicating that the lipid is not catalytic towards this compound as the absorbance measured is only due to increase in opacity. PDE-like activity of PtdHisOH can therefore be discarded.

Regarding the samples incubated with pNPP, the absorbance values from 0 to 10 mol% are around 0.1 a.u. and increase exponentially from 10 to 30 mol%, reaching 0.45 a.u. at the highest. The increase in absorbance is also correlated with the absorbance increase of LUVs with Zn^{2+} alone, but the difference between the two values is significant and not

within the error. The delta in absorbance increases from 0.05 a.u. at 15 mol% PtdHisOH to 0.08 a.u. at 30 mol%.

Figure 5.5 shows the catalytic rates calculated from the absorbance values. The controls indicate that PE and PC (0mol% PtdHisOH) do not show any catalytic activity. With 30 mol% PtdHisOH, there is a significant difference compared to the background for phosphatase activity only.

This experiment leads to the following conclusions:

- Low PDE-like activity is detected for PtdHisOH in the vesicular system, that can't be detected with the background absorbance.
- There is a binding/aggregation phenomenon of LUVs containing PtdHisOH in the presence of Zn^{2+}, resulting in increased turbidity and thereby affecting absorbance measurements. This phenomenon will be further investigated in Section 6.2 (chapter 6).
- The data suggests that PtdHisOH may exhibit some phosphatase activity on pNPP. This will be explored in the subsequent section.

5.1.2. Phosphatase activity

Another catalytic activity that we decided to assess with PtdHisOH is phosphatase activity. Having a lipid with phosphatase-like properties would be extremely interesting for the development of the artificial cell technology, as phosphatases play a role in many biological processes [197] and has been desceibed as a promising biomarker for diagnostic and treatment [198]. Harnessing a lipid with such functionality would represent a novel and intriguing addition to artificial cells and their utility in biomedical applications. For these reasons, we decided to investigate a phosphatase-like activity from our lipid PtdHisOH.

Compared to PDE-like activity, the presence of phosphatase-like activity would not impact our vesicle systems, as a phosphatase would not be able to hydrolyse PC or PE. Other lipids such as PA or PI (phosphatidyinositol) could be hydrolysed, and this should be considered for the application of the PtdHisOH lipid.

p-Nitrophenyl Phosphate (pNPP) is a chromogenic compound absorbing at 405 nm [125] and commonly used for the detection of phosphatase activity [126]. Similar to bNPP, upon hydrolysis, 4-nitrophenol is released, resulting in a visible color change from clear to yellow under alkaline conditions. This induces a large absorbance change that can be monitored with a spectrometer at $Abs_{405\,nm}$.

This experiment aimed to evaluate the potential phosphatase-like activity of the lipid PtdHisOH. Similar to previous assays using BNPP for phosphodiesterase activity, PC LUVs, PC LUVs with free L-Histidinol, or PC-PtdHisOH LUVs were mixed with pNPP, both with and without Zn^{2+}, as outlined in the methods section 2.3.2.

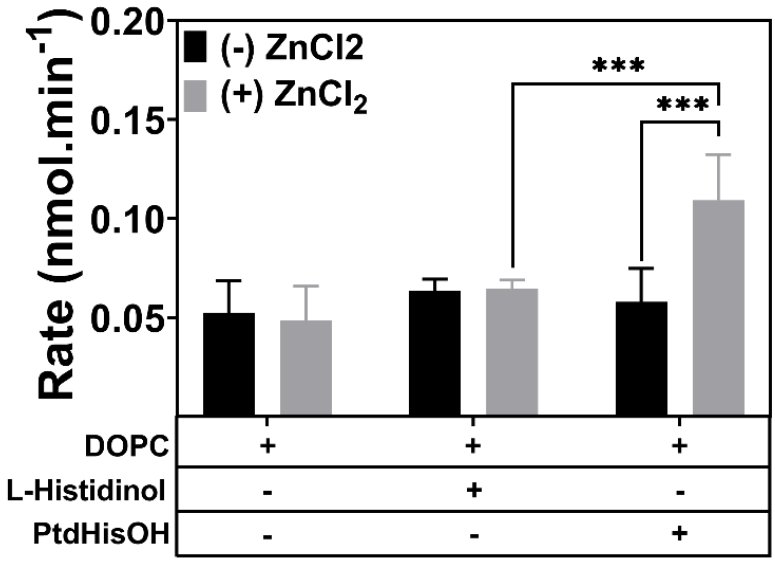


Figure 5.6 – Phosphatase activity of PtdHisOH in LUVs. Phosphatase activity was tested in 100 mol% PC LUVs, 100 mol% PC LUVs with 20 nmols L-Histidinol or 70 mol% PC – 30 mol% PtdHisOH LUVs, incubated without or with 20 nmols of Zn^{2+} at room temperature for 30 minutes. 1 mM pNPP was then added, and catalytic rates were calculated using standard curves. Average of 2 separate experiments with triplicates (n = 6) and SD are shown. The background absorbance has been removed.

Figure 5.6 shows the catalytic rates of pNPP hydrolysis by PtdHisOH LUVs in the presence or absence of Zn^{2+}. Here, the high background issues have been solved, and data is presented as rates.

Considering the findings from previous experiments with BNPP, where an increase in absorbance is attributed to LUVs binding/fusing, two absorbance measurements are

taken for this experiment: $Abs_{405\ nm}$ and $Abs_{600\ nm}$. While $Abs_{600\ nm}$ measures the opacity of the solution, it does not take into account the absorbance for 4-nitrophenol [199]. Therefore, calculating the difference between $Abs_{600\ nm}$ and $Abs_{405\ nm}$ provides a more accurate estimation of the absorbance solely due to hydrolysis. This difference was then converted to rates based on a 4-nitrophenol calibration curve.

This experiment confirms that there is some phosphatase activity in LUVs containing PtdHisOH in the presence of Zn^{2+}. However, the background from the controls is still high due to opaqueness (0.05 nmol.min-1) and the delta with the negative control is relatively low (0.07 $nmol.min^{-1}$).

To enhance sensitivity and mitigate the absorbance issue caused by LUV clustering in the presence of Zn^{2+}, we tested a fluorescent compound for the detection of phosphatase activity. 4-MUP (4-Methylumbelliferyl Phosphate) is a commonly used fluorescent substrate for detecting alkaline phosphatase activity [200, 201]. LUVs were incubated with or without Zn^{2+} for 30 minutes before adding 5 mM 4-MUB and fluorescence was measured overnight at $Ex_{386\ nm}$ and $Em_{448\ nm}$ using a spectrometer. Unfortunately, the results of this experiment were inconclusive as no fluorescence was detected in any samples.

To conclude on the phosphatase activity, PtdHisOH exhibits some low but detectable activity toward pNPP. The issues with high background have been addressed, and the catalytic rates for phosphatase are not high enough to pursue our investigation.

5.1.3. Esterase activity

The catalytic ability of imidazole toward esterases has been reported in literature, as well as the capacity of L-Histidine to hydrolyse ester bonds [162, 187]. These experiments were inspired by the work done by Poznik *et al.*, where they investigated the hydrolysis of esters in the presence of zinc in membrane surfaces, and with membrane additives containing imidazole functional groups [127]. In their work, fluorescein diacetate (FDA) was used as the artificial substrate to detect hydrolysis.

In our study, the PtdHisOH was directly incorporated in the membrane of PC vesicles. 200 nm extruded LUVs were prepared without or with PtdHisOH. Fluorescein diacetate (FDA) was used as the substrate and the detection of the catalysis was measure with a spectrometer at $Abs_{480\,nm}$ and $Em_{520\,nm}$.

The first experiment consists in comparing the esterase activity detected in LUVs containing PC-PtdHisOH. PC LUVs are used as a control, as well as PC LUVs with free L-Histidinol to be able to compare the activity of the alcohol and the activity of the novel lipid. The experiment is carried out without or with Zn^{2+} in parallel, to see how the metal influences the catalysis of FDA by the lipid.

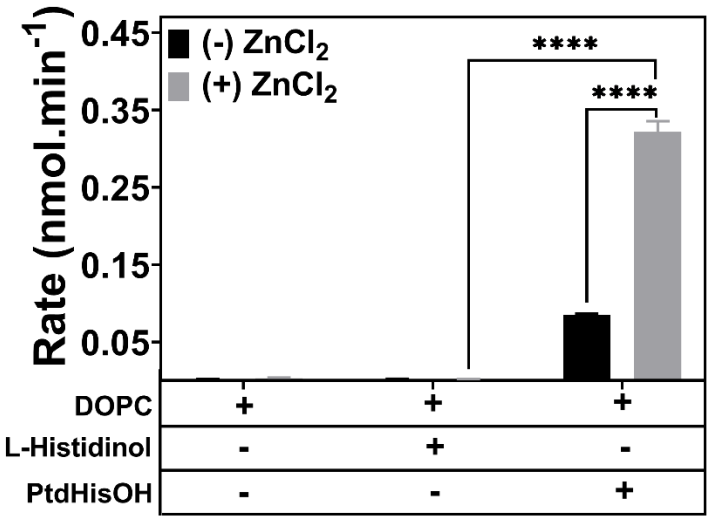


Figure 5.7 – Esterase activity of PtdHisOH in LUVs. Esterase activity was tested in 100 mol% PC LUVs, 100 mol% PC LUVs with 20 nmols L-Histidinol or 70 mol% PC – 30 mol% PtdHisOH LUVs, incubated without or with 20 nmols of Zn^{2+} at room temperature for 30 minutes. 1 mM FDA was then added, and catalytic rates were calculated using standard curves. The time frame to calculate rates was of 500 seconds. Average of 2 separate experiments with triplicates (n = 6) and SD are shown.

Figure 5.7 shows a catalytic rate of almost 0 $nmol.min^{-1}$ for the catalysis of FDA by PC LUVs. The rates are very close to 0 $nmol.min^{-1}$ for the catalysis by PC LUVs in the presence of L-Histidinol. In these conditions, the presence of Zn^{2+} has no impact on the reaction. However, when the LUVs are supplemented with PtdHisOH, the catalytic rates are higher, reaching a rate of 0.1 $nmol.min^{-1}$ in the absence of Zn^{2+} and almost 0.35 $nmol.min^{-1}$ when

Zn^{2+} is added to the reaction. This confirms that the lipid possesses catalytic esterase-like activity, and the presence of Zn^{2+} boosts this activity 3-fold.

Comparing the catalytic rates obtained for phosphodiesterase activity, phosphatase activity and esterase activity, we can conclude that esterase activity is the most active(0.35 $nmol.min^{-1}$), followed by phosphatase activity with a 3-fold decrease in activity (0.1 $nmol.min^{-1}$). Phosphodiesterase exhibits the lowest activity, with rates not exceeding 0.03 $nmol.min^{-1}$).

Moreover, phosphatase and phosphodiesterase experiments were based on absorbance, which have shown some high background due to the intrinsic absorbance of LUVs, particularly in the presence of Zn^{2+}. For these reasons, we decided to focus on the esterase capabilities of our lipid.

5.2. Esterase activity

5.2.1. Lipid presentation

After confirming in Figure 5.7 that the presence of Zn^{2+} enhances esterase activity within the LUV system, we opted to explore alternative lipid presentations to determine in which conditions the lipid was most catalytic.

For this experiment, lipids were presented either in the 2-phase system (used for lipid synthesis), in the coated system (used for the optimisation of the synthesis), in a micellar system with octyl glucoside (OG) or in 200 nm extruded LUVs.

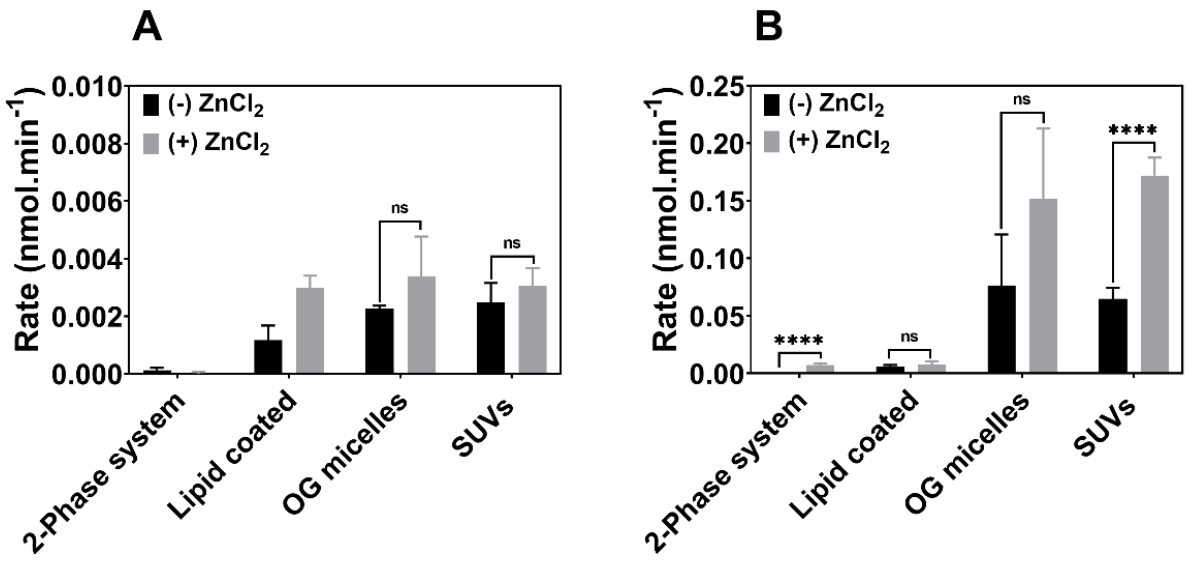


*Figure 5.8 – Effect of lipid presentation on Zn^{2+}-dependent esterase activity. Lipids were presented in four different ways: 2-phase system (buffer/chloroform), coated system in a 96-well plate), micelles (with Octyl glucoside) or LUVs (200 µm diameter). PC alone was employed for the controls (**A**) and PC supplemented with 30 mol% PtdHisOH was employed in (**B**). Reactions were incubated without Zn^{2+} (**black**) or with 20 nmols Zn^{2+} (**grey**). Lipids and metals were incubated for 30 minutes at room temperature before adding 1 mM FDA. The reactions were monitored by fluorescence and initial rates calculated using standard curves. Average of 2 separate experiments with triplicates (n = 6) and SD are shown.*

Figure 5.8 shows the catalytic rates for esterase activities with PC or PtdHisOH presented in different systems, both without and with the presence of Zn^{2+}. In the controls containing PC only (Figure 8 A), no significant difference is observed between (-) Zn^{2+} and (+) Zn^{2+} in any of the four systems tested. The rates are consistently low, ranging from 0 nmols.min^{-1} in the 2-phase system, to 0.003 nmols.min^{-1} on average in the coated system, OG micelles and LUVs.

In Figure 8B, both the 2-phase system and the lipid-coated system exhibit the lowest rates, measured at 0.01 nmols.min^{-1}. While the 2-phase system shows a significant increase upon the addition of Zn^{2+}, the lipid-coated system demonstrates no difference in rates between samples with and without Zn^{2+}. Compared to the rates observed with PtdHisOH, the rates with PC are at least 20 times lower, and can therefore be considered as background fluorescence.

Presenting PtdHisOH in OG micelles or LUVs results in higher catalytic rates, which are significantly enhanced by the presence of Zn^{2+}. OG micelles exhibit a catalytic rate of 0.08 nmol.min^{-1} and a 1.8-fold increase in the presence of Zn^{2+}, reaching a rate of 0.15

nmol.min^{-1}. Similarly, LUVs display a catalytic rate of 0.06 nmol.min^{-1}, which is boosted to 0.18 nmol.min^{-1} in the presence of Zn^{2+}, indicating a 3-fold increase in rate. It is worth noting that the OG micelles exhibit a higher error compared to the LUVs.

These results confirm that the catalysis of PtdHisOH is indeed boosted by the presence of Zn^{2+}. Furthermore, the observed differences in catalytic rates across various lipid presentations suggests that the catalysis is influenced by the surface curvature of these lipid environments. These results are very positive as they show the formation of catalytic vesicles that could easily be applied for further applications in artificial cells (discussed in chapter 6).

LUVs and micelles, being small in particle size, present a distinct surface curvature compared to the other systems. Lipid presentation as LUVs (in the nanometre range) yields the highest catalytic rates, followed by OG micelles, which have an even smaller particle size [202].

In contrast, neither the coated lipid system nor the 2-phase system exhibits catalytic activity. The coated lipid system features a flat layer with no curvature, while the 2-phase system consists of relatively large droplets (in the micrometre range) [203]. The curvature in the 2-phase system is so low that the system would also appear as a flat surface.

In conclusion, the data indicates a correlation between the zinc-dependent catalytic activity of PtdHisOH and its presentation. Specifically, the catalytic activity appears to be influenced by the curvature of the membrane.

5.2.2. Variation of PtdHisOH amounts

In this experiment, we investigate the impact of varying amounts of PtdHisOH on esterase catalytic rates. The experiment focuses on the two most effective systems, LUVs and OG micelles, prepared with increasing amounts of PtdHisOH ranging from 0 mol% to 30 mol%, with the remainder composed of PC. As a control, PE was utilized due to its structural similarity to PtdHisOH, particularly regarding the presence of the amine functionality in the headgroup.

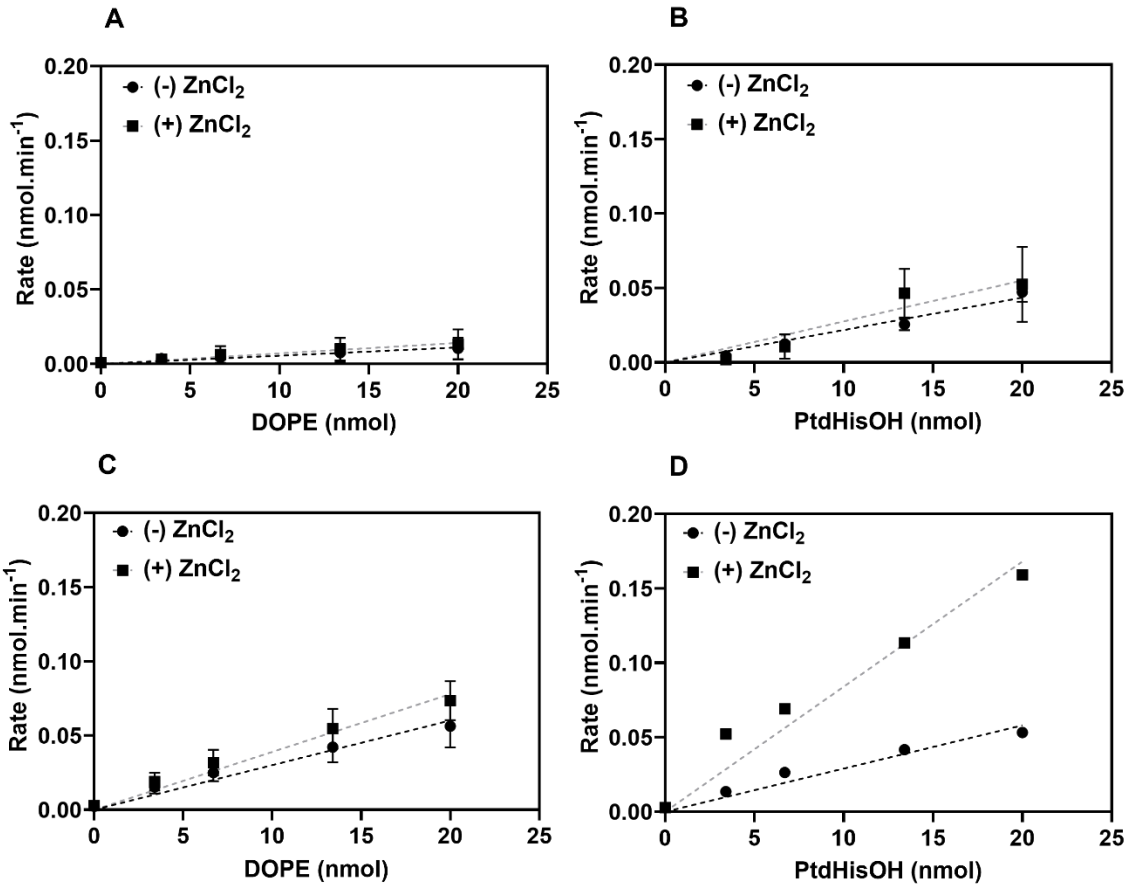


*Figure 5.9 – Esterase rates correlate with lipid amounts in micelles or LUVs. PE or PtdHisOH were presented with PC in octyl glucoside micelles or extruded LUVs using increasing amounts of lipid as indicated. (**A**) PC-PE micelles (0 - 30 mol% PE), (**B**) PC-PtdHisOH micelles (0 – 30 mol%), (**C**) PC-PE LUVs (0 - 30 mol% PE), (**D**) PC-PtdHisOH LUVs (0 – 30 mol%). Micelles or LUVs were incubated at room temperature for 30 minutes without or with Zn^2, before adding 1 mM FDA. Esterase activity was detected by fluorescence and initial rates calculated using standard curves. The background fluorescence has been deducted in this data set. Average of 2 separate experiments with triplicates (n = 6) and SD are shown.*

In Figure 5.9, the controls illustrate the catalytic rates of PE micelles (A) and PE LUVs (C). In PE micelles, the catalytic rates are observed to be close to 0 and increase slightly with the concentration of PE, though without statistical significance. In contrast, PE LUVs demonstrate a linear increase in esterase activity correlated with increasing amounts of PE, reaching a rate of 0.075 nmol.min^{-1} at the highest PE concentration, regardless of the presence of Zn^{2+}. Notably, there is no significant enhancement in activity in the presence of Zn^{2+}.

Figure 9B illustrates the linear increase in catalytic rates of PtdHisOH micelles, reaching 0.05 nmol.min^{-1} for the highest PtdHisOH concentration, regardless of the presence of

Zn^{2+}. Compared to the PE controls, PtdHisOH micelles have higher catalytic rates than PE micelles, and similar rates to PE LUVs.

Furthermore, figure 9D presents the catalytic rates for PtdHisOH LUVs. Once again, the rates increase linearly with PtdHisOH concentration, but the presence of Zn^{2+} results in a 3-fold boost to the catalytic activity. Catalytic rates reach 0.05 $nmol.min^{-1}$ for PtdHisOH LUVs, and more than 0.15 $nmol.min^{-1}$ in the presence of Zn^{2+}.

These results confirm the zinc-dependent esterase activity in PtdHisOH LUVs. Comparing the activity with the PE LUVs control, it becomes evident that the zinc-related catalytic properties observed are closely linked to the imidazole compound present in the headgroup of the PtdHisOH lipid. Imidazole has been demonstrated in numerous studies to form complexes with Zn^{2+}, likely accounting for the observed catalytic effects detected [156, 204, 205].

Furthermore, the observation of activity in the LUV system for PE suggests that the amino group present in both PE and PtdHisOH may contribute to the observed activity to some extent.

Finally, the significantly higher activity observed in PtdHisOH LUVs with Zn^{2+} compared to PtdHisOH micelles with Zn^{2+} suggests that particle size, and therefore the curvature of LUVs, could be a factor influencing esterase activity.

5.2.3. Effect of Zn^{2+} on PtdHisOH LUVs

Drawing from previous experiments indicating the significance of particle size and of the crucial role of the imidazole/Zn^{2+} interaction on esterase activity, we opted to explore the effects of Zn^{2+} on the particle size of PtdHisOH LUVs.

We have established from prior experiments (chapter 4) that PtdHisOH lipids for complexes with Zn^{2+}, causing LUVs to cluster and merge. The objective here is to explore the correlation between the augmentation in PtdHisOH concentration within LUVs and the resulting alteration in particle size.

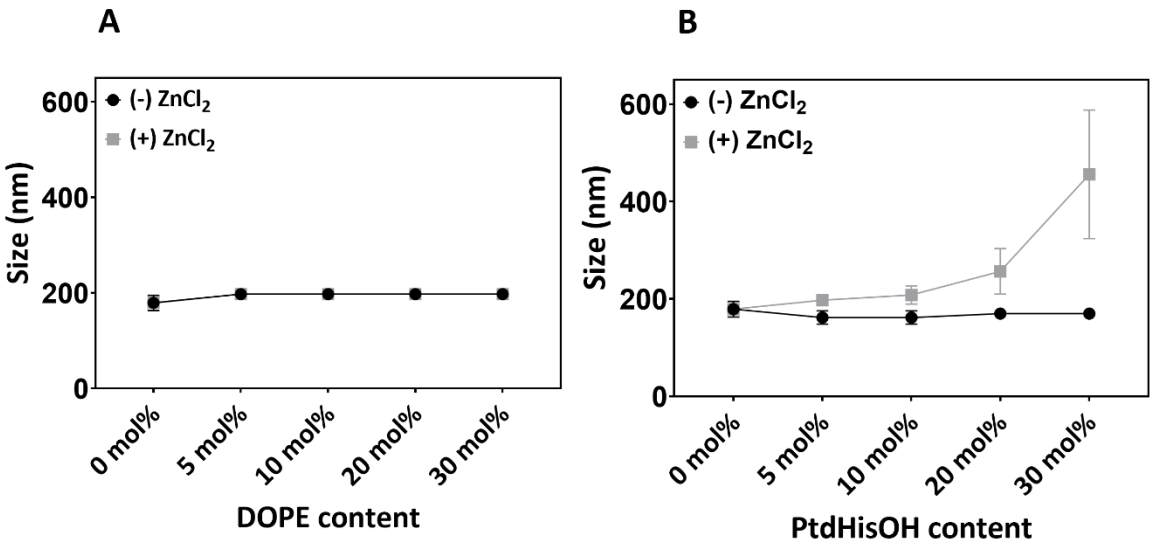


*Figure 5.10 – Particle size dynamics of LUVs with gradient PE or PtdHisOH. PE or PtdHisOH were presented with PC in LUVs using increasing amounts of lipid as indicated (**A**) PC-PE LUVs (0 - 30 mol% PE), (**B**) PC-PtdHisOH LUVs (0 – 30 mol%). LUVs were made by extrusion using 200 nm filters and were incubated for 30 minutes with or without 20 nmols Zn^{2+}. Particle sizes were measured using a particle sizer (Zetasizer) in a UV disposable cuvette. Data points in this graph represent the peaks for each size distribution curve generated. Average of 3 separate experiments (n = 3) and SD are shown.*

In the control featuring PE LUVs (Figure 10A), the size of PE LUVs is measured at nearly 200 nm and remains constant with the increase in PE concentration. Additionally, the size is not affected by the presence of Zn^{2+} at the tested molar ratios.

In Figure 5.10-A, the size of PtdHisOH LUVs without Zn^{2+} fluctuates between 160 nm and 180 nm, remaining relatively constant with increasing concentrations of PtdHisOH. In contrast, in the presence of Zn^{2+}, PtdHisOH LUVs exhibit a non-linear increase in size with increasing concentrations of PtdHisOH. The size increase between 0 mol% and 10 mol% PtdHisOH is minimal, rising from 180 nm to 200 nm. At 20 mol% PtdHisOH, the size of LUVs increases by 25%, reaching 250 nm and with 30 mol% PtdHisOH, the size increases by 75%, averaging more than 430 nm. The abrupt rise in particle size observed in the presence of Zn^{2+} at 20 mol% PtdHisOH could be attributed to the density of PtdHisOH at the surface of LUVs. At lower densities (5 mol% and 10 mol%), there is less binding of Zn^{2+} compared to when concentrations of PtdHisOH are higher. This correlates with the binding experiments showing that a certain density of PtdHisOH is needed to achieve Zn^{2+}

chelation (Figure 4.9 - chapter 4). This increase in particle size in the presence of Zn^{2+} will be further investigated in Chapter 6.

5.2.4. Zn^{2+} dependency of the esterase activity

The experiment described in Figure 5.9, where PtdHisOH molar ratios in LUVs were increased while maintaining a constant Zn^{2+} concentration, may have led to alterations in the equimolar ratios of PtdHisOH/Zn^{2+}. In LUVs with higher PtdHisOH molar ratios, Zn^{2+} could potentially become depleted, resulting in some PtdHisOH remaining free.
To address this concern, we examined the impact of increasing Zn^{2+} concentrations on catalytic rates while maintaining the molar ratio of PtdHisOH or PE at 30 mol%, as this ratio yielded the highest rate.

5.2.4.1. Ratio lipid : Zn^{2+}

In order to determine the optimal conditions for the catalytic activity of PtdHisOH, we experimented with various concentrations of Zn^{2+} while maintaining a fixed concentration of PtdHisOH in LUVs only, as they exhibited the best catalytic rates. As controls, PC and PC-PE LUVs were employed.

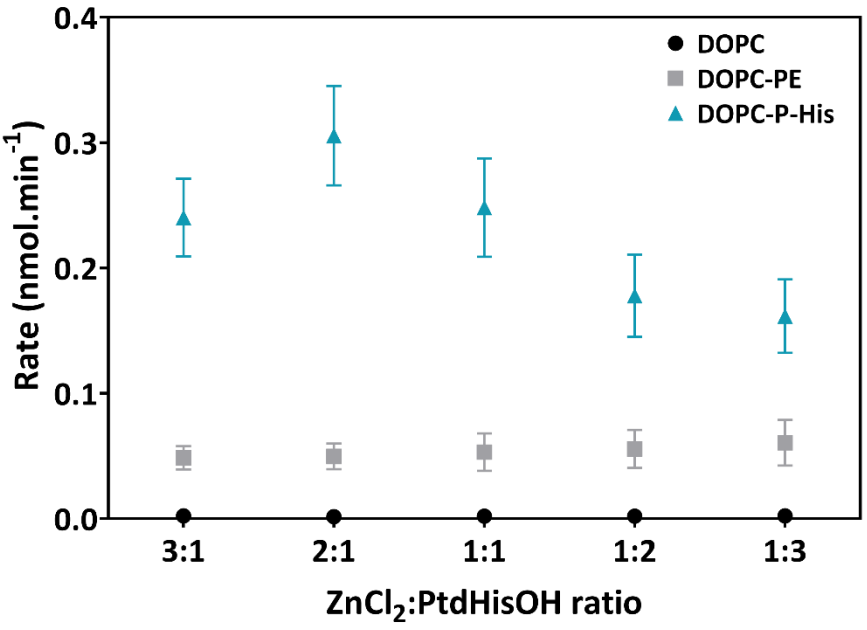


Figure 5.11 – Optimal Zn^{2+}/PtdHisOH ratios for esterase activity of PtdHisOH lipid in LUVs. LUVs containing either 100 mol% PC, 70 mol% PC – 30 mol% PE or 70 mol% PC – 30 mol% PtdHisOH were incubated at room temperature for 30 minutes with the indicated concentrations of Zn^{2+} before adding 1 mM FDA. The reactions were monitored by fluorescence and initial rates calculated using standard curves. Average of 2 separate experiments with triplicates (n = 6) and SD are shown.

The data presented in Figure 5. 11 shows no catalytic rates for PC LUVs, regardless of the Zn^{2+} concentration. Similarly, the PE control shows a constant catalytic rate around 0.04 nmols.min^{-1}. Regarding PtdHisOH LUVs, the optimal Zn^{2+}/PtdHisOH ratio seems to be two Zn^{2+} per one PtdHisOH lipid (2:1). The lowest catalytic rates are observed for a ratio of 3:1 Zn^{2+} to PtdHisOH, with a 2-fold decrease from the optimum. The drop in catalytic activity is surprisingly low, given that the catalysis is driven by Zn^{2+}, and there is 6 times less zinc in the 3:1 ratio compared to 2:1 ratio.

This data suggests that 1:3 Zn^{2+}/PtdHisOH is enough to detect catalytic activity, with the excess of Zn^{2+} increasing the number of complexes formed. However, the observed linear increase in Zn^{2+} concentration did not result in a proportional increase in catalytic rate. This discrepancy suggests a potential contribution of amine groups in PtdHisOH to binding of Zn^{2+}, which could explain the formation of an active complex with only two PtdHisOH molecules.

5.2.4.2. Metal selectivity

Given that Zn^{2+} has consistently demonstrated the ability to enhance catalytic rates for esterase activity in previous experiments involving PtdHisOH, we sought to confirm whether this enhancement is specifically attributed to the metal ion itself rather than its charge. To address this, we examined the impact of other bivalent metals on esterase activity and their potential to substitute Zn^{2+}. $ZnCl_2$, $CoCl_2$ and $CuCl_2$ were tested with LUVs. $CaCl_2$, which has not been reported as a cofactor of any esterase, was also tested.

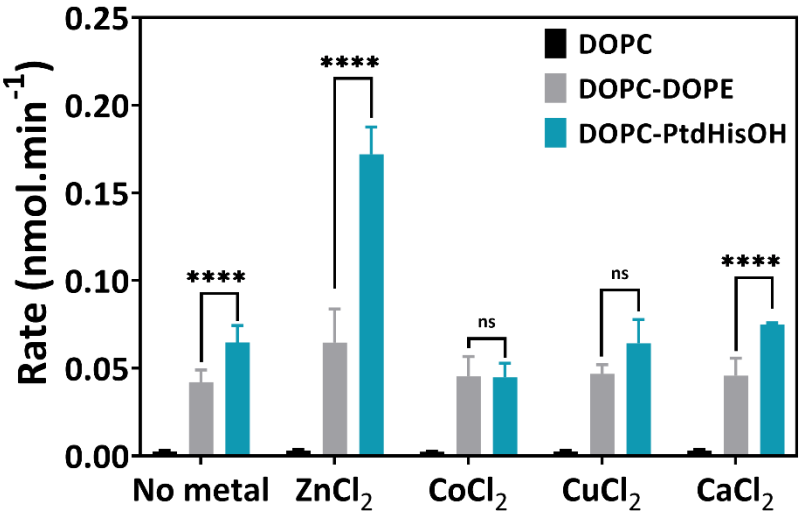


Figure 5.12 – Metal selectivity of PtdHisOH esterase activity in micelles or LUVs. LUVs were incubated with 20 nmols of the indicated metal ion for 30 minutes at room temperature, before addition of 1 mM FDA. Esterase activity was detected by fluorescence and calculated based on standard curves. Average of 2 separate experiments with triplicates (n = 6) and SD are shown.

In Figure 5.12, PC LUVs exhibit no catalytic activity regardless of the added metal, consistent with previous observations. PC-PE LUVs display some catalytic activity that remains relatively constant across different metals, hovering around 0.05 $nmol.min^{-1}$, with a slight enhancement in the presence of Zn^{2+}. For PC-PtdHisOH LUVs, the catalytic activity is measured at 0.06 $nmol.min^{-1}$ in the absence of metal and with Ca^{2+}. There is a marginal decrease in activity in the presence of Co^{2+} and Cu^{2+}, while a significant increase is observed in the presence of Zn^{2+}, with a 2.8-fold increase compared to no metal. These results affirm that Zn^{2+} is significantly superior as a catalyst, consistent with existing literature.

These results demonstrate the specificity of PtdHisOH esterase activity to Zn^{2+}, as evidenced by the lack of boost in catalytic rates with other metals such as Co^{2+} and Cu^{2+}, despite their known interactions with the imidazole group [206, 207].

Additionally, the size of PC, PC-PE and PC-PtdHisOH LUVs in the presence of different bivalent metals were measured.

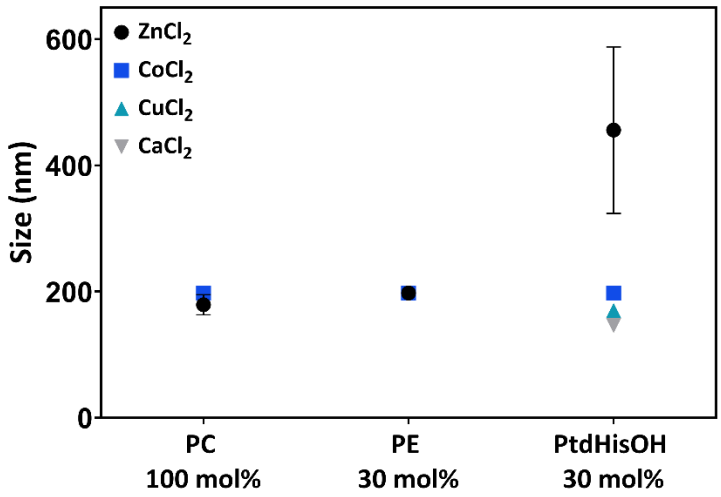


Figure 5.13 – Effect of different metal ions on the size of LUVs. LUVs used in the experiment from Figure 11 were incubated with 20 nmols of the indicated metal ion at room temperature and for 30 minutes. The LUVs were measured using a particle sizer (Zetasizer) in a UV diposable cuvette. Particle sizes were measured using a particle sizer (Zetasizer) in a UV disposable cuvette. Data points in this graph represent the peaks for each size distribution curve generated. Average of 2 separate experiments (n = 2) and SD are shown.

Figure 5.13 illustrates that only PC-PtdHisOH LUVs exhibit an increase in size, suggesting a clustering of LUVs as observed previously. In contrast, the other metal ions have no significant impact on the size of PtdHisOH. PC and PC-PE LUVs remain unaffected by any metal ions, maintaining a consistent size of 200 nm.

5.3. Conclusions & future work

In conclusion, the PtdHisOH lipid exhibits both esterase-like and phosphatase-like properties, with esterase activity being predominant.

Our investigation into esterase activity revealed that surface curvature and lipid density play pivotal roles in catalysis, with the 200 nm extruded LUVs demonstrating the highest catalytic rates. Moreover, the results underscore the strong dependence of catalysis on Zn^{2+}, aligning with existing literature on histidine catalysis.

These findings open new perspectives for leveraging PtdHisOH in artificial cell applications, a topic that will be explored in Chapter 6.

6. Chapter 6: Application of PtdHisOH to the Artificial Cell technology

The PtdHisOH lipid has exhibited intriguing properties, including its capability to bind his-tagged proteins in the coated system and its catalytic properties towards esters. These characteristics make the lipid a promising candidate for applications in artificial cells, serving as a novel tool for vesicle functionalization.

Incorporated into vesicles, this lipid holds potential applications in the biomedical field. It could be utilized for protein-lipid binding to target specific sites, for lipid-lipid binding to create networks of vesicles, or for its catalytic properties to establish microreactors capable of activating drugs in situ. The aim of this chapter is to explore initial possible concepts, that would provide insight into possible approaches to enhance artificial cell functionality.

6.1. Incorporation of the PtdHisOH lipid into the membrane of artificial cells

6.1.1. Characterisation and stability of LUVs with PtdHisOH

The data presented in Figure 5.10 (chapter 5) demonstrates that LUVs can be generated, using PC and PtdHisOH via extrusion. LUVs measuring just under 200 nm can be produced, the size remaining constant regardless of the mol% of PtdHisOH present in the membrane (up to 30 mol%).

The stability of LUVs containing 30 mol% PtdHisOH was tested by measuring the size distribution of a sample over time. Given that the primary reason to use vesicles in PtdHisOH experiments is curvature, we based stability experiments on the premise that if the size distribution remains unchanged, vesicles are not undergoing collapse.

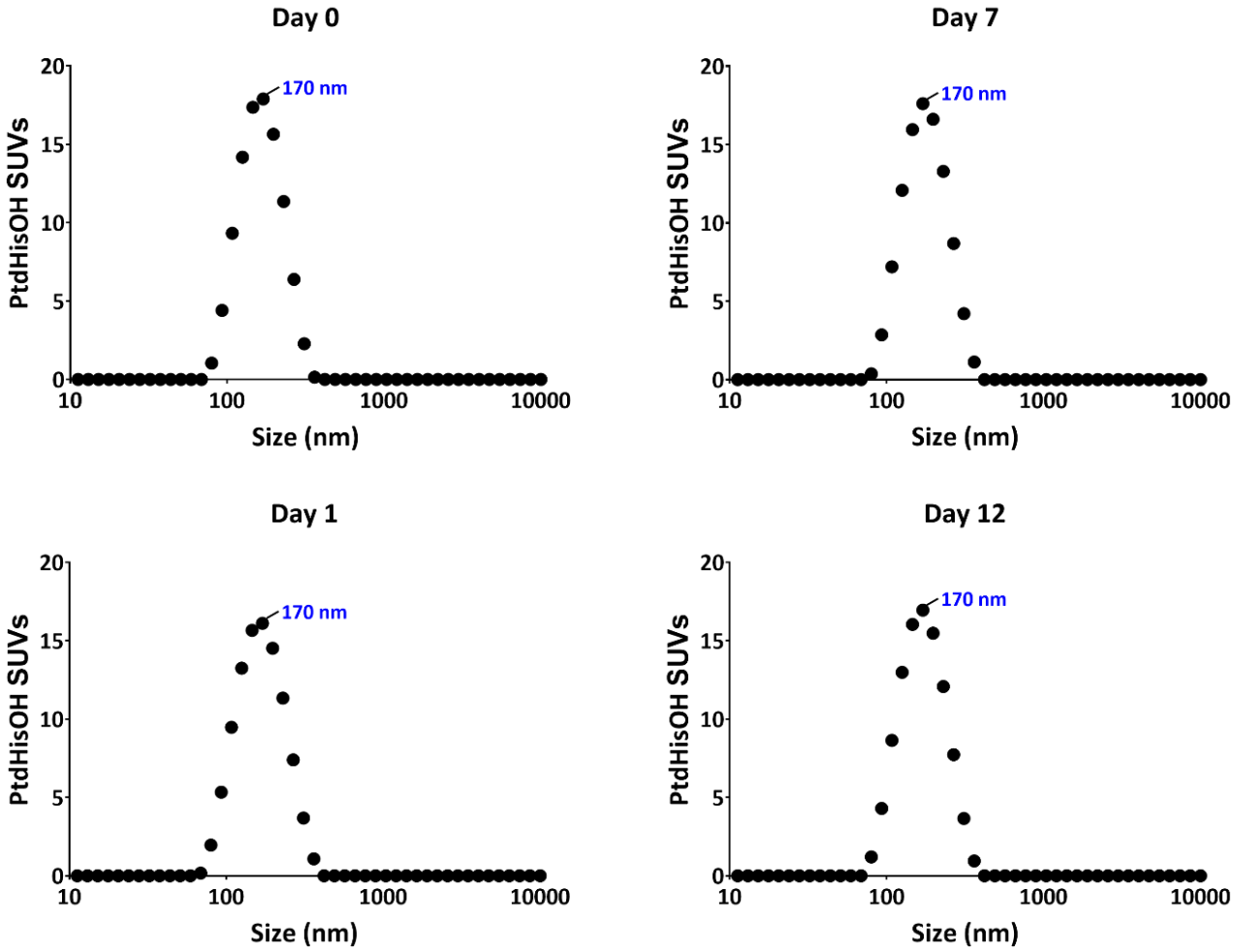


Figure 6.1 – Size distribution of the same sample of LUVs over time. LUVs with 70 mol% PC-30 mol% PtdHisOH were extruded using a 200 nm membrane in HEPES buffer pH 7.4. The size distribution of the sample was measured on days 0, 1, 7 and 12 using a DLS. Samples were stored at 4°C in between measurements LUVs were made using standard procedures detailed Methods – section 2.4.2.

Figure 6.1 shows that the size distribution stays consistent over the monitored period of 12 days. When stored at 4°C, the size of PtdHisOH LUVs is stable over time. For all subsequent experiments, LUVs were either employed immediately after preparation or stored for a maximum of 2 days at 4°C before use.

6.1.2. Lipid distribution in PtdHisOH LUVs

The additional imidazole moiety in the PtdHisOH could cause a preference for an asymmetric distribution between the inner and outer leaflets of the vesicular membrane. It cannot be ruled out that the bigger headgroup would favour a convex curvature therefore it was necessary to elucidate the distribution of PtdHisOH lipid within the bilayer of PtdHisOH-PC LUVs.

To achieve this, the amount of free amino functionalities located on the PtdHisOH headgroup was determined by exposing LUVs to fluorescamine. As explained earlier, fluorescamine becomes fluorescent when exposed to primary amines, and based on a calibration curve, the amount of lipid can be calculated. To distinguish between the outer leaflet and inner leaflet two conditions of exposure were applied: firstly, fluorescamine was presented in aqueous buffer for the detection of PtdHisOH in the outer membrane only, secondly fluorescamine was presented in acetone for the total PtdHisOH measurement. Among other organic solvents, acetone has shown to dissolve lipid membranes, and is often employed in fluorescamine assays [1, 2]. The same experiment was done using PtdHisOH presented in micelles as a control (Figure 6.2 – A). In micelles, all the lipid head groups will be exposed and accessible for detection, so similar amounts of lipid are expected in both dissolved (acetone treated) or undissolved (aqueous buffer) conditions. PC was employed as a negative control, PE/PC as a positive control.

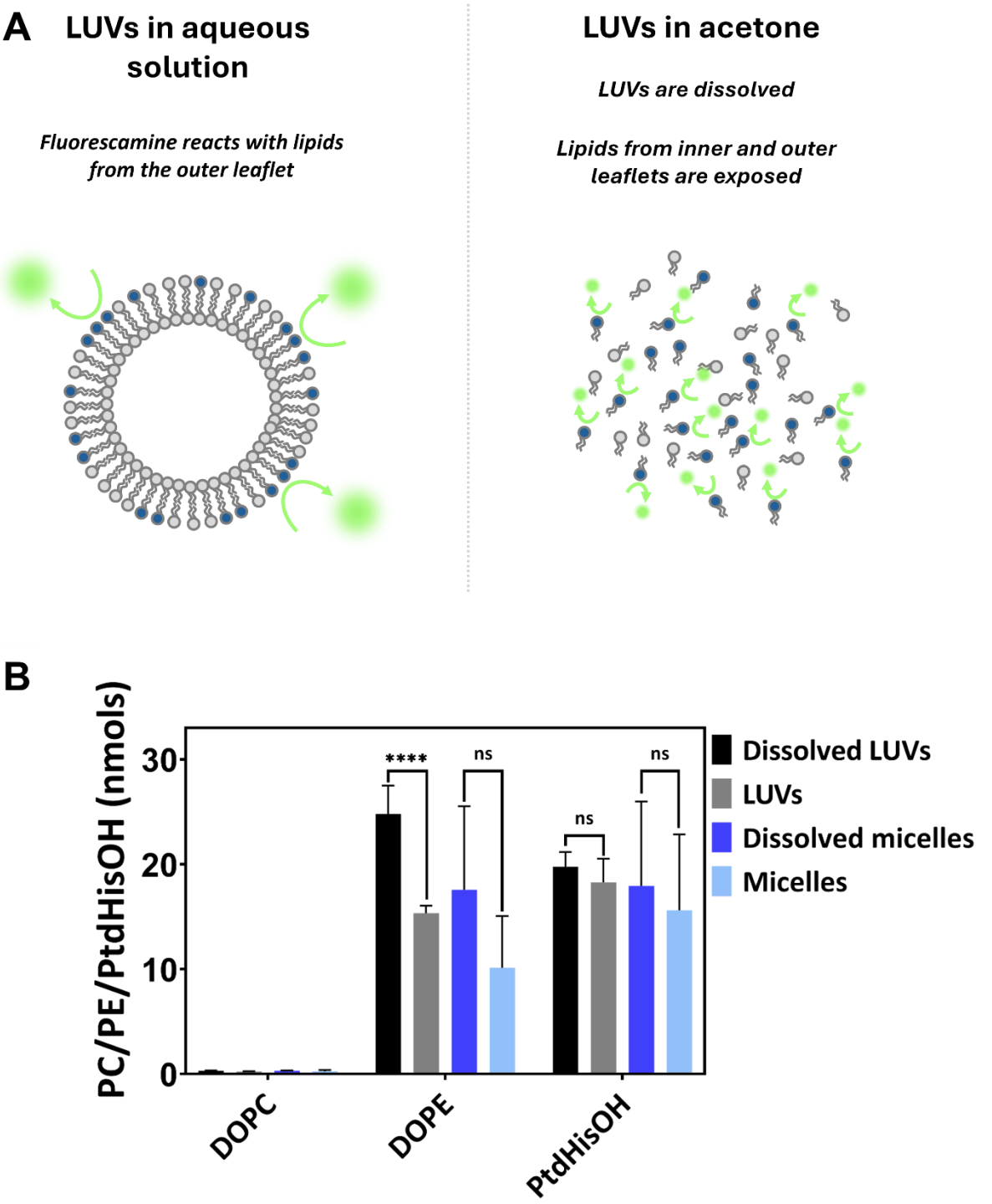


Figure 6.2 – (A) Schematic representation of the experiment: fluorescamine reaction of lipids incorporated into SUV membranes or lipids dissolved into the solvent. (B) PtdHisOH distribution in the LUV bilayer. LUVs composed of 100 mol% PC, 70 mol% PC-30 mol% PE, or 70 mol% PC-30 mol% PtdHisOH are prepared by extrusion using a 200 nm filter. OG micelles with the same compositions are made by sonication. Each LUV or micelle sample (50 µL) is supplemented with fluorescamine either in 50 µL of buffer (pH 7.4), or 50 µL of acetone (dissolved micelles or LUVs), resulting in a final fluorescamine concentration of 2.5 mM. The kinetics of the reaction are monitored at Ex420nm/Em480nm. Lipid quantities are calculated using the PE or PtdHisOH calibration curve with fluorescamine as described in section 2.2.3. Data represents the mean and standard deviation shown as error of n = 9 replicates.

In Figure 6.2 - B, the experiment demonstrates that for both LUVs and micelles, whether in buffer or 50% acetone, there are no detectable free amino functionalities in PC samples, validating the negative control.

In the case of PC-PE LUVs, there is a significant difference in the amount of PE detected in the dissolved and undissolved LUVs. This suggests that approximately 2/3 of the PE is distributed in the outer membrane of LUVs, while 1/3 is distributed in the inner layer of the membrane. This result makes sense, as the outer layer typically has a larger surface area compared to the inner layer due to curvature.

For PE micelles, it is expected to detect the same value for both acetone and buffer, as micelles are formed of one lipid layer and dissolving them will not increase the number of exposed lipids. Here, there is a difference observed between the samples dissolved and the untreated samples. However, the difference is not significant: the discrepancy may be attributed to the large error bars observed.

In the case of PC-PtdHisOH LUVs, similar amounts of PtdHisOH are detected for both treated and untreated samples. The non-significant difference suggests that there is no difference between the total and the outer layer PtdHisOH content. Hence, 90% to 100% of PtdHisOH is located in the outer membrane of LUVs, resulting in a distinctly asymmetric LUV membrane. In PtdHisOH micelles, similar amounts of amino functionalities are detected in both acetone and buffer, consistent with expectations, but again with large error bars.

6.2. Applying the lipid-metal affinity to attract vesicles together

Previous results have revealed that PtdHisOH binds metal ions, particularly Zn^{2+} and Cu^{2+}, when the PtdHisOH density is high enough (Figure 4.6, Chapter 4). Based on the literature, two histidines can form a complex through coordination bonds with a transition metal ion [89]. This allows us to hypothesise that two PtdHisOH lipids from two distinct vesicles can bind together, establishing a cell-cell contact.

6.2.1. Size distribution of PtdHisOH LUVs in the presence of metal ions

To investigate whether lipid-lipid interactions such as binding or fusion can be achieved, the stability of LUVs and their behaviours when exposed to metal ions were monitored through size distribution analysis, under various pH conditions.

200 nm PC or PtdHisOH LUVs were prepared via extrusion and subsequently incubated with Zn^{2+} in buffers ranging from acidic (pH 5) to neutral (pH 7) and alkaline (pH 8.5). The size of the LUVs was then assessed using a Zetasizer instrument. For reference, the size of LUVs without Zn^{2+} is shown in Figure 6.1.

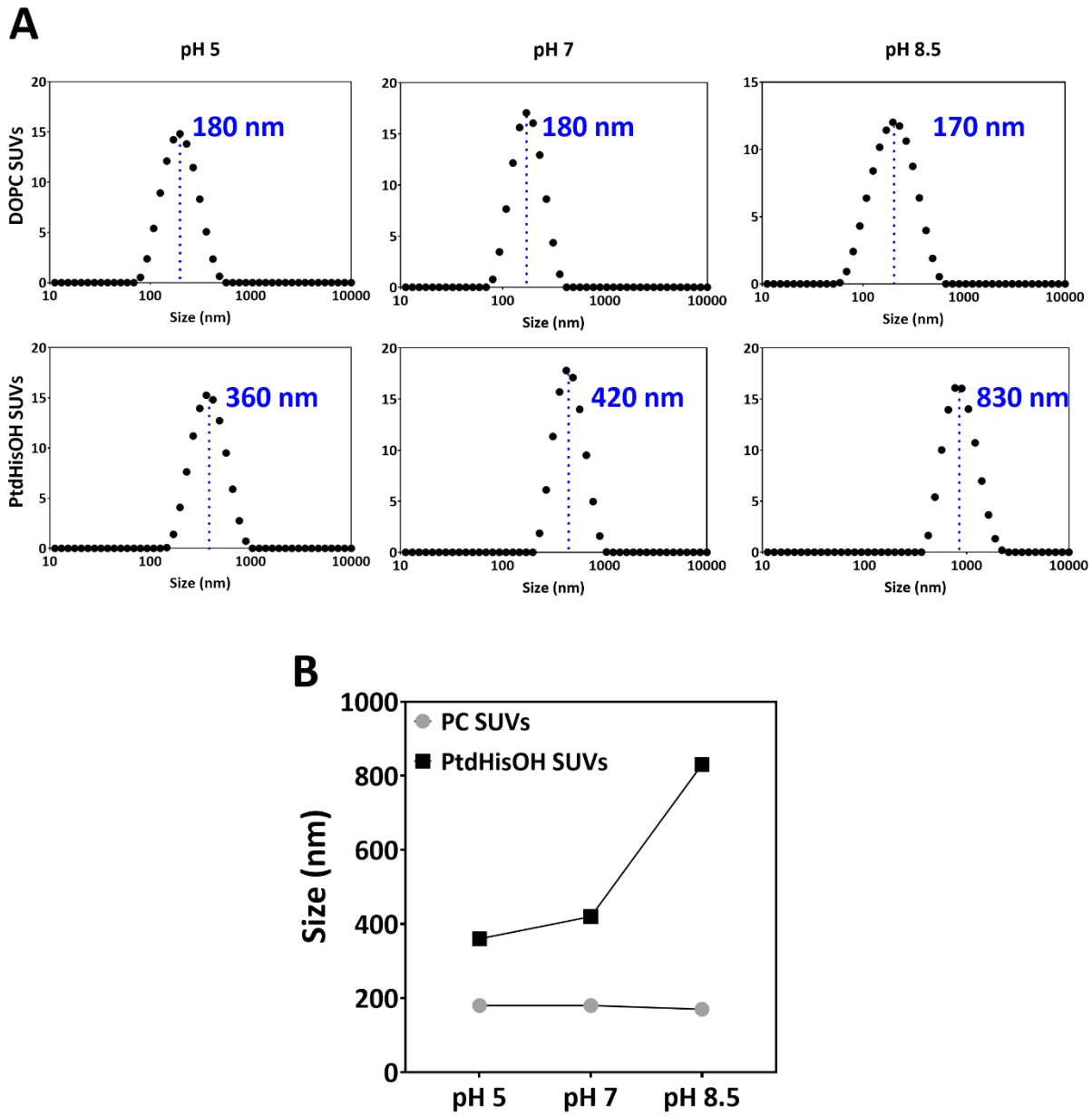


*Figure 6.3 – Impact of Zn^{2+} on particle size at different pH. PC 100 mol% or PC 70 mol% - PtdHisOH 30 mol% LUVs are made by extrusion using 200 nm filters and were incubated for 30 minutes with 20 nmol Zn^{2+} at pH 5, pH 7 or pH 8.5. The size distribution is shown in (**A**) and the change in the peak size is shown in (**B**). Particle sizes are measured using a particle sizer (Zetasizer) in a UV disposable cuvette. The graphs represent the size distribution curve generated. Average of 2 separate experiments (n = 2) is shown.*

Figure 6.3 illustrates a consistent size of PC LUVs, regardless of the pH in the presence of Zn^{2+}. The peak size for PC LUVs remains approximately 180 nm, with a slightly smaller size detected (170 nm) at pH 8.5.

For PtdHisOH LUVs, at pH 5, the size is measured at 360 nm, with the size increasing at neutral pH (420 nm) and even further at alkaline pH (830 nm). These results suggest that alkaline conditions promote LUV-LUV aggregation or fusion, while acidic conditions slow down LUV-LUV interactions. The increase in size at alkaline pH can be attributed to the PtdHisOH's pKa being around 7.5, leading to an increased negative charge on the lipid and enhanced metal chelation [208].

6.2.2. Investigating the increase in size of LUVs

6.2.2.1. Reversing LUVs to their original size

To discriminate between the clustering or fusion of LUVs together, a series of experiments were performed. The first step is to induce the clustering or fusion of LUVs using Zn^{2+} to observe an increase in size. Subsequently, a potent chelating agent, ethylenediaminetetraacetic acid (EDTA), is introduced to capture the Zn^{2+} ions and assess the change in size of LUVs. If the LUVs revert to their original size, it indicates that the binding of LUVs together is reversible and therefore, the increase in size in the presence of Zn^{2+} corresponds to clustering. Conversely, if they do not return to their original size, it suggests that the LUVs fuse together to form larger structures.

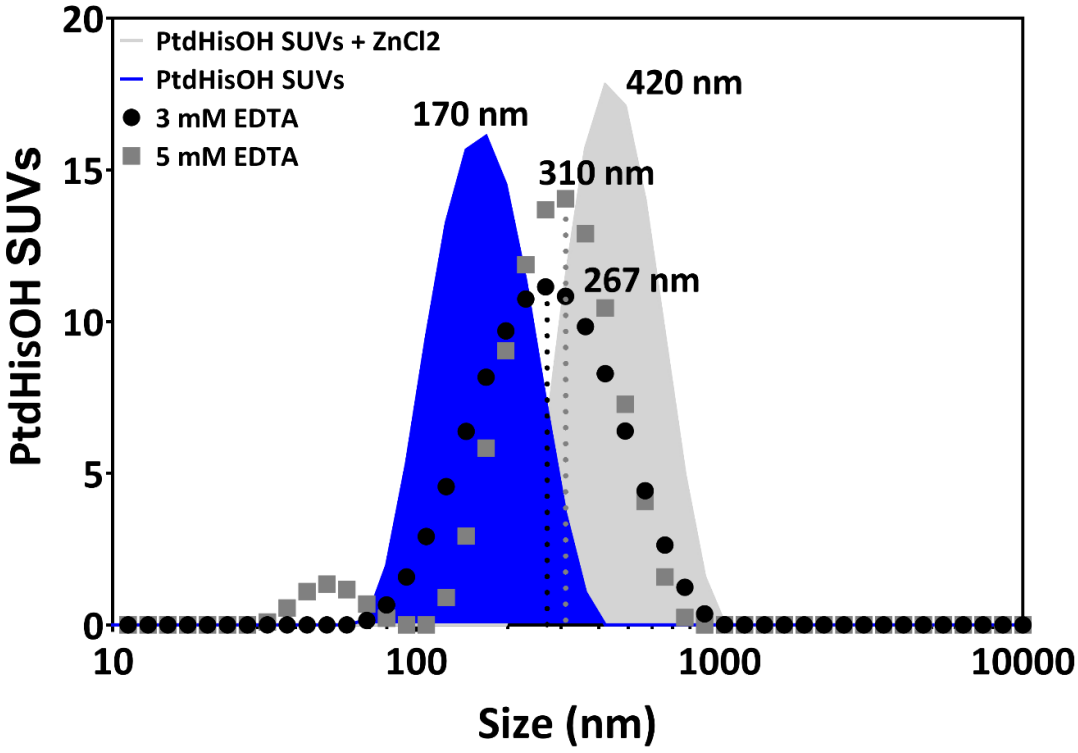


Figure 6.4 – Investigating the size increase of LUVs in the presence of Zn^{2+}. PC 70 mol%-PtdHisOH 30 mol% LUVs are incubated with 20 nmol of Zn^{2+} for 30 minutes at pH 7. 3 mM or 5 mM EDTA are then added to the samples. Particle sizes are measured using a particle sizer (Zetasizer) in a UV disposable cuvette. The graphs represent the size distribution curve generated. For reference, the size of PtdHisOH LUVs incubated with Zn^{2+} (grey curve) was extracted from Figure 6.2. Average of 2 separate experiments (n = 2) is shown.

Figure 6.4 shows the original size of LUVs (in blue) measured before incorporating Zn^{2+}. The average size of LUVs is observed to be 170 nm. The grey curve shows the size of LUVs in the presence of Zn^{2+} at pH 7 whose diameter was 420 nm. Upon adding an excess of EDTA (3 mM and 5 mM), the size reduces to an average of 300 nm. These findings indicates that the LUVs do not revert to their original size closer to 170 nm, but a partial collapse is observed. The data suggest that LUVs are fusing but an alternative method is needed to validate this hypothesis.

6.2.2.2. Lipid-mixing assay for membrane fusion

A Förster resonance energy transfer (FRET) assay was developed based on previous research on fusion between vesicular systems [209-211], to confirm the fusion of PtdHisOH LUVs in the presence of Zn^{2+}. A pair of fluorophore-lipid conjugates (PE-Rhodamine B and PE-NBD) are incorporated in the membrane of PtdHisOH-PC LUVs. It is

expected that the two fluorophore lipids are sufficiently close to each other (< 5nm) for the FRET to be effective. Upon excitation of the donor fluorophore PE-NBD ($Ex_{467\ nm}/Em_{539\ nm}$), it is expected to detect the emission fluorescence of the acceptor PE-Rh B ($Ex_{560\ nm}/Em_{585\ nm}$) [212]. Generally, a distance of 5 nm or less is required for efficient FRET.

The experiment involves two populations of LUVs: population 1 is composed of PtdHisOH LUVs with the fluorescent lipids (PE-NBD and PE-Rhd B), and population 2 is composed of PtdHisOH LUVs without fluorescent lipids. When the two populations of LUVs are mixed together in the presence of Zn^{2+}, the fluorescence is expected to stay the same if there is no fusion (Figure 6.5). If fusion occurs, lipids will diffuse quickly (± 1 $\mu m^2.s^{-1}$), increasing the distance between the donor and acceptor lipid fluorophores [213]. A decrease in the acceptor's emission fluorescence is expected, as well as an increase in the donor's emission fluorescence.

In this experiment, the fluorescence and the size of the particles will be measured using flow cytometry. Regarding the fluorescence, the samples will be excited at the excitation wavelength of the donor ($Ex_{467\ nm}$), and fluorescence readings will be measured at the donor's emission wavelength ($Em_{539\ nm}$). Therefore, we will look at the donors' fluorescence, which will only be detected if fusion happens, inducing a decrease in the FRET effect.

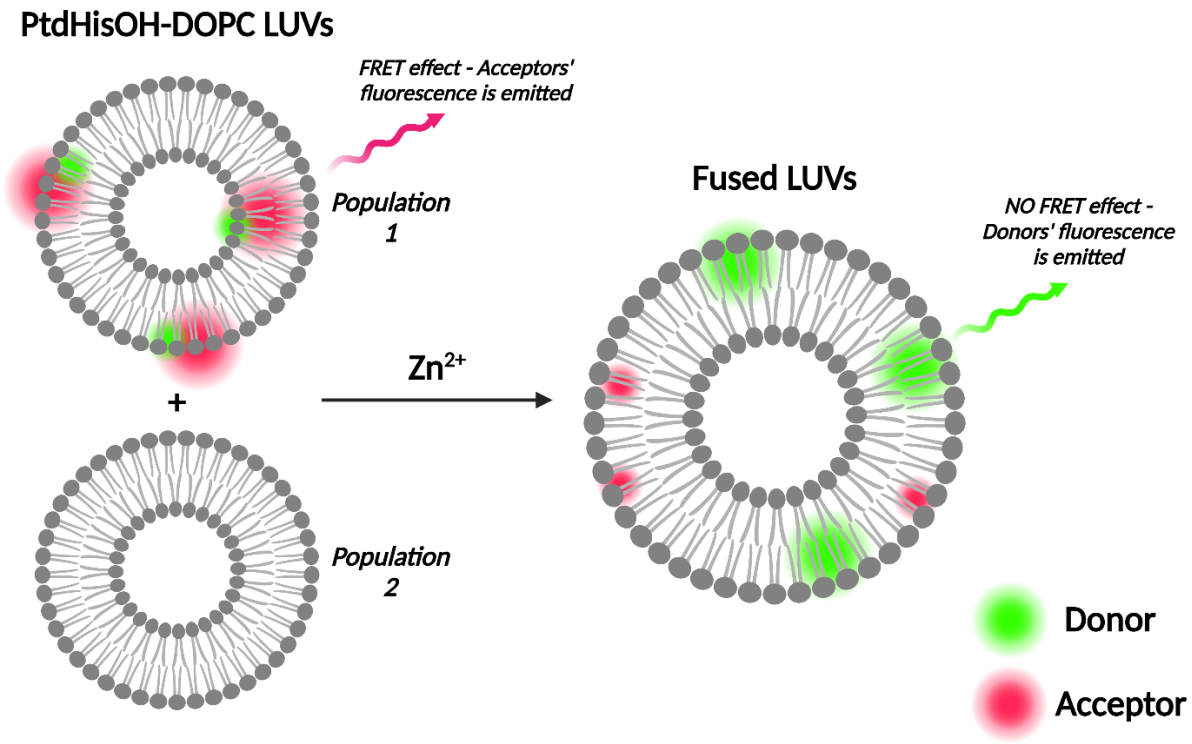


Figure 6.5 – Schematic representation of the FRET effect in LUVs. In population 1, LUVs containing the fluorophore lipids emit at the acceptor's wavelength, due to FRET. When population 2 (no fluorophore lipids) is mixed with population 1 in the presence of Zn^{2+}, the LUVs may fuse and the lipids diffuse, increasing the distance between the donor and the acceptor fluorophore lipids. The fluorescence emission of the donor is no longer quenched (no FRET) and can be detected. The acceptor is no longer excited and its emission decreases.

Three most likely scenarios can be expected if fusion happens:

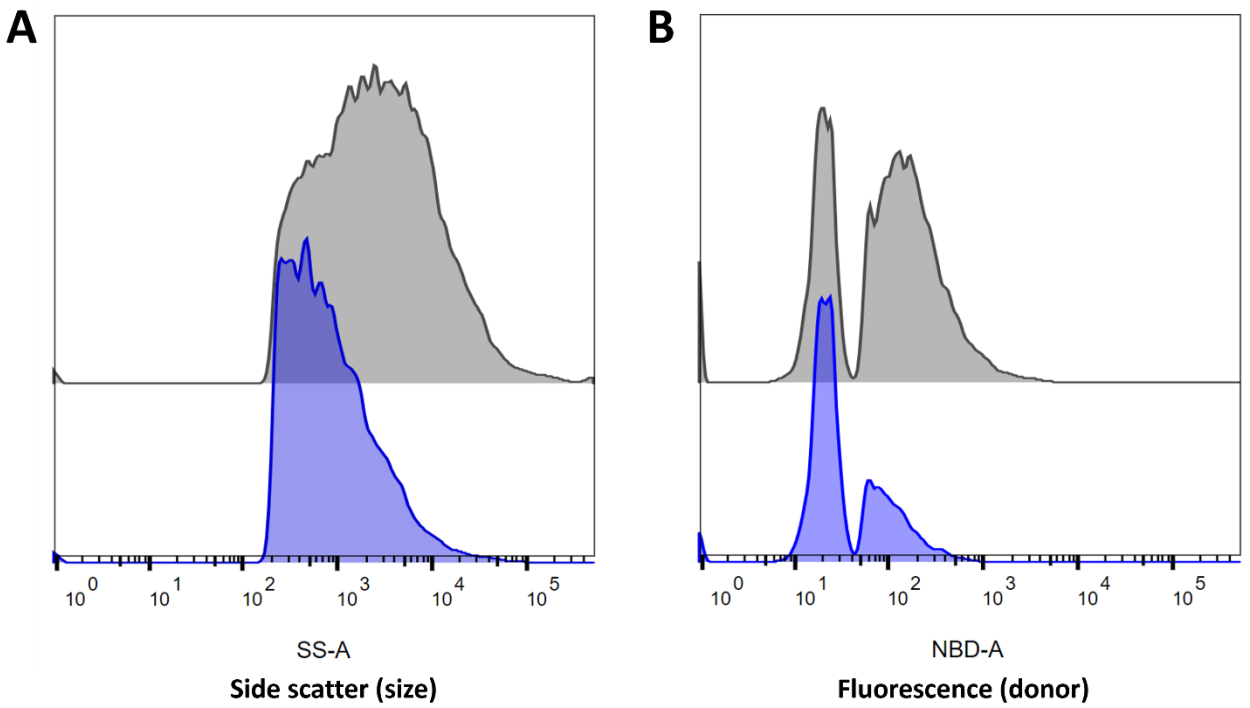
(i) One LUV from population 1 fuses with an LUV from population 2;

(ii) Two LUVs from population 1 fuse together;

(iii) Two LUVs from population 2 fuse together.

In scenarios (ii) and (iii), the vesicle size would increase but no change in fluorescence would be detected.

LUVs were prepared by extrusion using a 200 nm membrane. The two populations were mixed without Zn^{2+} (control) and in the presence of Zn^{2+}. LUVs were incubated for 30 minutes and analysed using flow cytometry.



	Count	Median SS-A	Median FITC-A	Median FITC-A	Freq. of parent
(+) $ZnCl_2$	14879	2435	99.2	159	67.6
(-) $ZnCl_2$	5477	698	24.9	98.9	33.8

Figure 6.6 – Histograms for the lipid-mixing of membrane fusion assay. PC 70 mol%-PtdHisOH 30 mol% LUVs are loaded with 2 mol% of Rhodamine B-PE and 2 mol% NBD-PE. Unlabelled PC-PtdHisOH LUVs are also prepared. LUVs populations are mixed as indicated in the figure and incubated at pH 8.2 for 30 minutes with 20 nmols of Zn^{2+} or without metal. Each sample is then analysed with a Flow NanoAnalyzer. For each sample, + 4000 events are recorded. Data shown is normalized.

Figure 6.7 shows the results of the experiment, represented by two histograms. Histogram A shows the side scatter, which is associated with the size of the particles. In the absence of a calibration curve, the units are arbitrary, but data between samples is comparable as they were recorded using the same settings. In histogram B, the relative fluorescence in the NBD channel ($Ex_{467\ nm}/Em_{539\ nm}$) is shown. Again, units are arbitrary, and the different samples are comparable. The grey plot represents the sample where the two populations are mixed in the presence of Zn^{2+}, and the blue curve shows the sample without Zn^{2+}.

Regarding the size of the sample, in the absence of Zn^{2+}, the peak is shifted towards the left. In contrast, in the presence of Zn^{2+}, the side scatter shows a much broader peak

shifted to the right. This represents a 3.5-fold increase in size, consistent with the results from DLS (Figure 6.3).

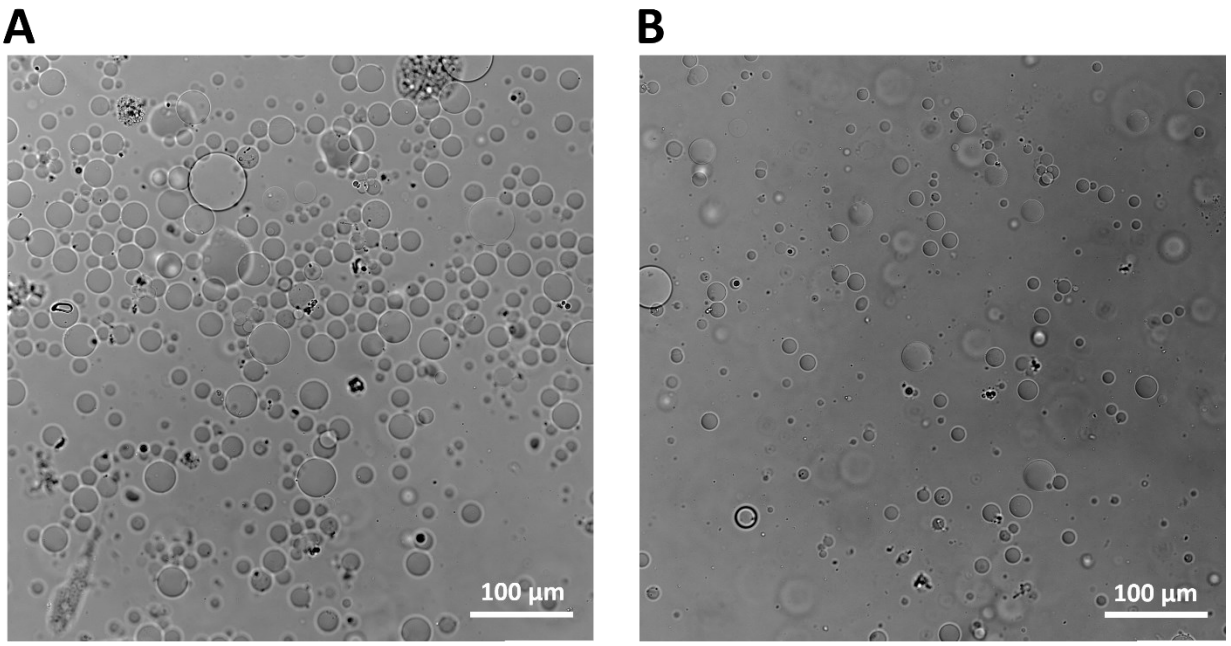
Regarding the fluorescence emission of PE-NBD, two peaks are detected in both conditions, indicating the presence of two populations with different levels of fluorescence. The first peak corresponds to the population that has not fused, and the second peak corresponds to the population that has increased in size.
The first median value relates to the fluorescence in the total population (peak 1 and 2). The data indicates that in the presence of Zn^{2+}, a 4-fold increase in fluorescence is measured compared to the sample not incubated with Zn^{2+} (99.2 vs 24.9). The second median value corresponds to the fluorescence intensity of the vesicles that have increased in size (159 vs 98.9). Compared to the median value of the whole population, the fluorescent intensity is much higher (1.7-fold). Finally, the frequency of parent represents the percentage of vesicles that are positive, meaning that have an increase in size and fluorescence. Here, the data indicates that in the presence of Zn^{2+}, twice as many particles have fused (67.6% vs 33.8%).
Since fluorescence can only occur if LUVs fuse, the data indicates that the fusion of LUVs is indeed enhanced in the presence of Zn^{2+}.
This notable increase in size and fluorescence in the sample containing the labelled and unlabelled populations of LUVs in the presence of Zn^{2+} combined with previous data strongly indicates that LUVs containing PtdHisOH merge in the presence of Zn^{2+}. These results are very promising as membrane fusion is key in many biological mechanisms such as fertilization, virus infection and exocytosis and the PtdHisOH lipid could be used in models of membrane fusion [214].

The investigation into lipid-lipid interactions facilitated by a metal ion reveals the merging of LUVs, particularly in the presence of Zn^{2+} and in alkaline conditions, which in turn facilitate stronger metal binding. These findings pave the way for further exploration of lipid-lipid and lipid-protein interactions within artificial cells, which will be the focus of Sections 6.4 and 6.5.

6.3. Making GUVs with PtdHisOH

The ability to generate GUVs with PtdHisOH in the membrane would broaden the application of the lipid to artificial cell technologies. GUVs measure more than 1 μm which is comparable to bacteria in size (1 μm) as well as animal and plant cells (10-100 μm) [55]. GUVs also offer the possibility to encapsulate SUVs or LUVs, making more complex structures resembling real cells [131].

In this experiment, PtdHisOH-PC GUVs were made by emulsion phase transfer as described in the methods chapter (section 2.4.3). PC GUVs were made as controls, alongside PC-PtdHisOH GUVs. Yields were calculated based on the number of GUVs generated (average cell count) and vesicle size was measured based on microscopy, using the software ImageJ; results were compared between samples.



	Average size (μm)	Std dev	Average cell count	Std dev
PC GUVs	26.8	8.32	235	29.51
PC-PtdHisOH GUVs	17.5	5.29	108	8.08

Figure 6.7 – Incorporation of PtdHisOH in the membrane of PC GUVs. (A) 100 mol% PC GUVs for control. (B) 80 mol% PC – 20 mol% PtdHisOH GUVs. The images shown are representative, more images can be found in appendix 1. The GUVs are made by phase transfer using sucrose 0.5 M on the inside and glucose 0.5 M on the outside. Samples are imaged using brightfield microscopy. The average size is measured from 100 GUVs. The average cell count represents the

number of GUVs in one image, the standard deviation being the error between three images of three independent experiments. The analysis was done using Image J.

Comparing images A and B from Figure 6.7 reveals that incorporating 20 mol% PtdHisOH in GUVs reduces the yield by 50%, compared to the 100 mol% PC GUVs. The addition of PtdHisOH in the GUVs membrane appears to also impact the size of the GUVs produced, as vesicles containing PtdHisOH are 1.5-fold smaller on average.

Additionally, a high number of PtdHisOH GUVs burst over time (10 minutes), which was not observed in the sample containing only PC. Attempts to produce GUVs with higher mol% of PtdHisOH resulted in yields close to zero. These findings suggest that the incorporation of PtdHisOH in the membrane of GUVs makes them unstable, possibly because of the membrane asymmetry (see Figure 6.2).

6.4. Lipid-protein interaction in GUVs

6.4.1. Lipid-protein binding in PtdHisOH GUVs

We showed in Figure 4.9 and Figure 4.10 (chapter 4) that the PtdHisOH lipid could bind a his-tagged protein through a metal ion, preferably Zn^{2+}, in the coating system. This study also showed that a minimum density of PtdHisOH was needed to achieve binding. In this experiment, we attempt to decorate the membrane of PtdHisOH GUVs with his-mEGFP through lipid-protein binding, as a first step towards more complex applications for artificial cells.

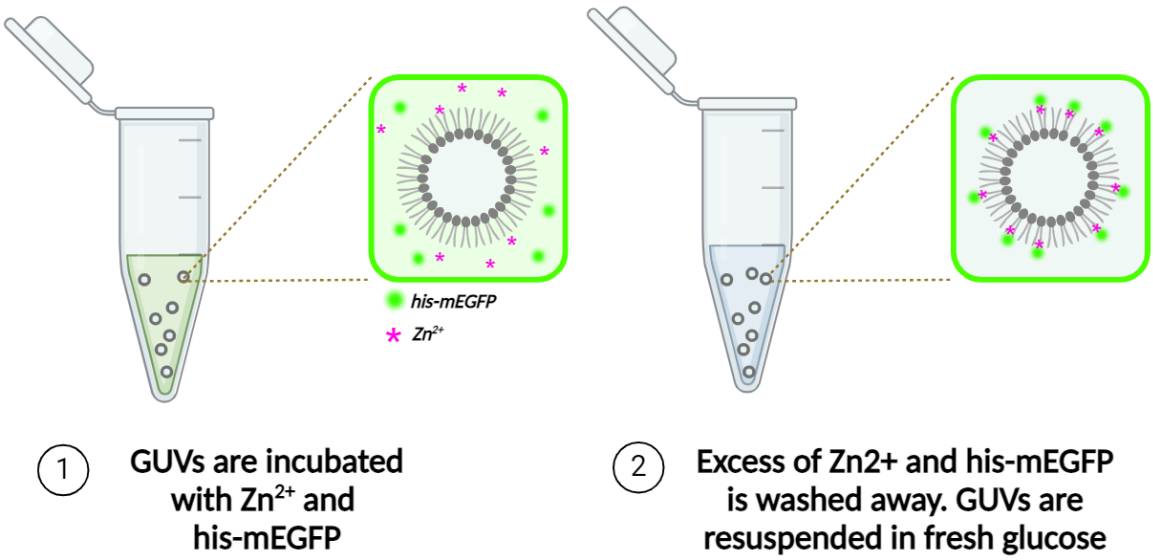


Figure 6.8 – Schematic representation of the lipid-protein binding in GUVs. GUVs containing sucrose 0.5 M + HEPES on the inside are incubated with Zn^{2+} and GFP in glucose solution + HEPES simultaneously. After 30 minutes of incubation, GUVs are span-down at 9,000 xg, the supernatant containing the excess of his-mEGFP and Zn^{2+} is removed and GUVs are resuspended in fresh glucose.

In this experiment, GUVs were made by phase transfer, using increasing amounts of PtdHisOH ranging from 0 mol% to 15 mol%. The GUVs were incubated in a glucose solution supplemented with Zn^{2+} and his-mEGFP for 30 minutes. The supernatant containing the excess of Zn^{2+} and his-mEGFP was washed away and GUVS were resuspended in fresh glucose solution. An alternative to this experiment would have been to encapsulate the his-mEGFP and Zn^{2+} in the GUVs, to use fewer amounts of protein and reduce the background fluorescence, but as shown in Figure 6.2, PtdHisOH is predominantly located on the outer membrane of the vesicles.

The samples were visualised by confocal microscopy to allow a better focus on the membrane and analysed using image J.

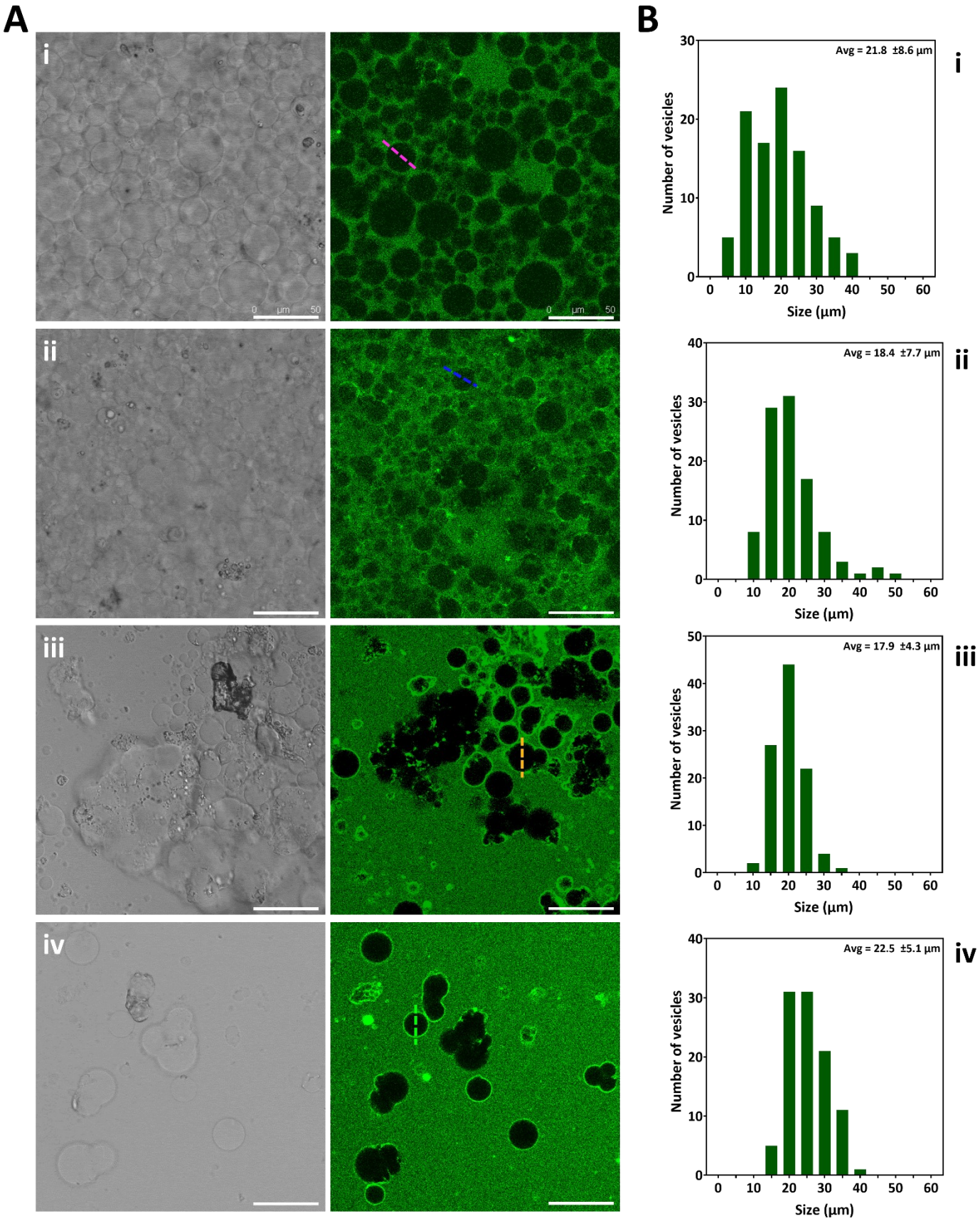


Figure continues in the next page

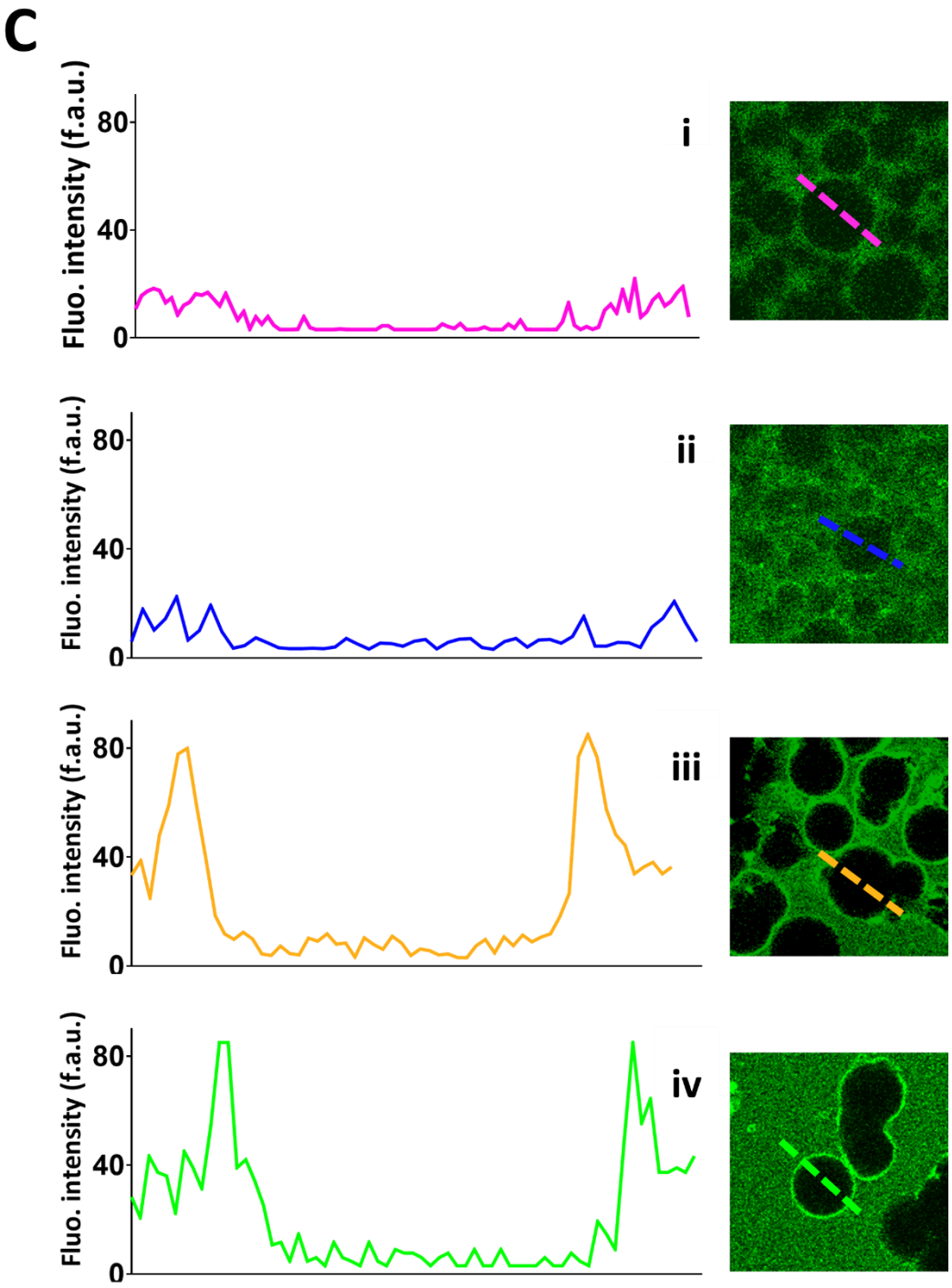


*Figure 6.9 – Lipid - his-mEGFP binding in PtdHisOH GUVs. GUVs containing increasing amounts of PtdHisOH lipid i) 0 mol%, ii) 5 mol%, iii) 10 mol%, iv) 15 mol% are incubated in 0.5 M glucose solution supplemented with 10 mM HEPES pH 7.4, 10 μM Zn^{2+} and 6.5 μM his-mEGFP. All scale bars shown represent 50 μm. This experiment was replicated twice with different GUV batches. Representative images are shown in this figure, more images for each condition can be found in Appendix 2. Brightfield and fluorescence confocal images are shown in (**A**), the size distribution of 100 vesicles is shown in (**B**) and the fluorescence intensity profiles across the indicated GUVs (one profile per PtdHisOH concentration) are shown in (**C**).*

Figure 6.9 shows the binding between PtdHisOH GUVs and his-mEGFP through Zn^{2+}. PC GUVs with increasing amounts of PtdHisOH are studied, keeping the concentration of Zn^{2+} and his-mEGFP constant.

At 0 mol% PtdHisOH (A.i), a high yield of GUVs is achieved for phase transfer, visible as black circles in the fluorescent field, with background fluorescence from his-mEGFP in the glucose buffer. The size distribution of the population is quite spread, with 50% of the population measuring between 10 and 20 μm (B.i). The fluorescence intensity profile (C.i) shows background fluorescence oscillating around 20 f.a.u., dropping to around 10 f.a.u. inside the GUV, indicating no increase in membrane fluorescence and therefore, no binding of his-mEGFP.

Increasing PtdHisOH to 5 mol% (A.ii) results in a similarly high yield of GUVs, albeit narrower in size distribution (50% of the population between 15 and 20 μm) (B.i). Some GUVs exhibit brighter fluorescence in some sections of the membrane compared to the background, indicating some binding where the density of PtdHisOH is high enough. The fluorescence profile of the chosen GUV remains similar to 0 mol% PtdHisOH (C.ii).

At 10 mol% PtdHisOH, the size distribution narrows a bit more in comparison to lower concentrations of PtdHisOH (A.iii & B.iii). GUV size is comparable to the size with 5 mol% PtdHisOH, and we observe some GUV-GUV binding. A distinct fluorescent ring, much brighter than background fluorescence, surrounds all GUVs. The fluorescence profile shows background fluorescence close to 30-40 f.a.u., with peaks reaching 80 f.a.u. corresponding to the membrane, and dropping drastically inside the GUV. Another peak is detected at 80 f.a.u. for the other side of the GUV (C.iii). This indicates that his-mEGFP is binding to the membrane of the vesicles and that the density of PtdHisOH is enough to cover the whole vesicle.

At 15 mol% PtdHisOH, the size distribution is narrow, with average GUV size remaining between 20 and 25 μm (A.iv & B.iv). More GUVs bind together, forming larger structures like aggregates. A clear fluorescent ring surrounds the vesicles, not visible in bound regions, suggesting hemi-fusion. The fluorescence profile resembles that of 10 mol% PtdHisOH, with peaks reaching 80 f.a.u. detected for the membrane (C.iv).

This data shows that PtdHisOH can bind his-mEGFP in GUVs through a Zn^{2+}. The binding can be tuned to achieve the desired coverage of his-mEGFP and the strength of the

binding. 20 mol% PtdHisOH is the maximum density that can be reached in GUVs, as using higher amounts results in structures that collapse quickly. The aggregation of GUVs together, suggested as hemi-fusion, will be investigated in the following experiment.

6.5. Lipid-lipid interaction in GUVs

In section 6.2.2, we elucidated the binding and fusion of PtdHisOH LUVs through Zn^{2+}, leading to the formation of larger fused structures. However, in Figure 6.9, the confocal images suggests that the GUVs do not fuse like LUVs, therefore, further investigation is required.

Achieving the binding of GUVs or fusion would be a step forward towards the creation of tissue-like structures.

In this experiment, PtdHisOH GUVs were made by phase transfer and PC GUVs were used for control. Zn^{2+} was added to the glucose buffer containing the GUVs, and samples were immediately imaged, to try to detect binding or fusion. Movement of the GUVs are driven by convection forces only, as no time was given for the vesicles to sink before starting the imaging. Clips were recorded over periods of 10 minutes, and the following images were extracted.

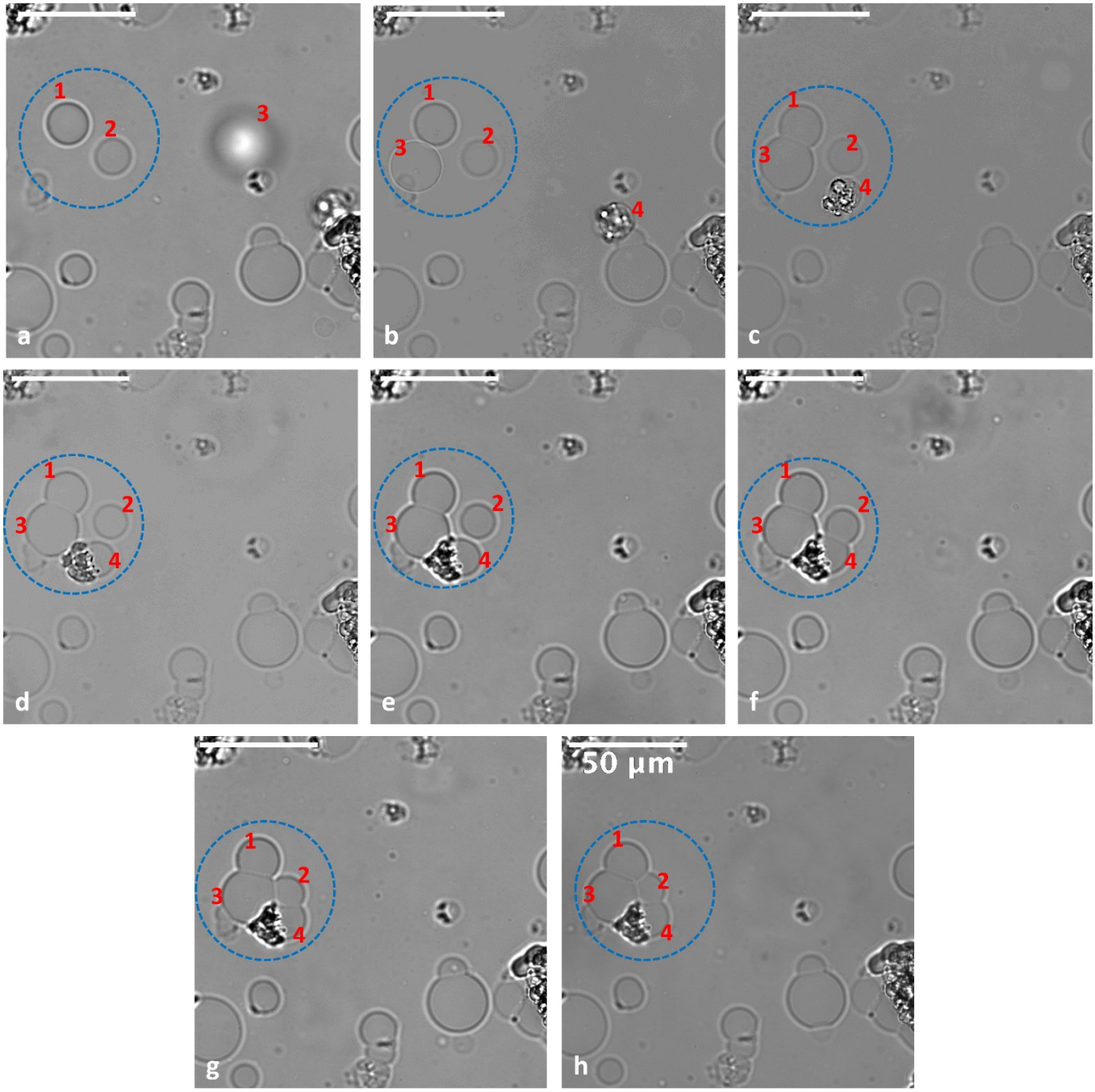


Figure 6.10 – PtdHisOH GUVs bind to each other through a metal ion. a,b,c,d,e,f,g,h frames are placed in chronological order and represent the binding of 4 GUVs together over time (5 minutes). 80 mol% PC-20 mol% PtdHisOH GUVs were incubated with 10 µM of Zn^{2+}. The samples were immediately imaged and monitored over time, using brightfield microscopy. All scale bars shown represent 50 µm. This experiment was replicated twice with different GUV batches. These images are representative, additional data is shown in appendix 3.

In Figure 6.10-a, two vesicles in proximity are circled, while a third vesicle (labelled 3) is entering focus. Subsequently, in frame (b), vesicles 1 and 3 make contact, and after a

brief period, they undergo hemi-fusion (c). It is observable that the outer membrane is shared, yet a lipid layer still separates the two vesicles. Additionally, in frame (c), another vesicle carrying some oil comes into focus. Moving to frame (d), vesicles 3 and 4 come into contact and hemi-fuse in frame (e). Concurrently in frame (e), vesicles 4 and 2 also come into contact. Finally, in the subsequent frames, vesicle 2 undergoes hemi-fusion with all surrounding vesicles: hemi-fusion with vesicle 4 in frame (f), hemi-fusion with vesicle 3 in frame (g), and hemi-fusion with vesicle 1 in frame (h).

This convergence of four vesicles results in the formation of a larger structure with distinct compartments. This behaviour of vesicles undergoing hemi-fusion was solely observed in GUVs containing PtdHisOH in the presence of Zn^{2+}. No hemi-fusion of GUVs was observed in controls containing PtdHisOH without Zn^{2+} (Figure 6.7) or in PC GUVs with Zn^{2+}.

The frequency of hemi-fusion has been calculated to be close to 80%, with hemi-fusion between 2 to a maximum of 10 vesicles being recorded (appendix 3).

6.6. Catalysis – Fura-2AM

In this experiment, we test whether the esterase activity of PC-PtdHisOH can be utilised beyond the artificial substrate FDA, tested in Chapter 5. We chose FURA-2 as the substrate, as it is commonly used in cellular assays to monitor signalling events [215, 216], and could be potentially applied to artificial cell experiments.

For this proof of concept, a nested vesicle system was created, by encapsulating catalytic LUVs into POPC GUVs, to create a confined space for the product to be catalysed. The experiment was developed and adapted from previous work on nested vesicles [131]. Using the phase transfer standard protocol (detailed in Methods chapter – section 2.4.3), GUVs were generated using POPC to enhance yields. In the sucrose solution used in phase transfer, extruded LUVs, together with Zn^{2+}, were added, resulting in GUVs with nested LUVs inside. As controls, PC LUVs or PC-PE LUVs were encapsulated, while PC-PtdHisOH LUVs were encapsulated for the actual experiment.

Fura-2 acetoxymethyl (AM) is a cell-permeant ester commonly used to measure intracellular Ca^{2+} concentrations by fluorescence [217]. Initially non-fluorescent, Fura-

2AM becomes fluorescent upon hydrolysis by the esterase naturally found in the cell membrane and in the presence of Ca^{2+}. Fura-2AM has also been used to detect the presence of Zn^{2+} by fluorescence detection [216, 218] (Figure 6.11-A).

In this experiment, Fura-2AM was used to detect the catalysis inside the GUVs, in the presence of Zn^{2+}. First, Fura-2AM permeates the membrane of GUVs. The compound is catalysed by the esterase properties of PtdHisOH LUVs and becomes fluorescent thanks to the presence of Zn^{2+} in the lumen of the GUVs. Once hydrolysed, Fura-2 is unable to leave the membrane compartment; the fluorescent compound accumulates in the GUV and fluorescence is monitored by fluorescence microscopy (Figure 6.11-B).

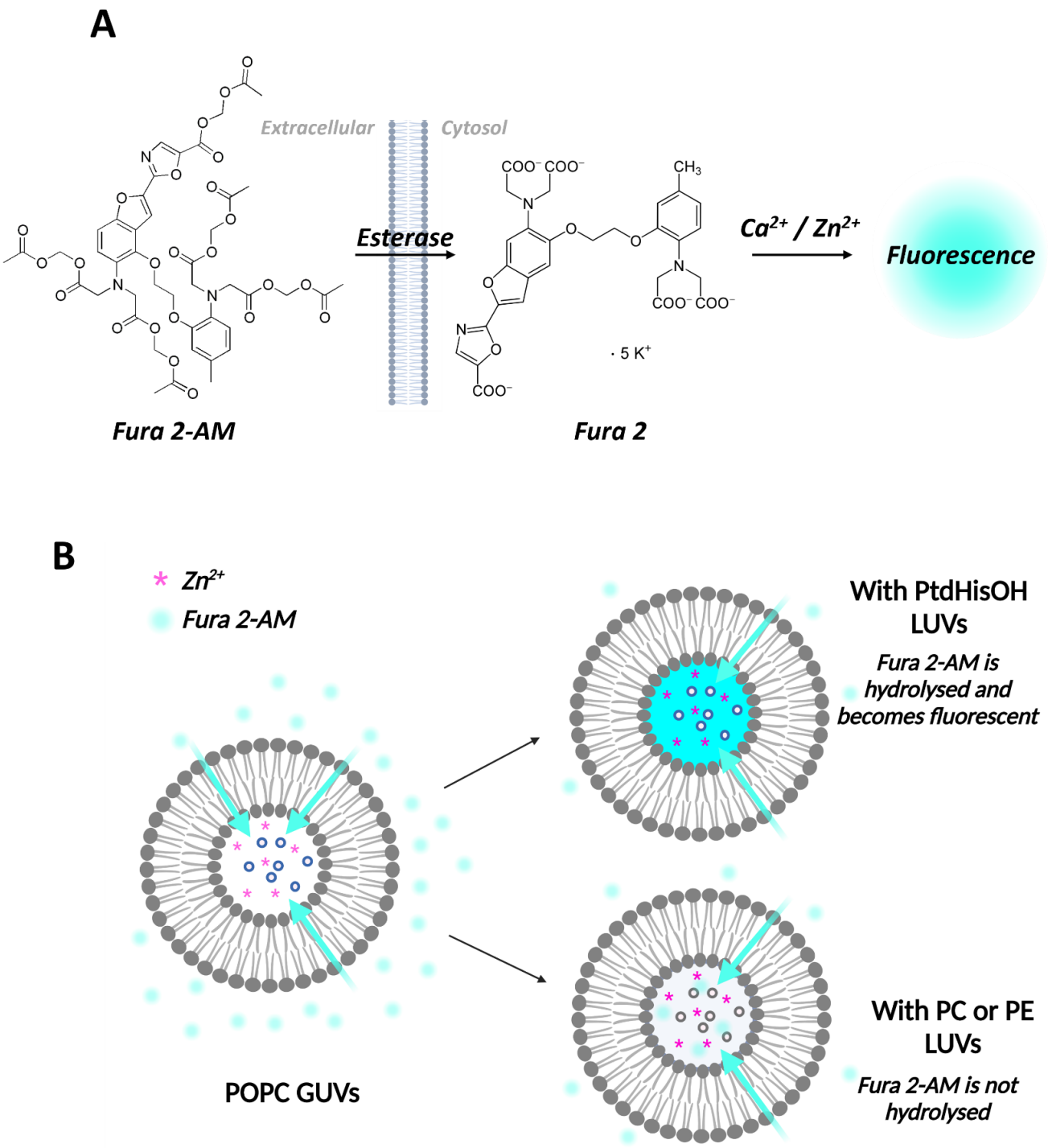


*Figure 6.11 – Schematic representation of catalysis reaction in GUVs. Catalytic PtdHisOH LUVs (70 mol% PC-30 mol% PtdHisOH) are encapsulated in POPC GUVs, in sucrose buffer supplemented with 10 mM HEPES pH 7.4 and 1 μM Zn^{2+}. The application for cellular detection is shown in (**A**); the proposed experiment for proof of concept is shown in (**B**).*

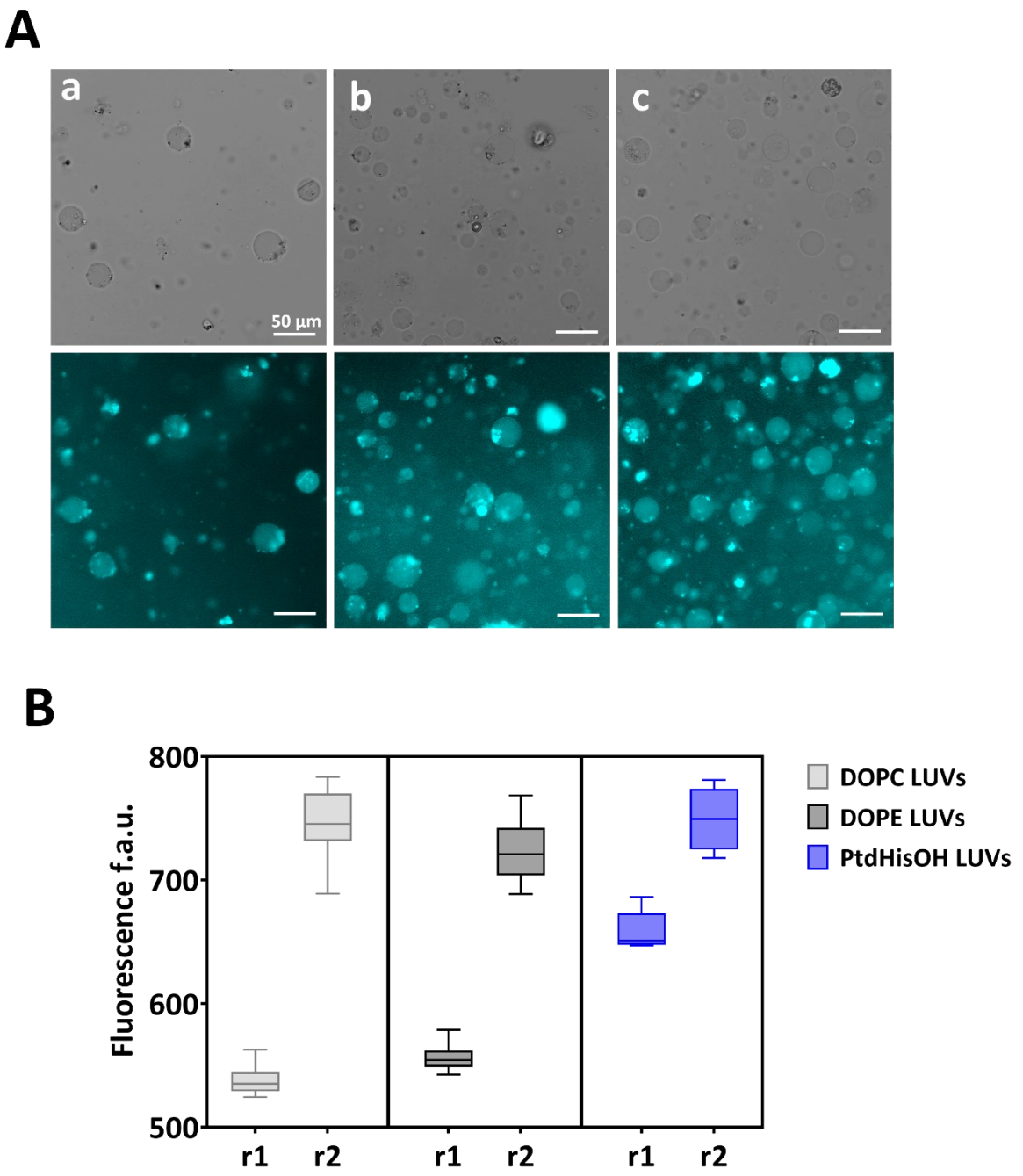


*Figure 6.12 – Catalysis of Fura-2AM by nested PtdHisOH LUVs in the presence of Zn^{2+}. 100 mol% PC LUVs or 70 mol% PC-30 mol% PE LUVs or 70 mol% PC-30 mol% PtdHisOH were encapsulated in POPC by phase transfer, with 1 µM Zn^{2+} in 10 mM HEPES-0.5M sucrose solution. GUVs were placed under the microscope and 1mM Fura-2AM dissolved in DMSO was added to the sample. The experiment was replicated twice, with different batches of LUVs. Both brightfield and fluorescence images for controls with PC LUVs (a) and PC-PE LUVs (b) are shown, as well as PC-PtdHisOH LUVs (c). All the scale bars represent 50 µm (**A**). The average fluorescence of replicate 1 (r1) and replicate (2) for the three samples is shown in the boxplot (**B**).*

Figure 6.12 – A, shows that the average size of GUVs is comparable in the three samples, close to 20 µm. However, GUVs with nested PC LUVs exhibited half the yield compared to those with PE or PtdHisOH LUVs. Regarding the fluorescence images, it is expected to observe no fluorescence in the PC nested LUVs, since Fura 2-AM cannot be catalysed. Yet in image A-a, some fluorescence is detected inside the GUVs, indicating successful crossing of the membrane by Fura-2AM, but also catalysis of Fura 2-AM into Fura2. Similarly, little or no catalysis is expected for the PE LUVs, as concluded in Chapter 5. In the fluorescence field of figure A-b, fluorescence is also detected in the lumen of GUVs. In the last condition with PtdHisOH LUVs, it is expected that the LUVs catalyse the compound, and after forming a complex with the remaining Zn^{2+}, Fura2 becomes fluorescent. Again, fluorescence is detected inside the GUVs.

Figure 6.12 – B shows the fluorescence intensity of an average of fifteen GUVs per experiment. Measurements were conducted using ImageJ, and contamination with oil exhibiting high fluorescence was avoided.

In the first replicate, the sample containing PtdHisOH LUVs shows 1.2-fold higher intensities than the controls. However, these results are not replicable as in replicate 2, the three samples show very similar fluorescence. We can also note that the buffer shows some fluorescence, indicating that some Fura-2AM is being hydrolysed outside the vesicles.

To be able to drag a conclusion from this experiment, some optimisation is still necessary. Understanding why Fura-2AM is catalysed in the controls in the absence of catalytic LUVs is crucial, as well as reducing background fluorescence in the buffer. It should be considered that both the PtdHisOH LUVs and the Fura-2 will form complexes with the free Zn^{2+} encapsulated in the GUVs, meaning that the Fura-2/Zn^{2+} complex could disrupt the esterase activity. Moving forward, both Ca^{2+} and Zn^{2+} could be encapsulated, as Zn^{2+} would be preferred for catalysis and Ca^{2+} would be captured by the Fura-2. Another optimisation parameter could be to increase the amount nested LUVs, to detect a clear and bright fluorescence on the case of Fura-2AM catalysis.

6.7. Conclusions & future work

Chapter 6 focuses on the application of the novel lipid in the context of artificial cells. In this chapter, we elucidated the membrane asymmetry in PtdHisOH vesicles, highlighting a preference for the lipid to sit in the outer leaflet of the membrane. Investigating lipid-lipid interaction in LUVs and GUVs, the results showed an increase in particle size and lipid mixing between vesicles, suggesting the fusion of LUVs in the presence of Zn^{2+}. Additionally, hemi-fusion was observed in PtdHisOH GUVs in the presence of Zn^{2+}. Furthermore, assays involving lipid-his-tagged binding were performed in GUVs, showing the ability to decorate an artificial cell membrane with his-tagged protein through a metal ion. Lastly, we tried to apply the catalytic properties of the lipid in a nested vesicle system, but further optimisation of the experiment is required to draw conclusions.

7. Conclusions & future work

The overall aim of this thesis was to develop new tools for membrane functionalisation in artificial cells. We optimised a platform for artificial lipid synthesis and focused on PtdHisOH lipid synthesis, characterisation, and applications.

7.1. Summary of findings

In this research project, we successfully developed a new tool to functionalise artificial cell membranes and promote binding of his-tag compounds, cell-cell interactions and creating catalytic vesicles.

We achieved the synthesis of phosphatidyl-histidinol, a novel phospholipid containing a histidine headgroup, using enzyme-assisted synthesis. In chapter 3, the synthesis and scale-up were optimised to achieve the highest yields with the minimal amounts of material. For 1 unit of PLD, we achieved a yield of 80% making 3 g of PtdHisOH. Comparing our results to similar transphophatidylation reactions using the PLD from *Streptomyces* sp., DOPC as starting material and simple primary alcohols as substrates (ethanolamine, glycerol), we were able to synthesise at least twice as much product using 1 unit of PLD [219]. These findings will be of high economy impact for the biotech industry.

The functionality of the lipid developed is also a major achievement in this thesis (chapter 4), as it could be applied in a wide range of applications. Compared to other synthetic imidazole functionalised lipids, PtdHisOH is a phospholipid carrying a histidine headgroup that is found in nature. The lipid is therefore chemically close to natural compounds and is expected to be more biocompatible than already existing synthetic compounds. Incorporated into artificial cells, this lipid opens up applications in medicine for nanodelivery. The lipid could also be used in the coating system for high-throughput analytics: it could be used for affinity detections in the same way that antibodies are used.

PtdHisOH showed catalytic properties through the imidazole moiety, in accordance with literature (chapter 5). The lipid showed catalytic activity towards phosphoester and ester bonds, with a preference for the latter. The catalytic properties also revealed to be metal-dependent, specifically towards zinc, which was expected as well. What was not expected was the dependency of catalysis on lipid presentation.

The formation of asymmetric membranes with the PtdHisOH lipid being predominantly located on the outer leaflet of the membrane was also unexpected (chapter 6). Further experiments regarding the asymmetry of PtdHisOH vesicles could be performed to confirm this finding. The PtdHisOH being negatively charged, zeta potential measurements could be performed and results compared to other negatively charged membranes. Finally, we successfully showed the possibility to bind his-tagged mEGFP to the membrane of vesicles, in a controllable way. In the future, the reversibility of the binding could be tested by adding a strong chelating agent to a sample containing protein coated vesicles. Further investigation on the GUV-GUV interactions is also needed, such as modulating the amount of PtdHisOH incorporated in the membrane to see if binding can be achieved instead of hemi-fusion.

7.2. Future work

7.2.1. Sythesis of functional phospholipids

The successful synthesis of PtdHisOH by PLD transphosphatidylation could lead to the synthesis of other functional phospholipids through head group modifications.
Focusing on other ways to bring vesicles together, H-bonding of nucleotides like DNA or formation of disulfide bridges like proteins could be explored (Figure 7.1).

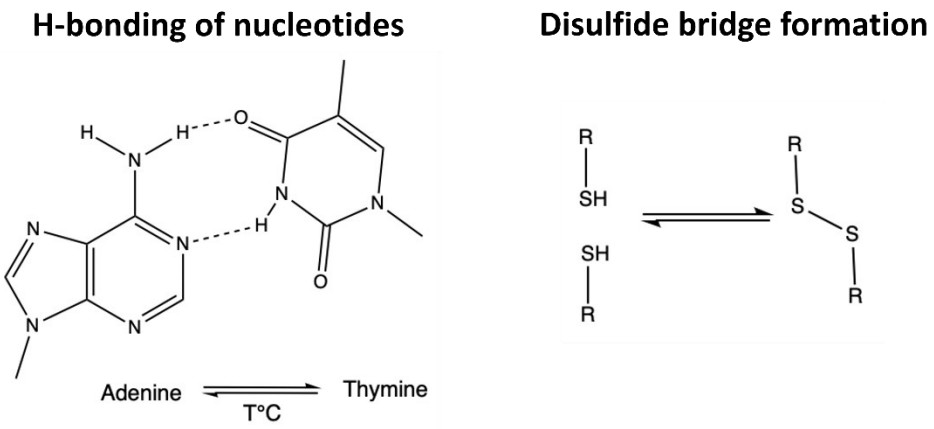


Figure 7.1 – Examples of lipid functions that could be explored in the future.

Preliminary work was done on the synthesis of a nucleoside headgroup lipid, with the objective to create a temperature dependent binding inspired by the double stranded DNA. This nucleoside lipids could be applied to decorate artificial cell membranes with nucleic acids

payloads (DNA or RNA) for gene or drug delivery systems. This functionality could also be used to bring vesicles together in a controlled manner to create tissue like structures. Synthesis of nucleolipids has already been reported using PLD for the synthesis of a thymidine-phospholipid from PC [220, 221]. Here, we attempted to synthesise three nucleoside phospholipids, adenosine, cytidine and thymidine using the optimised conditions developed in the 2-phase system synthesis of PtdHisOH, adenosine and cytidine being novel phospholipid headgroups. Figure 7.2 shows the accumulation of nucleoside phospholipids in the organic phase after 20 minutes and 60 minutes of reaction in the 2-phase system. The data indicated that all three nucleosides are successfully transphosphorylated by PLD, with thymidine being the best substrate. These results are promising for the synthesis of these lipids and open the door for many other syntheses.

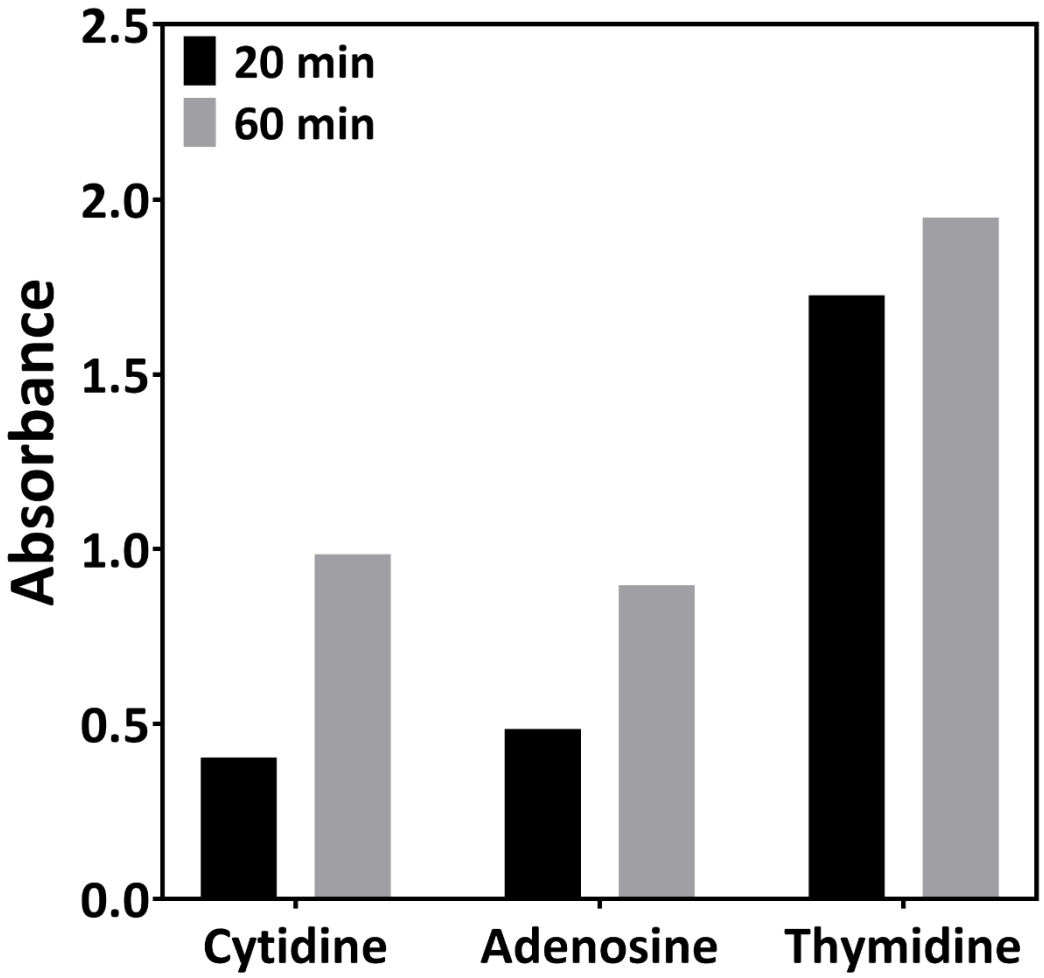


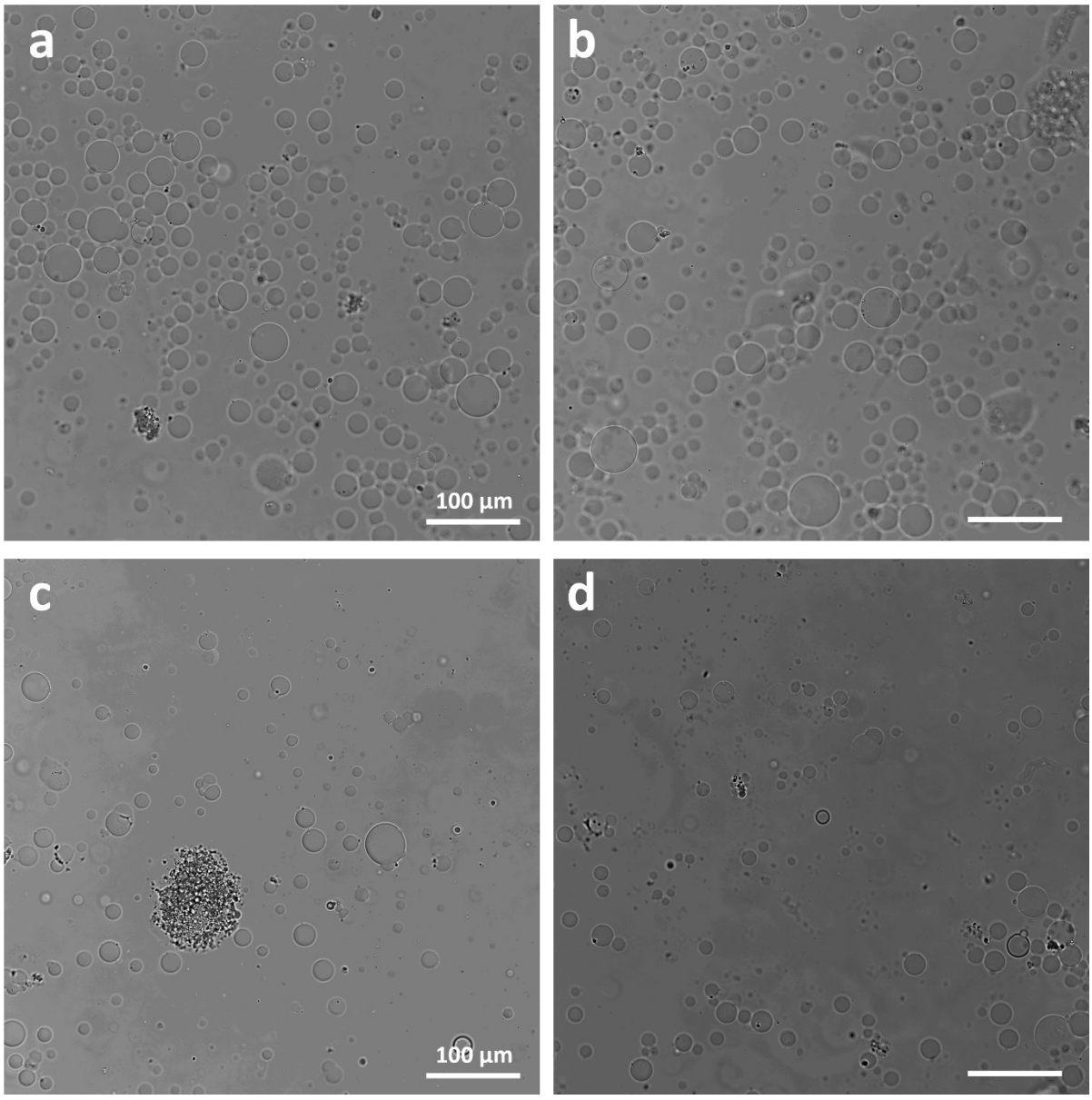
Figure 7.2 – Transphosphatidylation of nucleoside headgroup. 30 mM adenosine, 100 mM cytidine and 150 mM thymidine were used as substrates for the transphosphatidylation reaction using PC as starting material. Reactions were performed using standard procedures for the 2-

phase system. The products were detected by absorbance, $Abs_{259\ nm}$ for adenosine, $Abs_{272\ nm}$ for cytidine and $Abs_{266\ nm}$ for thymidine. The data presented shows the delta between the absorbance value and the blank measured at 0 min.

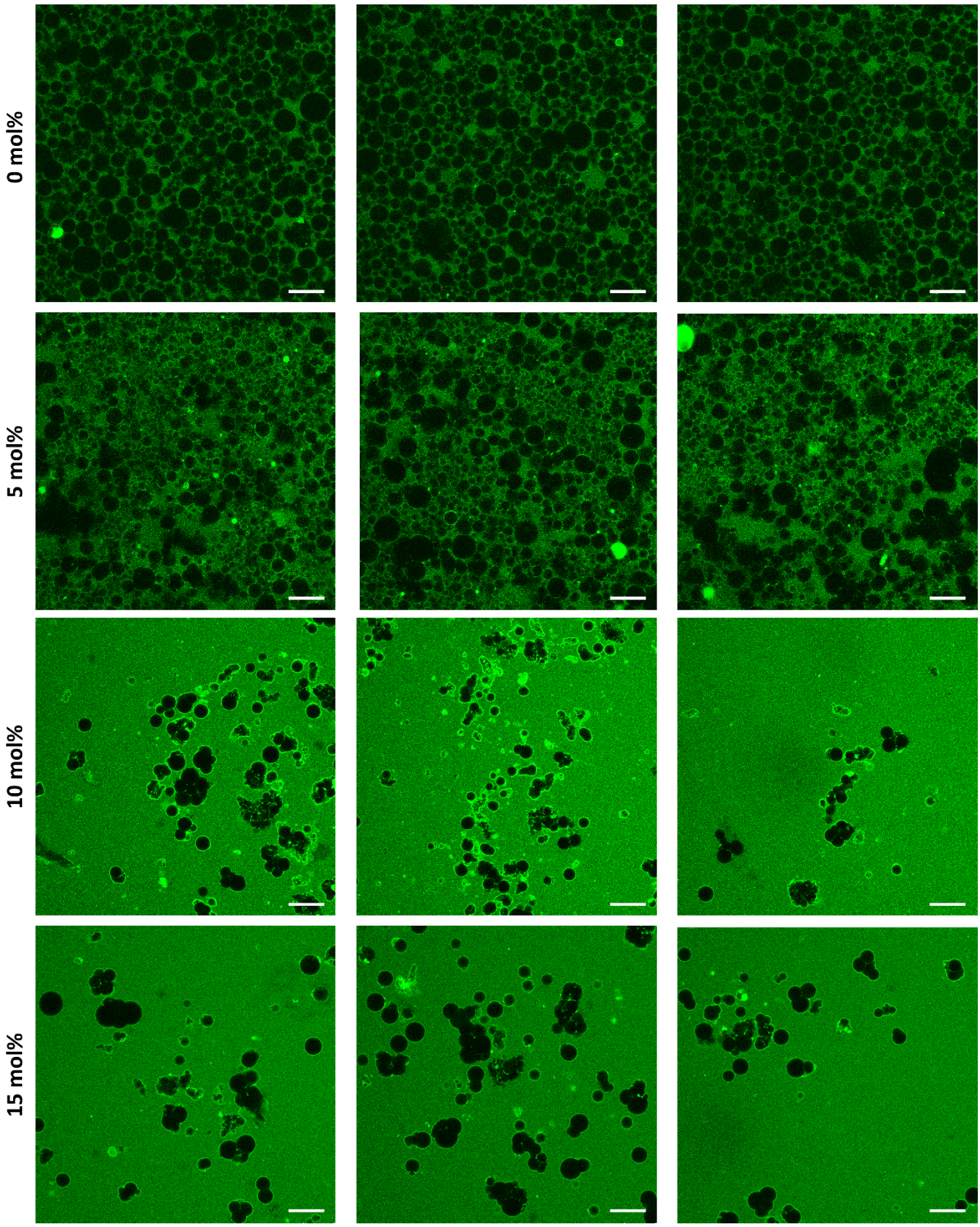
This thesis describes the development of a new tool for functionalisation of artificial cell membranes through the phospholipids headgroups. In this work, we focused on the development of PtdHisOH lipid, which promotes the binding of his-tag proteins or any other his-tag compound to the membrane through Zn^{2+} complex formations. This lipid has also shown catalytic abilities in the vesicular system, being useful for in situ chemical reactions. Finally, the lipid can promote vesicle-vesicle interactions through the metal binding, which offers the possibility of recreating artificial tissues or induce communication between artificial cells.

Having a platform to synthesise customisable functional lipids could be a major step forward for the use of artificial cells in real-world applications.

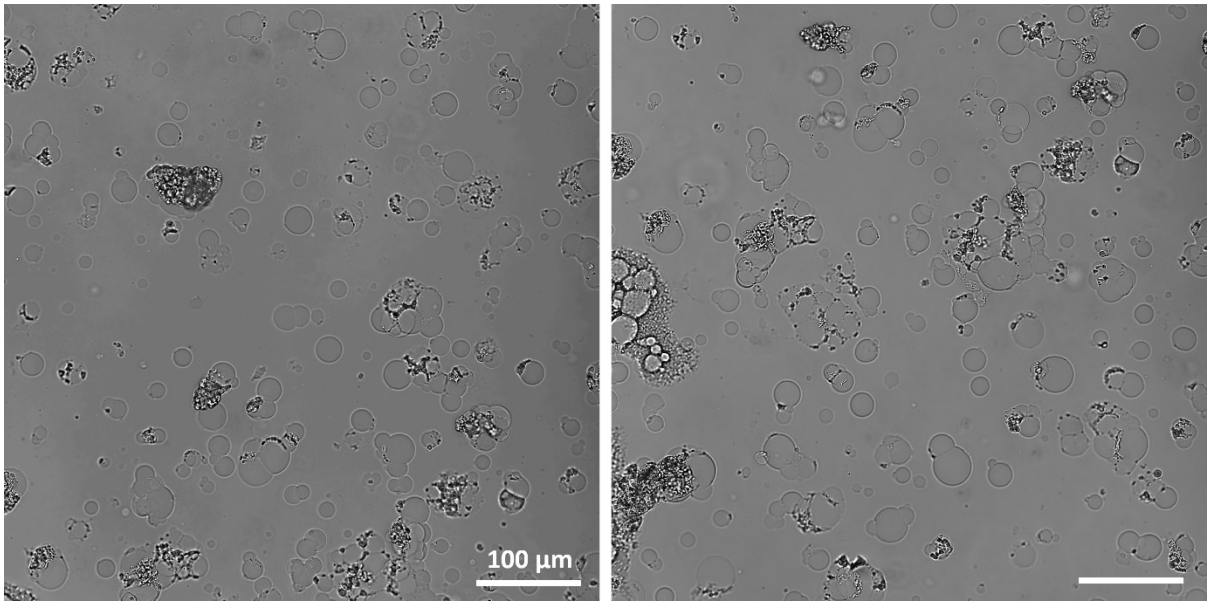
8. Appendix



Appendix 1 – Incorporation of PtdHisOH in the membrane of PC GUVs. (a-b) 100 mol% PC GUVs for control. (c-d) 80 mol% PC – 20 mol% PtdHisOH GUVs. The GUVs are made by phase transfer using sucrose 0.5 M on the inside and glucose 0.5 M on the outside. Samples are images using brightfield microscopy.



Appendix 2 – Lipid - his-mEGFP binding in PtdHisOH GUVs. GUVs containing increasing amounts of PtdHisOH lipid are incubated in 0.5 M glucose solution supplemented with 10 mM HEPES pH 7.4, 10 μM Zn^{2+} and 6.5 μM his-mEGFP.



Appendix 3 – PtdHisOH GUVs bind to each other through a metal ion. 80 mol% PC-20 mol% PtdHisOH GUVs were incubated with 10 µM of Zn^{2+}. The samples are imaged after a 30-minute incubation using brightfield microscopy.

9. References

1. Elani, Y., *Interfacing Living and Synthetic Cells as an Emerging Frontier in Synthetic Biology.* Angew Chem Weinheim Bergstr Ger, 2021. **133**(11): p. 5662-5671.
2. Cameron, D.E., C.J. Bashor, and J.J. Collins, *A brief history of synthetic biology.* Nat Rev Microbiol, 2014. **12**(5): p. 381-90.
3. Garner, K.L., *Principles of synthetic biology.* Essays Biochem, 2021. **65**(5): p. 791-811.
4. Yan, X., et al., *Applications of synthetic biology in medical and pharmaceutical fields.* Signal Transduct Target Ther, 2023. **8**(1): p. 199.
5. Khalil, A.S. and J.J. Collins, *Synthetic biology: applications come of age.* Nat Rev Genet, 2010. **11**(5): p. 367-79.
6. Zeng, Y., et al., *Advanced genome-editing technologies enable rapid and large-scale generation of genetic variants for strain engineering and synthetic biology.* Curr Opin Microbiol, 2022. **69**: p. 102175.
7. Voigt, C.A., *Synthetic biology 2020-2030: six commercially-available products that are changing our world.* Nat Commun, 2020. **11**(1): p. 6379.
8. Cohen, S.N., et al., *Construction of biologically functional bacterial plasmids in vitro.* Proc Natl Acad Sci U S A, 1973. **70**(11): p. 3240-4.
9. Lanigan, T.M., H.C. Kopera, and T.L. Saunders, *Principles of Genetic Engineering.* Genes (Basel), 2020. **11**(3).
10. Ke, J., B. Wang, and Y. Yoshikuni, *Microbiome Engineering: Synthetic Biology of Plant-Associated Microbiomes in Sustainable Agriculture.* Trends Biotechnol, 2021. **39**(3): p. 244-261.
11. Omer, R., et al., *Engineered Bacteria-Based Living Materials for Biotherapeutic Applications.* Front Bioeng Biotechnol, 2022. **10**: p. 870675.
12. Ceroni, F., et al., *Quantifying cellular capacity identifies gene expression designs with reduced burden.* Nat Methods, 2015. **12**(5): p. 415-8.
13. Ceroni, F., et al., *Burden-driven feedback control of gene expression.* Nat Methods, 2018. **15**(5): p. 387-393.
14. Wu, G., et al., *Metabolic Burden: Cornerstones in Synthetic Biology and Metabolic Engineering Applications.* Trends Biotechnol, 2016. **34**(8): p. 652-664.
15. Buddingh, B.C. and J.C.M. van Hest, *Artificial Cells: Synthetic Compartments with Life-like Functionality and Adaptivity.* Acc Chem Res, 2017. **50**(4): p. 769-777.
16. Jiang, W., et al., *Artificial Cells: Past, Present and Future.* ACS Nano, 2022. **16**(10): p. 15705-15733.
17. Salehi-Reyhani, A., O. Ces, and Y. Elani, *Artificial cell mimics as simplified models for the study of cell biology.* Exp Biol Med (Maywood), 2017. **242**(13): p. 1309-1317.
18. Stano, P. and F. Mavelli, *Protocells Models in Origin of Life and Synthetic Biology.* Life, 2015. **5**: p. 1700-1702.
19. Stano, P., *Is Research on " ynthetic Cells" Moving to the ext Level?* Life, 2018. **9**: p. 3.
20. Xu, C., S. Hu, and X. Chen, *Artificial cells: from basic science to applications.* Mater Today (Kidlington), 2016. **19**(9): p. 516-532.
21. Kraft, M.L., *Plasma membrane organization and function: moving past lipid rafts.* Mol Biol Cell, 2013. **24**(18): p. 2765-8.

22. Shaw, T.R., S. Ghosh, and S.L. Veatch, *Critical Phenomena in Plasma Membrane Organization and Function.* Annu Rev Phys Chem, 2021. **72**: p. 51-72.
23. Brown, D.A. and E. London, *Structure and origin of ordered lipid domains in biological membranes.* J Membr Biol, 1998. **164**(2): p. 103-14.
24. Harayama, T. and H. Riezman, *Understanding the diversity of membrane lipid composition.* Nat Rev Mol Cell Biol, 2018. **19**(5): p. 281-296.
25. Chiu, M.L., *Introduction to membrane proteins.* Curr Protoc Protein Sci, 2012. **Chapter 29**: p. 29 1 1-29 1 8.
26. Lombard, J., *Once upon a time the cell membranes: 175 years of cell boundary research.* Biol Direct, 2014. **9**: p. 32.
27. Singer, S.J. and G.L. Nicolson, *The fluid mosaic model of the structure of cell membranes.* Science, 1972. **175**(4023): p. 720-31.
28. Israelachvili, J.N., *Refinement of the fluid-mosaic model of membrane structure.* Biochim Biophys Acta, 1977. **469**(2): p. 221-5.
29. Wisniewska, A., J. Draus, and W.K. Subczynski, *Is a fluid-mosaic model of biological membranes fully relevant? Studies on lipid organization in model and biological membranes.* Cell Mol Biol Lett, 2003. **8**(1): p. 147-59.
30. Simons, K. and R. Ehehalt, *Cholesterol, lipid rafts, and disease.* J Clin Invest, 2002. **110**(5): p. 597-603.
31. Nicolson, G.L., *Update of the 1972 Singer-Nicolson Fluid-Mosaic Model of Membrane Structure.* Discoveries (Craiova), 2013. **1**(1): p. e3.
32. Ikeda, M., A. Kihara, and Y. Igarashi, *Lipid asymmetry of the eukaryotic plasma membrane: functions and related enzymes.* Biol Pharm Bull, 2006. **29**(8): p. 1542-6.
33. Bevers, E.M. and P.L. Williamson, *Getting to the Outer Leaflet: Physiology of Phosphatidylserine Exposure at the Plasma Membrane.* Physiol Rev, 2016. **96**(2): p. 605-45.
34. Fadeel, B. and D. Xue, *The ins and outs of phospholipid asymmetry in the plasma membrane: roles in health and disease.* Crit Rev Biochem Mol Biol, 2009. **44**(5): p. 264-77.
35. Dai, Y., H. Tang, and S. Pang, *The Crucial Roles of Phospholipids in Aging and Lifespan Regulation.* Front Physiol, 2021. **12**: p. 775648.
36. Tolomeu, H.V. and C.A.M. Fraga, *Imidazole: Synthesis, Functionalization and Physicochemical Properties of a Privileged Structure in Medicinal Chemistry.* Molecules, 2023. **28**(2).
37. Manikandan, A., D. Divakar, and N. Poonam Singh, *Phospholipid—the dynamic structure between living and non-living world; a much obligatory supramolecule for present and future.* AIMS Molecular Science 2019. **6**: p. 1-19.
38. Dufourc, E.J., *Sterols and membrane dynamics.* J Chem Biol, 2008. **1**(1-4): p. 63-77.
39. Blanco, A. and G. Blanco, *Chapter 5 - Lipids*, in *Medical Biochemistry*. 2017: Academic Press. p. 99-119.
40. Levental, I. and E. Lyman, *Regulation of membrane protein structure and function by their lipid nano-environment.* Nat Rev Mol Cell Biol, 2023. **24**(2): p. 107-122.
41. Rousseau, D., R.R. Rafanan, and R. Yada, *Microemulsions as Nanoscale Delivery Systems.* Comprehensive Biotechnology, 2011. **4**: p. 675-682.
42. Luzzati, V., et al., *Structure and polymorphism in lipid-water systems, and their possible biological implications.* Ann N Y Acad Sci, 1966. **137**(2): p. 409-13.

43. Simons, K. and J.L. Sampaio, *Membrane organization and lipid rafts.* Cold Spring Harb Perspect Biol, 2011. **3**(10): p. a004697.
44. Jouhet, J., *Importance of the hexagonal lipid phase in biological membrane organization.* Front Plant Sci, 2013. **4**: p. 494.
45. Ramezanpour, M., et al., *Structural Properties of Inverted Hexagonal Phase: A Hybrid Computational and Experimental Approach.* Langmuir, 2020. **36**(24): p. 6668-6680.
46. Leekumjorn, S. and A.K. Sum, *Molecular studies of the gel to liquid-crystalline phase transition for fully hydrated DPPC and DPPE bilayers.* Biochim Biophys Acta, 2007. **1768**(2): p. 354-65.
47. Schonfeldova, T., et al., *Lipid Melting Transitions Involve Structural Redistribution of Interfacial Water.* J Phys Chem B, 2021. **125**(45): p. 12457-12465.
48. Brkljača, Z., et al., *Monitoring lipid phase transition temperatures using fluorescent probes and temperature-dependent fluorescence spectroscopy.* Dyes and Pigments, 2022. **206**.
49. Llado, V., et al., *Regulation of the cancer cell membrane lipid composition by NaCHOleate: effects on cell signaling and therapeutical relevance in glioma.* Biochim Biophys Acta, 2014. **1838**(6): p. 1619-27.
50. Zhang, G. and J. Sun, *Lipid in Chips: A Brief Review of Liposomes Formation by Microfluidics.* Int J Nanomedicine, 2021. **16**: p. 7391-7416.
51. Fanalista, F., et al., *Shape and Size Control of Artificial Cells for Bottom-Up Biology.* ACS Nano, 2019. **13**(5): p. 5439-5450.
52. Weinberger, A., et al., *Gel-assisted formation of giant unilamellar vesicles.* Biophys J, 2013. **105**(1): p. 154-64.
53. Carugo, D., et al., *Liposome production by microfluidics: potential and limiting factors.* Sci Rep, 2016. **6**: p. 25876.
54. Akbarzadeh, A., et al., *Liposome: classification, preparation, and applications.* Nanoscale Res Lett, 2013. **8**(1): p. 102.
55. Hindley, J.W., R.V. Law, and O. Ces, *Membrane functionalization in artificial cell engineering.* Discover Applied Sciences, 2020. **2**.
56. Armstrong, J.P. and A.W. Perriman, *Strategies for cell membrane functionalization.* Exp Biol Med (Maywood), 2016. **241**(10): p. 1098-106.
57. Zhao, J., et al., *Mimicking Cellular Metabolism in Artificial Cells: Universal Molecule Transport across the Membrane through Vesicle Fusion.* Anal Chem, 2022. **94**(9): p. 3811-3818.
58. Sharma, B., et al., *Synthetic Cell as a Platform for Understanding Membrane-Membrane Interactions.* Membranes (Basel), 2021. **11**(12).
59. Mondal Roy, S. and M. Sarkar, *Membrane fusion induced by small molecules and ions.* J Lipids, 2011. **2011**: p. 528784.
60. Vlieghe, A., et al., *Role of Lipids and Divalent Cations in Membrane Fusion Mediated by the Heptad Repeat Domain 1 of Mitofusin.* Biomolecules, 2023. **13**(9).
61. Joardar, A., G.P. Pattnaik, and H. Chakraborty, *Mechanism of Membrane Fusion: Interplay of Lipid and Peptide.* J Membr Biol, 2022. **255**(2-3): p. 211-224.
62. Aronson, J.F., *Nuclear membrane fusion in fertilized Lytechinus variegatus eggs.* J Cell Biol, 1973. **58**(1): p. 126-34.
63. van Hoogevest, P. and A. Wendel, *The use of natural and synthetic phospholipids as pharmaceutical excipients.* Eur J Lipid Sci Technol, 2014. **116**(9): p. 1088-1107.

64. Baer, E., A.J. Duke, and D. Buchnea, *Synthesis of propylene glycol phospholipids: analogues of alpha-lecithins and alpha-cephalins.* Can J Biochem, 1968. **46**(1): p. 69-74.
65. Baer, E. and H.O. Fischer, *L(+)propylene glycol.* J Am Chem Soc, 1948. **70**(2): p. 609.
66. Guo, Z., A.F. Vikbjerg, and X. Xu, *Enzymatic modification of phospholipids for functional applications and human nutrition.* Biotechnol Adv, 2005. **23**(3): p. 203-59.
67. Schaub, T., *Efficient Industrial Organic Synthesis and the Principles of Green Chemistry.* Chemistry, 2021. **27**(6): p. 1865-1869.
68. Dadkhah, M. and J.M. Tulliani, *Green Synthesis of Metal Oxides Semiconductors for Gas Sensing Applications.* Sensors (Basel), 2022. **22**(13).
69. Anastas, P. and N. Eghbali, *Green chemistry: principles and practice.* Chem Soc Rev, 2010. **39**(1): p. 301-12.
70. Hamid, B., et al., *Cold-Active Enzymes and Their Potential Industrial Applications-A Review.* Molecules, 2022. **27**(18).
71. Cerminati, S., et al., *Industrial uses of phospholipases: current state and future applications.* Appl Microbiol Biotechnol, 2019. **103**(6): p. 2571-2582.
72. Saichana, N., et al., *Acetic acid bacteria: A group of bacteria with versatile biotechnological applications.* Biotechnol Adv, 2015. **33**(6 Pt 2): p. 1260-71.
73. Bennett, J.W., *Mycotechnology: the role of fungi in biotechnology.* J Biotechnol, 1998. **66**(2-3): p. 101-7.
74. Alvarez, B. and L.A. Fernandez, *Sustainable therapies by engineered bacteria.* Microb Biotechnol, 2017. **10**(5): p. 1057-1061.
75. De Maria, L., et al., *Phospholipases and their industrial applications.* Appl Microbiol Biotechnol, 2007. **74**(2): p. 290-300.
76. Martin, S.F., R.L. DeBlanc, and P.J. Hergenrother, *Determination of the substrate specificity of the phospholipase D from Streptomyces chromofuscus via an inorganic phosphate quantitation assay.* Anal Biochem, 2000. **278**(2): p. 106-10.
77. Richmond, G.S. and T.K. Smith, *Phospholipases A(1).* Int J Mol Sci, 2011. **12**(1): p. 588-612.
78. Selvy, P.E., et al., *Phospholipase D: enzymology, functionality, and chemical modulation.* Chem Rev, 2011. **111**(10): p. 6064-119.
79. Liscovitch, M., et al., *Phospholipase D: molecular and cell biology of a novel gene family.* Biochem J, 2000. **345 Pt 3**(Pt 3): p. 401-15.
80. Yang, H. and M.F. Roberts, *Phosphohydrolase and transphosphatidylation reactions of two Streptomyces phospholipase D enzymes: covalent versus noncovalent catalysis.* Protein Sci, 2003. **12**(9): p. 2087-98.
81. Lindberg, J., J. Ekeroth, and P. Konradsson, *Efficient synthesis of phospholipids from glycidyl phosphates.* J Org Chem, 2002. **67**(1): p. 194-9.
82. Juneja, L.R., et al., *Conversion of phosphatidylcholine to phosphatidylserine by various phospholipases D in the presence of l- or d-serine.* Biochim. Biophys. Acta Lipids Lipid Metab., 1989. **1003**: p. 277-283.
83. Juneja, L.R., et al., *Kinetic evaluation of conversion of phosphatidylcholine to phosphatidylethanolamine by phospholipase D from different sources.* Biochim Biophys Acta, 1988. **960**(3): p. 334-41.
84. Allegretti, C., et al., *Polar Head Modified Phospholipids by Phospholipase D-Catalyzed Transformations of Natural Phosphatidylcholine for Targeted Applications: An Overview.* Catalysts, 2020. **10**(9).

85. Patel, D. and S.N. Witt, *Ethanolamine and Phosphatidylethanolamine: Partners in Health and Disease.* Oxid Med Cell Longev, 2017. **2017**: p. 4829180.
86. Ponting, C.P. and I.D. Kerr, *A novel family of phospholipase D homologues that includes phospholipid synthases and putative endonucleases: identification of duplicated repeats and potential active site residues.* Protein Sci., 1996. **5**(5): p. 914-922.
87. Damnjanovic, J. and Y. Iwasaki, *Phospholipase D as a catalyst: application in phospholipid synthesis, molecular structure and protein engineering.* J Biosci Bioeng, 2013. **116**(3): p. 271-80.
88. Ulbrich-Hofmann, R., et al., *Phospholipase D and its application in biocatalysis.* Biotechnol Lett, 2005. **27**(8): p. 535-44.
89. Brasili, D., et al., *The unusual metal ion binding ability of histidyl tags and their mutated derivatives.* Dalton Trans, 2016. **45**(13): p. 5629-39.
90. Ruszkowski, M. and Z. Dauter, *Structures of Medicago truncatula L-Histidinol Dehydrogenase Show Rearrangements Required for NAD(+) Binding and the Cofactor Positioned to Accept a Hydride.* Sci Rep, 2017. **7**(1): p. 10476.
91. Bruice, T.C. and G.L. Schmir, *The catalysis of the hydrolysis of p-nitrophenyl acetate by imidazole and its derivatives.* Arch Biochem Biophys, 1956. **63**(2): p. 484-6.
92. Farr, G.W. and J.R. Heitz, *Imidazole catalysis of sucrose hydrolysis.* J Dent Res, 1974. **53**(3): p. 516-9.
93. Fubin, J., et al., *Metallomicellar catalysis: accelerated hydrolysis of BNPP by copper(II), zinc(II), and nickel(II) complexes of long alkanol-imidazole in CTAB micellar solution.* J Colloid Interface Sci, 2004. **273**(2): p. 497-504.
94. Phukan, M., H.J. Borah, and R. Borah, *Henry reaction in environmentally benign methods using imidazole as catalyst.* Green Chemistry Letters and Reviews, 2009. **2**(4): p. 249-253.
95. Jencks, W.P. and J. Carriuolo, *Imidazole catalysis. II. Acyl transfer and the reactions of acetyl imidazole with water and oxygen anions.* J Biol Chem, 1959. **234**(5): p. 1272-9.
96. Morrow, J.R., *Artificial ribonucleases.* Adv Inorg Biochem, 1994. **9**: p. 41-74.
97. Palermo, G., et al., *Catalytic metal ions and enzymatic processing of DNA and RNA.* Acc Chem Res, 2015. **48**(2): p. 220-8.
98. Ishihara, K., Y. Kosugi, and M. Akakura, *Rational design of an L-histidine-derived minimal artificial acylase for the kinetic resolution of racemic alcohols.* J Am Chem Soc, 2004. **126**(39): p. 12212-3.
99. Nieri, P., et al., *Cholinesterase-like organocatalysis by imidazole and imidazole-bearing molecules.* Sci Rep, 2017. **8**: p. 45760.
100. Singh, N., et al., *Insight into the esterase like activity demonstrated by an imidazole appended self-assembling hydrogelator.* Chem. Commun, 2015. **51**: p. 13213-13216.
101. Yuan, L., B.A. Nelson, and G. Caryl, *The catalytic cysteine and histidine in the plant acyl-acyl carrier protein thioesterases.* J Biol Chem, 1996. **271**(7): p. 3417-9.
102. Huo, L., et al., *Evidence for a dual role of an active site histidine in alpha-amino-beta-carboxymuconate-epsilon-semialdehyde decarboxylase.* Biochemistry, 2012. **51**(29): p. 5811-21.
103. Li, Z., et al., *Accurate Metal-Imidazole Interactions.* J Chem Theory Comput, 2022.
104. Brosnan, M.E. and J.T. Brosnan, *Histidine Metabolism and Function.* J Nutr, 2020. **150**(Suppl 1): p. 2570S-2575S.
105. Pfeiffer, M., et al., *Essential Functional Interplay of the Catalytic Groups in Acid Phosphatase.* ACS Catal, 2022. **12**(6): p. 3357-3370.

106. Barwinska-Sendra, A., et al., *An evolutionary path to altered cofactor specificity in a metalloenzyme.* Nat Commun, 2020. **11**(1): p. 2738.
107. Huang, R., et al., *Imidazole-Based pH-Sensitive Convertible Liposomes for Anticancer Drug Delivery.* Pharmaceuticals (Basel), 2022. **15**(3).
108. Ju, L., et al., *Preparation and properties evaluation of a novel pH-sensitive liposomes based on imidazole-modified cholesterol derivatives.* Int J Pharm, 2017. **518**(1-2): p. 213-219.
109. Mendes, B.B., et al., *Nanodelivery of nucleic acids.* Nat Rev Methods Primers, 2022. **2**.
110. Moorthy, B.S., Y. Gao, and G.S. Anand, *Phosphodiesterases catalyze hydrolysis of cAMP-bound to regulatory subunit of protein kinase A and mediate signal termination.* Mol Cell Proteomics, 2011. **10**(2): p. M110 002295.
111. Belluati, A., et al., *Artificial cell synthesis using biocatalytic polymerization-induced self-assembly.* Nat Chem, 2024. **16**(4): p. 564-574.
112. Yang, H. and R. Woscholski, *A Novel High-Throughput Assay Reveals That the Temperature Induced Increases in Transphosphatidylation of Phospholipase D Are Dependent on the Alcohol Acceptor Concentration.* Biomolecules, 2022. **12**(5).
113. Udenfriend, S., et al., *Fluorescamine: a reagent for assay of amino acids, peptides, proteins, and primary amines in the picomole range.* Science, 1972. **178**(4063): p. 871-2.
114. Guo, Z. and X. Xu, *Biosynthesis of Phosphatidyl Vitamin B6 by Phospholipase D Catalyzed Transphosphatidylation.* Austin Food Sci. , 2016.
115. Nakazawa, Y., et al., *Large-scale production of phospholipase D from Streptomyces racemochromogenes and its application to soybean lecithin modification.* Appl Biochem Biotechnol, 2011. **165**(7-8): p. 1494-506.
116. Kumar, R.N., et al., *Development of a thin layer chromatography-based method to detect sorbitol presence in milk and its applicability in formalin preserved milk samples.* J Food Sci Technol, 2024. **61**(5): p. 870-878.
117. Chen, S., et al., *Bioconversion of phosphatidylserine by phospholipase D from Streptomyces racemochromogenes in a microaqueous water-immiscible organic solvent.* Biosci Biotechnol Biochem, 2013. **77**(9): p. 1939-41.
118. Touchstone, J.C., *Thin-layer chromatographic procedures for lipid separation.* J Chromatogr B Biomed Appl, 1995. **671**(1-2): p. 169-95.
119. Dittmer, J.C. and R.L. Lester, *A Simple, Specific Spray for the Detection of Phospholipids on Thin-Layer Chromatograms.* J Lipid Res, 1964. **5**: p. 126-7.
120. Sinhababu, A., H. Dey, and S. Basu, *A Novel Spray Reagent for the Detection of Amino Acids on Thin Layer Chromatography Plates.* TACL, 2013. **3**: p. 330 - 334.
121. Sherma, J. and J.C. Touchstone, *Quantitative Thin Layer Chromatography of Amino Acids Using Fluorescamine Reagent.* Analytical Letters, 1973. **7**.
122. Lu, Z., et al., *A small-scale silica gel column chromatography method for separating carbazole compounds from highly mature crude oil.* J Chromatogr A, 2024. **1713**: p. 464536.
123. Alviz-Gazitua, P., et al., *The Response of Cupriavidus metallidurans CH34 to Cadmium Involves Inhibition of the Initiation of Biofilm Formation, Decrease in Intracellular c-di-GMP Levels, and a Novel Metal Regulated Phosphodiesterase.* Front Microbiol, 2019. **10**: p. 1499.
124. Salar, U., W. Atia Tul, and M. Iqbal Choudhary, *Biochemical evaluation and ligand binding studies on glycerophosphodiester phosphodiesterase from Staphylococcus*

aureus using STD-NMR spectroscopy and molecular docking analysis. Bioorg Chem, 2024. **144**: p. 107153.
125. Pinna, L.A. and A. Donella-Deana, *Phosphorylated synthetic peptides as tools for studying protein phosphatases.* Biochimica et Biophysica Acta (BBA) - Molecular Cell Research 1993. **1222**(3): p. 415-431.
126. Zhang, Z.Y., et al., *Expression, purification, and physicochemical characterization of a recombinant Yersinia protein tyrosine phosphatase.* J Biol Chem, 1992. **267**(33): p. 23759-66.
127. Poznik, M. and B. Konig, *Cooperative hydrolysis of aryl esters on functionalized membrane surfaces and in micellar solutions.* Org Biomol Chem, 2014. **12**(20): p. 3175-80.
128. Berger, N., et al., *Filter extrusion of liposomes using different devices: comparison of liposome size, encapsulation efficiency, and process characteristics.* Int J Pharm, 2001. **223**(1-2): p. 55-68.
129. Gispert, I., et al., *Stimuli-responsive vesicles as distributed artificial organelles for bacterial activation.* Proc Natl Acad Sci U S A, 2022. **119**(42): p. e2206563119.
130. Moga, A., et al., *Optimization of the Inverted Emulsion Method for High-Yield Production of Biomimetic Giant Unilamellar Vesicles.* Chembiochem, 2019. **20**(20): p. 2674-2682.
131. Hindley, J.W., et al., *Light-triggered enzymatic reactions in nested vesicle reactors.* Nat Commun, 2018. **9**(1): p. 1093.
132. Pencer, J., G.F. White, and F.R. Hallett, *Osmotically induced shape changes of large unilamellar vesicles measured by dynamic light scattering.* Biophys J, 2001. **81**(5): p. 2716-28.
133. Jin, A.J., et al., *Light scattering characterization of extruded lipid vesicles.* Eur Biophys J, 1999. **28**(3): p. 187-99.
134. Elliott, A.D., *Confocal Microscopy: Principles and Modern Practices.* Curr Protoc Cytom, 2020. **92**(1): p. e68.
135. Pedelacq, J.D., et al., *Engineering and characterization of a superfolder green fluorescent protein.* Nat Biotechnol, 2006. **24**(1): p. 79-88.
136. Bradford, M.M., *A rapid and sensitive method for the quantitation of microgram quantities of protein utilizing the principle of protein-dye binding.* Anal Biochem, 1976. **72**: p. 248-54.
137. Chapman, J., A.E. Ismail, and C.Z. Dinu, *Industrial Applications of Enzymes: Recent Advances, Techniques, and Outlooks.* Catalysts, 2018. **8**(6): p. 238.
138. Bravo-Alfaro, D.A., et al., *The enzymatic modification of phospholipids improves their surface-active properties and the formation of nanoemulsions.* Biocatalysis and Agricultural Biotechnology, 2023. **48**.
139. Hama, S., C. Ogino, and A. Kondo, *Enzymatic synthesis and modification of structured phospholipids: recent advances in enzyme preparation and biocatalytic processes.* Appl Microbiol Biotechnol, 2015. **99**(19): p. 7879-91.
140. Rich, J.O. and Y.L. Khmelnitsky, *Phospholipase D-catalyzed transphosphatidylation in anhydrous organic solvents.* Biotechnol Bioeng, 2001. **72**(3): p. 374-7.
141. Uesugi, Y. and T. Hatanaka, *Phospholipase D mechanism using Streptomyces PLD.* Biochim Biophys Acta, 2009. **1791**(9): p. 962-9.
142. Xiao, H., et al., *Damage of proteins at the air/water interface: Surface tension characterizes globulin interface stability.* Int J Pharm, 2020. **584**: p. 119445.

143. Noskov, B.A., et al., *Bovine serum albumin unfolding at the air/water interface as studied by dilational surface rheology.* Langmuir, 2010. **26**(22): p. 17225-31.
144. Carrea, G., et al., *Purification and properties of two phospholipases D from Streptomyces sp.* Biochim Biophys Acta, 1995. **1255**(3): p. 273-9.
145. Dippe, M., et al., *Phospholipase D-catalyzed synthesis of new phospholipids with polar head groups.* Chem Phys Lipids, 2008. **152**(2): p. 71-7.
146. Zhou, W.B., et al., *Mining of a phospholipase D and its application in enzymatic preparation of phosphatidylserine.* Bioengineered, 2018. **9**(1): p. 80-89.
147. Sato, R., et al., *Effect of temperature on the stereoselectivity of phospholipase D toward glycerol in the transphosphatidylation of phosphatidylcholine to phosphatidylglycerol.* Lipids, 2004. **39**(10): p. 1019-23.
148. Juneja, L.R., et al., *Increasing productivity by removing choline in conversion of phosphatidylcholine to phosphatidylserine by phospholipase D.* Journal of Fermentation and Bioengineering, 1992. **73**(5): p. 357-361.
149. Pisch, S., et al., *Properties of unusual phospholipids IV: Chemoenzymatic synthesis of phospholipids bearing acetylenic fatty acids.* Tetrahedron, 1997. **53**(43): p. 14627-14634.
150. Doig, S.D. and R.M.M. Diks, *Toolbox for modification of the lecithin headgroup.* European Journal of Lipid Science and Technology, 2003. **105**(7): p. 368-376.
151. Xu, G., et al., *Thin-Layer Chromatography of Phospholipids and Their Lyso Forms: Application to Determination of Extracts from Rat Hippocampal CA1 Region.* Microchemical Journal, 1996. **53**: p. 29-33.
152. Cid-Hernandez, M., et al., *Two-Dimensional Thin Layer Chromatography-Bioautography Designed to Separate and Locate Metabolites with Antioxidant Activity Contained on Spirulina platensis.* Int J Anal Chem, 2018. **2018**: p. 4605373.
153. Cole, S.R. and J.G. Dorsey, *Cyclohexylamine Additives for Enhanced Peptide Separations in Reversed Phase Liquid Chromatography.* Biomedical Chromatography, 1997. **11**(3): p. 167-171.
154. Sigel, A. and H. Sigel, *Metal ions in biological systems*, ed. T.L.a.T.I.w. Biosystems. Vol. 40. 2003.
155. Greiner, B.A., et al., *Imidazole-based nickel(II) and cobalt(II) coordination complexes for potential use as models for histidine containing metalloproteins.* Inorganica Chimica Acta, 2007. **360**(10): p. 3132-3140.
156. Bauman, J.E. and J.C. Wang, *Imidazole Complexes of Nickel(II), Copper(II), Zinc(II), and Silver(I).* Inorganic Chemistry, 1963. **3**(3): p. 368–373.
157. Mahdy, A.R.E., et al., *Synthesis, characterization, and biological activity of Co(II) and Zn(II) complexes of imidazoles-based azo-functionalized Schiff bases.* Journal of Molecular Structure, 2022. **1259**.
158. Bete, S.C., C. Wurtele, and M. Otte, *A bio-inspired imidazole-functionalised copper cage complex.* Chem Commun (Camb), 2019. **55**(30): p. 4427-4430.
159. Rannulu, N.S. and M.T. Rodgers, *Solvation of copper ions by imidazole: structures and sequential binding energies of Cu+(imidazole)x, x = 1-4. Competition between ion solvation and hydrogen bonding.* Phys Chem Chem Phys, 2005. **7**(5): p. 1014-25.
160. Solomon, E.I., et al., *Geometric and electronic structure/function correlations in non-heme iron enzymes.* Chem Rev, 2000. **100**(1): p. 235-350.
161. Kim, J.K., et al., *Elucidating the role of metal ions in carbonic anhydrase catalysis.* Nat Commun, 2020. **11**(1): p. 4557.

162. Tirel, E.Y., et al., *Catalytic zinc complexes for phosphate diester hydrolysis.* Angew Chem Int Ed Engl, 2014. **53**(31): p. 8246-50.
163. Lippard, S.J. and J.M. Berg, *Principles of Bioinorganic Chemistry*. University Science Books, ed. Medical. 1994.
164. Qiu, S.R., et al., *Origins of optical absorption characteristics of Cu(2+) complexes in aqueous solutions.* Phys Chem Chem Phys, 2015. **17**(29): p. 18913-23.
165. Kocyla, A., A. Pomorski, and A. Krezel, *Molar absorption coefficients and stability constants of Zincon metal complexes for determination of metal ions and bioinorganic applications.* J Inorg Biochem, 2017. **176**: p. 53-65.
166. Rossi, A.V. and M. Tubino, *The kinetics and mechanism of the reaction of ZINCON, o-[1-(2-hydroxy-5-sulfophenyl)-3-phenyl-5-formazane] benzoic acid, with Zn2+, Cu2+ and [Zn2+ + Cu2+] equimolar mixtures.* Journal of the Brazilian Chemical Society, 1996. **7**(3): p. 161-168.
167. Rush, R.M. and J.H. Yoe, *Colorimetric Determination of Zinc and Copper with 2-Carboxy-2´-hydroxy-5´-sulfoformazylbenzene.* American Chemical Society, 1954. **26**(8): p. 1345-1347.
168. Breuer, W., et al., *Transport of iron and other transition metals into cells as revealed by a fluorescent probe.* Am J Physiol, 1995. **268**(6 Pt 1): p. C1354-61.
169. Konijn, A.M., et al., *The cellular labile iron pool and intracellular ferritin in K562 cells.* Blood, 1999. **94**(6): p. 2128-34.
170. Petronilli, V., et al., *Transient and long-lasting openings of the mitochondrial permeability transition pore can be monitored directly in intact cells by changes in mitochondrial calcein fluorescence.* Biophys J, 1999. **76**(2): p. 725-34.
171. Hindley, J.W., et al., *Building a synthetic mechanosensitive signaling pathway in compartmentalized artificial cells.* Proc Natl Acad Sci U S A, 2019. **116**(34): p. 16711-16716.
172. Cormack, B.P., R.H. Valdivia, and S. Falkow, *FACS-optimized mutants of the green fluorescent protein (GFP).* Gene, 1996. **173**(1 Spec No): p. 33-8.
173. Liu, H.L., Y. Ho, and C.M. Hsu, *Molecular simulations to determine the chelating mechanisms of various metal ions to the His-tag motif: a preliminary study.* J Biomol Struct Dyn, 2003. **21**(1): p. 31-41.
174. Watly, J., et al., *African Viper Poly-His Tag Peptide Fragment Efficiently Binds Metal Ions and Is Folded into an alpha-Helical Structure.* Inorg Chem, 2015. **54**(16): p. 7692-702.
175. Cantarero, L.A., J.E. Butler, and J.W. Osborne, *The adsorptive characteristics of proteins for polystyrene and their significance in solid-phase imunoassays.* Anal Biochem, 1980. **105**(2): p. 375-82.
176. Moringo, N.A., et al., *Polymer Free Volume Effects on Protein Dynamics in Polystyrene Revealed by Single-Molecule Spectroscopy.* Langmuir, 2020. **36**(9): p. 2330-2338.
177. Block, H., et al., *Immobilized-metal affinity chromatography (IMAC): a review.* Methods Enzymol, 2009. **463**: p. 439-73.
178. Porath, J., et al., *Metal chelate affinity chromatography, a new approach to protein fractionation.* Nature, 1975. **258**(5536): p. 598-9.
179. Lee, H.K., et al., *Interactions between a receptor tyrosine phosphatase and a cell surface ligand regulate axon guidance and glial-neuronal communication.* Neuron, 2013. **78**(5): p. 813-26.
180. Lentini, R., et al., *Two-Way Chemical Communication between Artificial and Natural Cells.* ACS Central Science, 2017. **3**(2): p. 117-123.

181. Ugi, S., et al., *Protein phosphatase 2A negatively regulates insulin's metabolic signaling pathway by inhibiting Akt (protein kinase B) activity in 3T3-L1 adipocytes.* Mol Cell Biol, 2004. **24**(19): p. 8778-89.
182. Elani, Y., *Construction of membrane-bound artificial cells using microfluidics: a new frontier in bottom-up synthetic biology.* Biochem Soc Trans, 2016. **44**(3): p. 723-30.
183. Elani, Y., R.V. Law, and O. Ces, *Vesicle-based artificial cells as chemical microreactors with spatially segregated reaction pathways.* Nat Commun, 2014. **5**: p. 5305.
184. Fuller, N. and R.P. Rand, *The influence of lysolipids on the spontaneous curvature and bending elasticity of phospholipid membranes.* Biophys J, 2001. **81**(1): p. 243-54.
185. Pengo, P., et al., *Carboxylate-imidazole cooperativity in dipeptide-functionalized gold nanoparticles with esterase-like activity.* J Am Chem Soc, 2005. **127**(6): p. 1616-7.
186. Gayen, K., et al., *Amino-Acid-Based Metallo-Hydrogel That Acts Like an Esterase.* ACS Appl Bio Mater, 2018. **1**(5): p. 1717-1724.
187. Arifuzzaman, M.D., et al., *Imprinted polymeric nanoparticles as artificial enzymes for ester hydrolysis at room temperature and pH 7.* Chem Catalysis, 2022. **2**: p. 2049-2065.
188. Wang, D., et al., *Imidazolium-Based Lipid Analogues and Their Interaction with Phosphatidylcholine Membranes.* Langmuir, 2016. **32**(48): p. 12579-12592.
189. Kriegler, S., et al., *Bipolar Imidazolium-Based Lipid Analogues for Artificial Archaeosomes.* Langmuir, 2021. **37**(41): p. 11996-12006.
190. Beavo, J.A., *Cyclic nucleotide phosphodiesterases: functional implications of multiple isoforms.* Physiol Rev, 1995. **75**(4): p. 725-48.
191. Maurice, D.H., et al., *Advances in targeting cyclic nucleotide phosphodiesterases.* Nat Rev Drug Discov, 2014. **13**(4): p. 290-314.
192. Liu, Y., et al., *Hydrolysis of phosphodiester catalyzed by metallomicelles with histidine residue: Kinetics and mechanism.* Colloids and Surfaces A: Physicochemical and Engineering Aspects, 2013. **436**: p. 839-845.
193. Orth, E.S., et al., *Intramolecular catalysis of phosphodiester hydrolysis by two imidazoles.* J Am Chem Soc, 2010. **132**(24): p. 8513-23.
194. Soper, A.S. and S.D. Aird, *Elution of tightly bound solutes from concanavalin A Sepharose. Factors affecting the desorption of cottonmouth venom glycoproteins.* J Chromatogr A, 2007. **1154**(1-2): p. 308-18.
195. Chen, J., et al., *An Asymmetric Dizinc Phosphodiesterase Model with Phenolate and Carboxylate Bridges.* Inorganic Chemistry, 2005. **44**(10): p. 3422-3430.
196. Conti, M. and J. Beavo, *Biochemistry and physiology of cyclic nucleotide phosphodiesterases: essential components in cyclic nucleotide signaling.* Annu Rev Biochem, 2007. **76**: p. 481-511.
197. Wu, Y., et al., *Overview of nanozymes with phosphatase-like activity.* Biosens Bioelectron, 2023. **237**: p. 115470.
198. Liu, H. and J. Liu, *Self-limited Phosphatase-mimicking CeO2 Nanozymes.* ChemNanoMat, 2020. **6**(6): p. 947-952.
199. Bowers, G.N., et al., *High-Purity 4-Nitrophenol: Purification, Characterization, and Specifications for Use as a Spectrophotometric Reference Material.* Clinical Chemistry, 1980. **26**(6): p. 724-729.
200. Larre, C., et al., *Assessment of allergenicity of diploid and hexaploid wheat genotypes: identification of allergens in the albumin/globulin fraction.* J Proteomics, 2011. **74**(8): p. 1279-89.

201. Darnay, B.G., et al., *Activation of NF-kappaB by RANK requires tumor necrosis factor receptor-associated factor (TRAF) 6 and NF-kappaB-inducing kinase. Identification of a novel TRAF6 interaction motif.* J Biol Chem, 1999. **274**(12): p. 7724-31.
202. Vinson, P.K., Y. Talmon, and A. Walter, *Vesicle-micelle transition of phosphatidylcholine and octyl glucoside elucidated by cryo-transmission electron microscopy.* Biophys J, 1989. **56**(4): p. 669-81.
203. Needham, D., et al., *Bottom up design of nanoparticles for anti-cancer diapeutics: "put the drug in the cancer's food".* J Drug Target, 2016. **24**(9): p. 836-856.
204. Appleton, D.W. and B. Sarkar, *Studies of Zn(II) and Co(II) complexes of imidazole and n-methylimidazole with regard to the activity related ionization in carbonic anhydrase.* Bioinorg Chem, 1977. **7**(3): p. 211-24.
205. Asayama, S., S. Nishinohara, and H. Kawakami, *Zinc-chelated imidazole groups for DNA polyion complex formation.* Metallomics, 2011. **3**(7): p. 680-2.
206. Mohapatra, S.K., K.S. Prakash, and U.L. Prasana, *Aquo-pentamine Co(III) complexes as models for carbonic anhydrase.* 1984. **21**: p. 287-294.
207. Weijnen, J.G.J., A. Koudijs, and J.F.J. Engbersen, *Carboxylic and phosphate ester hydrolysis catalysed by bivalent zinc and copper metallosurfactants.* Journal of the Chemical Society, Perkin Transactions 2, 1991: p. 1121-1126.
208. Pogostin, B.H., et al., *pKa Determination of a Histidine Residue in a Short Peptide Using Raman Spectroscopy.* Molecules, 2019. **24**(3).
209. Pace, H., et al., *Preserved transmembrane protein mobility in polymer-supported lipid bilayers derived from cell membranes.* Anal Chem, 2015. **87**(18): p. 9194-203.
210. Thorsteinsson, K., et al., *FRET-Based Assay for the Quantification of Extracellular Vesicles and Other Vesicles of Complex Composition.* Anal Chem, 2020. **92**(23): p. 15336-15343.
211. Uster, P.S., *In situ resonance energy transfer microscopy: monitoring membrane fusion in living cells.* Methods Enzymol, 1993. **221**: p. 239-46.
212. Struck, D.K., D. Hoekstra, and R.E. Pagano, *Use of resonance energy transfer to monitor membrane fusion.* Biochemistry, 1981. **20**(14): p. 4093-9.
213. Wang, T., C. Ingram, and J.C. Weisshaar, *Model lipid bilayer with facile diffusion of lipids and integral membrane proteins.* Langmuir, 2010. **26**(13): p. 11157-64.
214. Chernomordik, L.V. and M.M. Kozlov, *Mechanics of membrane fusion.* Nat Struct Mol Biol, 2008. **15**(7): p. 675-83.
215. Roe, M.W., J.J. Lemasters, and B. Herman, *Assessment of Fura-2 for measurements of cytosolic free calcium.* Cell Calcium, 1990. **11**(2-3): p. 63-73.
216. Atar, D., et al., *Excitation-transcription coupling mediated by zinc influx through voltage-dependent calcium channels.* J Biol Chem, 1995. **270**(6): p. 2473-7.
217. Chen, J., et al., *Application of large-scale transient transfection to cell-based functional assays for ion channels and GPCRs.* Methods Enzymol, 2010. **485**: p. 293-309.
218. Domaille, D.W., E.L. Que, and C.J. Chang, *Synthetic fluorescent sensors for studying the cell biology of metals.* Nat Chem Biol, 2008. **4**(3): p. 168-75.
219. D'Arrigo, P., et al., *Preparative transformation of natural phospholipids catalysed by phospholipase D from Streptomyces.* J. Chem. Soc., 1996(21): p. 2651-2656.
220. Birichevskaya, L.L., et al., *Substrate requirements of phospholipase D from Streptomyces netropsis in the transphosphatidylation synthesis of phospolipids.* Chemistry of Natural Compounds, 2006. **42**: p. 32-35.

221. Rosemeyer, H., *Nucleolipids: natural occurrence, synthesis, molecular recognition, and supramolecular assemblies as potential precursors of life and bioorganic materials.* Chem Biodivers, 2005. **2**(8): p. 977-1063.